

Dissertation

Current-based Simulation Models of Quantum Motion

Johannes Mesa Pascasio

TU Wien, Rigorosum am 26. April 2017

Supervisor

Prof. Manfred Faber

Referees

Prof. Maurice A. de Gosson

Prof. Basil Hiley

Kurzfassung

In den letzten Jahren wurden Teilchenbewegungen auf makroskopischer Ebene beobachtet, die bislang nur aus der Quantenmechanik bekannt waren. Obgleich es sich bei solchen Experimenten, wie sie von der Gruppe um Couder und Fort ausgeführt wurden, um rein klassische Physik handelt, gelingt in einer Analogiebetrachtung eine neuartige Beschreibung mikroskopischer Phänomene.

In dieser Arbeit wird mit Hilfe rein klassischer Mittel ein Modell des Bouncer–Walker Systems eines elementaren Teilchens konstruiert, das zugleich die alte Idee de Broglies, des Welle-Teilchen Dualismus, widerspiegelt. Dieses Modell beinhaltet einerseits eine mögliche Erklärung des Energieaustausches zwischen diesen separierten Bewegungen und somit eine Begründung für die Energiequantelung wie ursprünglich von Max Planck postuliert. Andererseits erlaubt das Modell die präzise Ausführung der bohmschen Bewegungen in perfekter Übereinstimmung mit der Quantenmechanik.

Zur Berechnung quantenmechanischer Teilchenbahnen im Ein- oder Mehrspaltsystem eignet sich die ballistische Diffusionsgleichung, eine spezielle Form der Diffusionsgleichung mit zeitabhängiger Diffusivität. Dies macht es möglich, wie hier gezeigt werden soll, den Zerfall eines gaußschen Wellenpakets auf elegante Weise zu simulieren.

Mit diesen Instrumenten wird in dieser Arbeit schließlich eine Rechenvorschrift zur Behandlung der auftretenden Ströme entwickelt, die äquivalent zur de Broglie–Bohm Theorie bleibt. Damit lassen sich Talbot-Muster und die Talbot-Distanz für beliebige Mehrspaltsysteme elegant reproduzieren.

Bei großen Unterschieden der Intensitäten in Doppelspaltexperimenten wird der Strahl geringer Intensität nach außen gedrückt und trotz anfänglich senkrechter Bewegung aus dem Spalt der Schirm seitlich von der Austrittsstelle getroffen. In dieser Arbeit wird die seitliche Anordnung des Schirms als mögliche alternative Messmethode untersucht.

Schließlich werden die mathematischen Simulationsverfahren, deren Limitierungen und mögliche Erweiterungen vorgestellt. Entkoppelt von der Diffusion lässt sich die Wirkung und somit die Phase als eine neue Quantität einer Gaußverteilung berechnen. Für ein Mehrspaltsystem genügt es in Folge, die Phasen zu kombinieren um die korrekte Intensitätsverteilung sowie die zugehörigen Wahrscheinlichkeitsströme zu erhalten. Die Entkopplung erlaubt überdies die Berechnung variabler Spaltbreiten sowie Phasenverschiebung auf einfache Weise.

Abstract

In recent years particles' trajectories have been observed at a macroscopic level which had been associated with nothing but quantum mechanical theory before, even though these experiments carried out by Couder and Fort's group are purely classical physics. By analogical considerations a new kind of description of microscopic phenomena is possible.

With purely classical tools a model for a bouncer-walker system of an elementary particle will be derived in this work which reflects the old idea of de Broglie's particle-wave duality. This model contains, on the one hand, a possible explanation of the work-energy exchange between the two separated motions, thereby providing an energy quantisation as originally postulated by Max Planck. On the other hand, the system perfectly obeys the Bohmian-type law of motion in full accordance with quantum mechanics.

For the calculation of elementary particles' trajectories a ballistic diffusion equation will be derived which is a special case of a diffusion equation with a time-dependent diffusivity. Therewith the simulation of spreading of an elementary Gaussian is made easy as will be shown herein.

With these tools one also accounts for Born's rule for multi-slit systems and develops a set of current rules that directly leads to a new formulation of the guiding equation equivalent to the original one of the de Broglie-Bohm theory. As will be shown in this thesis, this tool reproduces Talbot patterns and Talbot distance for an arbitrary multi-slit system.

Moreover, the sweeper effect is shown to arise when the intensity relation of two beams of a double-slit experiment exhibit a big difference. Then, the low-intensity beam is pushed aside in a sense that its initial propagation straight out of the slit is bent towards the side. A sideways screen as an alternative measurement method is proposed.

At last, mathematical simulation tools as well as their limitations and possible extensions are provided. Decoupled from the diffusion part the action and thus also the phase can be calculated as a new quantity of each single Gaussian. Then, for a multi-slit system a simple combination of these phases yields the correct intensity distributions including the complete interference patterns as well as the associated probability currents. The decoupling further allows for calculation of setups comprising variable slit widths as well as phase shifting.

Contents

Kurzfassung	ii
Abstract	iii
Introduction	1
1. The fluid droplet picture adapted to quantum mechanics	3
1.1. The macroscopic fluid droplet	3
1.2. A classical oscillator: The bouncer	5
1.3. Brownian motion of a particle: The walker	8
1.4. The walking bouncer	13
1.5. Conclusions and perspectives	16
2. Probability distributions and velocities	18
2.1. Outline	18
2.2. The constituting setup	19
2.3. Orthogonality relations and fluctuations	22
2.4. From classical phase-space distributions to quantum mechanical dispersion	26
2.5. Derivation of the time-dependent diffusion equation	28
2.6. Spreading of the wave packet	29
2.7. Conclusions and perspectives	32
3. Current-based theory on interference effects	35
3.1. Interference and emergence at a Gaussian double-slit	35
3.2. A set of current rules	38
3.3. Double-slit interference	42
3.4. Entangling currents in the double-slit experiment	47
3.5. Multi-slit interference and the quantum Talbot effect	56
3.6. Conclusions and outlook	62
4. Beam attenuation in double-slit experiments	64
4.1. Outline	64

4.2.	Deterministic and stochastic beam attenuation	65
4.2.1.	Beam attenuation in neutron interferometry	65
4.2.2.	Application to deterministic and stochastic beam attenuation experiments	66
4.3.	Phenomenology of the quantum sweeper for coherent and incoherent beams	69
4.4.	The quantum mechanical description of the sweeper effect	75
4.5.	Implications	78
4.6.	Conclusion and outlook	78
5.	Numerical methods	80
5.1.	Preliminaries	80
5.1.1.	The simulation setup	80
5.1.2.	Action and phase	81
5.1.3.	The diffusion coefficient in computations	83
5.2.	The finite difference method	86
5.2.1.	Coupled map lattices	86
5.2.2.	Crank–Nicolson’s method	90
5.2.3.	Comparison of the finite difference schemes	93
5.3.	The simulation procedure	94
5.4.	Trajectories	94
5.5.	Calibrating the simulation tools	96
5.6.	Conclusions and outlook	97
A.	Classical mechanics and Boltzmann’s relation	99
A.1.	The principle of least action	99
A.1.1.	The conservative case	102
A.1.2.	Reduced constraints	102
A.2.	A thermodynamical analogy	104
A.2.1.	Periodic motions	106
B.	Mathematical relations	109
B.1.	Random variables	109
B.2.	Vectors and fields	110
B.3.	Entropic functionals	110
	Bibliography	114
	Publication List	123

Introduction

Fundamental quantum phenomena are the basis of modern technologies like information theory or cryptography, for example. Even in well settled fields like semiconductor physics a deeper understanding is necessary, e.g., to scale circuits down, make them more reliable, or even to replace them by newer technologies like quantum circuits. Other topics in focus are quantum interference and quantum coherence, but also nonlinear optical phenomena which are intensively discussed nowadays. There are numerous possible applications of these results: Quantum circuits, sensors, molecules, or, more related to this thesis' field, the coherent control of atomic motion or secure communication with entangled photons.

A macroscopic body's motion is well understood in classical physics. At a microscopic level, a particle's motion is not yet completely understood. One may inquire into the trajectories of these particles, as, for example, Bohm did before [BH93], though the solutions therefore are widely spread in literature. Recently, averaged trajectories of photons have been reported [Bli13; Koc11] which obey also the rules of quantum mechanical theory.

A few years ago a French group around Yves Couder and Emmanuel Fort discovered the existence of quantum-type rules at macroscopic level in practical experiments using oil droplets bouncing on a vibrating oil bath [CF06; Edd09; For10; Pro06]. Investigations on those experiments showed that there is a kind of particle-wave duality similar to the explanation of de Broglie [CF12; dBro60; Har13].

One aspect of this work is to adapt de Broglie's particle-wave duality to microscopic level in order to investigate the energy exchange so that a model for the interaction between the particle and the wave can be specified. For simplicity, the description is restricted to one-dimensional, nonrelativistic cases. At the beginning, a classical particle behaves as a damped oscillator which also carries out a random motion that is superposed to the oscillatory motion. The necessary conditions to keep both motions alive will be shown and the energy balance will be derived. Accordingly, these conditions are shown to enforce natural motions, i.e. moving particles, and even accelerated ones being prevented of radiating. This adaptation has been published in reference [Grö11b; Sch12].

Another aspect concerns the motion of those particles: While in literature [Hol82; SM12] the quantum mechanical equations are solved, herein a different description of

a particle's motion will be developed which also simplifies the numerical calculations concerning the random motion carried out by the particle, its averaged motion and also the trajectories of particles, their velocities and probability currents. By setting initial probability distributions right after a single slit, or even multiple slits, the conditions of the decay of these distributions can be studied. It will be shown that the decay obeys a ballistic diffusion which leads to an explanation of interference effects, velocities and densities, and even to calculatory rules for the probability distributions, and the associated probability currents. If the intensities of two beams of a double-slit experiment provide big differences then the low-intensity beam is swept aside, away from the high-intensity beam. It is suggested to record the intensities at a screen perpendicular to the double-slit setup. Parts of this aspect have already been shown in [Fus14; Grö10b; Grö12b; Grö15a; Mes13].

These two aspects are of course closely tied to each other since the particle's motion inherits the waves' motion that itself influences the particle again, which has also been referred to in further publications of our group [Grö10a; Grö11a; Grö12a; Grö12c; Grö13; Grö14a; Grö14b; Mes12; Sch12].

A last aspect of the present work is the description of the numerical means to simulate a particle's motion. The mathematical background for the derivation and calibration of simulation tools is provided. Furthermore, the limitations one is confronted with when using these tools will be shown.

The theoretical framework presented herein has been worked out in tight cooperation with all members of our group. Accordingly, this thesis contains parts of our already published content, yet enhanced and completed to give a picture of what has been developed so far. The numerical treatment of the second part as well as the whole simulation procedure including programming has been worked out by myself. The practicability of the derived framework is demonstrated herein with numerous images obtained by these simulations.

1. The fluid droplet picture adapted to quantum mechanics

Inspired by the experiments of Couder and Fort's group who show that a macroscopic particle may both regularly oscillate in time with its characteristic frequency *and* propagate irregularly in space, we distinguish between these two types of motion and call the former *bouncer* and the latter *walker*. We discuss this two-fold perspective of an individual particle and discuss an analogous sub-quantum model simultaneously characterized by regular periodic and stochastic motions, both of which must, however, be comparable on the level of the work-energy expended during a certain amount of time. We shall calculate the respective work-energies for each aspect separately, afterwards they will be compared during the same time-span.

We assume that phenomena of standard quantum mechanics like Planck's energy relation or the Schrödinger equation can be assessed as the property of the vacuum combined with diffusion processes reflecting also a stochastic nature. Thus we obtain the quantum mechanical results as an averaged behaviour of sub-quantum processes. [Grö11b; Sch12]

1.1. The macroscopic fluid droplet

Masses and waves are well-known constitutive elements of classical physics. The idea of the wave-particle duality had no equivalent on a macroscopic scale for a long time until a small group of French physicists around Yves Couder [CF06; CF12; Cou05; Cou10; Edd09; For10; Pro06] published experiments providing bouncing masses and waves coupled tight, on the one hand, but being different objects on the other hand. More curious is the fact that both, the waves and the bouncing masses comprised of the same substance in those experiments, i.e. silicon oil.

Consider a coffee machine comprising a filter containing the coffee powder and a glass pot where the finished coffee is collected at last. Every now and then a brown coffee droplet goes down from the filter into the glass pot, falls on the surface of the same liquid and disappears rapidly. Sometimes the droplet bounces back from that surface

for two or three times thereby leaving some waves on the surface. Everybody knows that, however, the French scientists asked themselves how they could keep the droplets bouncing for a longer time. Therefore, they replaced the static pot by a vertically vibrating bath and the coffee by silicon oil because of its higher viscosity. Surprisingly, the droplet kept bouncing without disappearing for a long time, even in the order of hours or days.

Due to the vertical vibration of the bath, the characteristic acceleration thereby being generated causes the droplet to bounce on the surface periodically. As the droplet collides with the interface, it remains separated by a continuous air film. Before this air film can break, the droplet lifts off again. At each successive bounce, the droplet forms a surface wave which is thereby attenuated so that the force acting on the droplet guides it towards the next surface point and so on. Couder and his group then showed that by controlling the vibrating bath the droplets can be guided along artificial paths reminiscent of quantum mechanics.

If those macroscopic experiments are able to reproduce – to a certain extent – quantum mechanical experiments like diffraction of a single object or double-slit interference, then at least it should be worth to investigate this mechanism peculiarly with regard to quantum mechanical similarities. This has also been suggested by other authors, for example by Brady and Anderson [BA14] or Richardson *et al.* [Ric14]. In other words, consider the bouncing mass to be an elementary particle like an electron or a neutron whose intrinsic oscillation generates and affects the wave-like landscape around itself. Of course, this wave-like landscape has to be built up in an underlying sub-structure of the vacuum, the sub-quantum medium, combined with diffusion processes.

According to Couder’s experiments we distinguish between these two types of motion and call them *bouncer* and *walker*, respectively. We discuss this two-fold perspective of an individual particle and, after individual inspection, these two tools will be compared, or coupled, respectively. We are interested in reproducing the energy exchange and conservation between these two types of motion with respect to well-known quantum mechanical principles. We assume that phenomena of standard quantum mechanics like Planck’s energy relation or the Schrödinger equation can be assessed as the emergent property of an underlying sub-structure of the vacuum combined with diffusion processes reflecting also the stochastic parts of the zero-point field, i.e. the zero-point fluctuations [CdIP12; dlPeñ14; Grö08; Grö09; Grö10b]. With respect to an analogous sub-quantum model, then, this means that the *zitterbewegung* is simultaneously characterized by regular periodic and stochastic motions, both of which must, however, be comparable on the level of the work-energy expended during a certain amount of time. We shall calculate the respective work-energies for each aspect separately, afterwards they will be compared during the same time-span. This will lead to requirements which have to be fulfilled by a such modelled quantum mechanical system. Thus we obtain

the quantum mechanical results as an averaged behaviour of sub-quantum processes.

1.2. A classical oscillator: The bouncer

We assume a system comprising two subsystems, the first one is a harmonic oscillator and the second one undergoes a Brownian-type motion [Grö11b; Sch12]. To recall the above-mentioned picture, one could consider Couder's droplet: The droplet bounces on a wave, thus the droplet itself represents the harmonic oscillator which, at the same time, moves along together with a wave driven by the oscillations. Here, in a first step, we focus on the harmonic oscillation of the first subsystem.

We can write down the following Newtonian equation of a classical forced oscillator with friction (see any good textbook, e.g. [Dem06]) with one degree of freedom

$$m\ddot{x} + m\omega_0^2 x + 2\gamma m\dot{x} = F_0 \cos \omega t. \quad (1.1)$$

Equation (1.1) describes a forced oscillation of a mass m swinging around a centre point along $x(t)$. The resonant angular frequency is ω_0 for the case m would swing freely. Due to the damping/friction γ of the swinging particle, for periodic motion there is a need for a locally independent driving force $F_0 \cos \omega t$.

The general solution of the inhomogeneous equation (1.1) comprises a general solution of the homogeneous equation (the left hand side of Eq. (1.1)) plus a special solution of the inhomogeneous equation. Accordingly, the general solution must be of form

$$x(t) = r_1 e^{-\gamma t} \cos(\omega_1 t + \varphi_1) + r \cos(\omega t + \varphi). \quad (1.2)$$

After short calculation $\omega_1 = \sqrt{\omega_0^2 - \gamma^2}$ appears as the frequency of the free damped oscillation.

However, for $t \gg \gamma^{-1}$ the amplitude $r_1 e^{-\gamma t}$ of the first term vanishes, thus γ^{-1} plays the role of a relaxation time. The second term remains and represents a stationary solution of Eq. (1.1),

$$x(t) = r \cos(\omega t + \varphi). \quad (1.3)$$

As we suppose the oscillator to be in a steady state we are only interested in the stationary solution (1.3) further on. By substitution of (1.3) into (1.1) we find after some calculations for the phase shift between the forced oscillation and the forcing oscillation that

$$\tan \varphi = -\frac{2\gamma\omega}{\omega_0^2 - \omega^2}, \quad (1.4)$$

and for the amplitude of the forced oscillation

$$r(\omega) = \frac{F_0/m}{\sqrt{(\omega_0^2 - \omega^2)^2 + (2\gamma\omega)^2}}. \quad (1.5)$$

Next, we derive the work-energy W_{bouncer} of the stationary system for $t \gg \gamma^{-1}$ and $\omega = \omega_0$. From (1.3) we find for the kinetic energy of the harmonic oscillator that

$$E_{\text{kin}} = \frac{1}{2}m\dot{x}^2 = \frac{1}{2}m\omega^2 r^2 \sin^2(\omega t + \varphi) \quad (1.6)$$

and from (1.1) for the potential energy

$$E_{\text{pot}} = \int_0^x m\omega_0^2 x \, dx = \frac{1}{2}m\omega_0^2 x^2 = \frac{1}{2}m\omega_0^2 r^2 \cos^2(\omega t + \varphi). \quad (1.7)$$

Therefore, the sum of the kinetic and the potential energy reads

$$\begin{aligned} E &= E_{\text{kin}}(t) + E_{\text{pot}}(t) = \frac{1}{2}m\dot{x}^2 + \frac{1}{2}m\omega_0^2 x^2 \\ &= \frac{1}{2}mr^2 \left[\omega^2 \sin^2(\omega t + \varphi) + \omega_0^2 \cos^2(\omega t + \varphi) \right] \\ &= \frac{1}{2}mr^2 \left[\omega^2 + (\omega_0^2 - \omega^2) \cos^2(\omega t + \varphi) \right] \end{aligned} \quad (1.8)$$

Generally, energy E oscillates for $\omega \neq \omega_0$ whereas for $\omega = \omega_0$ Eq. (1.8) reduces to

$$E \Big|_{\omega \rightarrow \omega_0} = \frac{1}{2}m\omega_0^2 r^2 = \text{const.} \quad (1.9)$$

This means, the damped, forced system turns out to be stationary if it is driven at the resonance frequency $\omega = \omega_0$ of the free undamped oscillator.

For $\omega = \omega_0$ we obtain the work-energy multiplying Eq. (1.1) with \dot{x}

$$m\dot{x}\ddot{x} + m\omega_0^2 x\dot{x} = -2\gamma m\dot{x}^2 + F_0 \cos(\omega_0 t)\dot{x} \quad (1.10)$$

which can also be written as

$$\frac{d}{dt} \left(\frac{1}{2}m\dot{x}^2 + \frac{1}{2}m\omega_0^2 x^2 \right) = -2\gamma m\dot{x}^2 + F_0 \cos(\omega_0 t)\dot{x}. \quad (1.11)$$

In parentheses on the left hand side one easily recognizes the sum of the kinetic and the potential energy of Eq. (1.8) which is constant for a stationary solution (1.3), which is

why the l.h.s. of Eq. (1.11) equals zero. As Eq. (1.11) provides the power balance of the forced oscillator, we identify the damping of $-2\gamma m\dot{x}^2$ as the expended power going off the oscillator to the bath, whereas, in turn, $F_0 \cos(\omega_0 t)\dot{x}$ represents the power which is regained from the energy bath and applied back to the system. We conclude that the driving force and the friction force have to cancel each other

$$F_0 \cos(\omega_0 t) = 2\gamma m\dot{x} = -2\gamma m\omega_0 r \sin(\omega_0 t + \varphi). \quad (1.12)$$

We get

$$F_0 = 2\gamma m\omega_0 r, \quad \varphi = -\frac{\pi}{2} \quad (1.13)$$

and thus

$$x(t) = r \sin(\omega_0 t), \quad \dot{x}(t) = \omega_0 r \cos(\omega_0 t), \quad r = \frac{F_0}{2\gamma m\omega_0}. \quad (1.14)$$

One can write down the net work-energy that is taken up by the bouncer during each period $\tau = \frac{2\pi}{\omega_0}$ as

$$\begin{aligned} W_{\text{bouncer}} &= \int_0^\tau F_0 \cos(\omega_0 t)\dot{x} dt = \int_0^\tau 2\gamma m\dot{x}^2 dt \\ &= 2\gamma m\omega_0^2 r^2 \int_0^\tau \cos^2(\omega_0 t) dt = \gamma m\omega_0^2 r^2 \tau = 2\pi\gamma m\omega_0 r^2. \end{aligned} \quad (1.15)$$

Let us recall that W_{bouncer} is the energy floating in one period from the energy bath via the oscillator to friction energy. In addition, we have the constant energy as mentioned in connection with Eq. (1.11) of the oscillator. Further on, we call this constant energy E_{bouncer} , which is the energy (1.9) of the linear harmonic oscillator whose mean energies are given by Eqs. (1.6) and (1.7) together with (1.14) by¹

$$\langle E_{\text{kin}} \rangle = \langle E_{\text{pot}} \rangle = \frac{1}{4}m\omega_0^2 r^2, \quad E = \langle E_{\text{kin}} \rangle + \langle E_{\text{pot}} \rangle = \frac{m\omega_0^2 r^2}{2}. \quad (1.16)$$

In our work [Grö11b] we are concerned about the lowest energy of a harmonic oscillator. From quantum mechanics we know that this lowest energy is $\hbar\omega_0/2$. In order to bring this classical harmonic oscillator in a quantum mechanical context, we request

$$E_{\text{bouncer}} := E = \frac{m\omega_0^2 r^2}{2} = \frac{\hbar\omega_0}{2}, \quad (1.17)$$

¹We shall use different symbols for mean values over space \bar{x} , and mean values over time $\langle x \rangle$, if not otherwise noted (see e.g. [Sch06]).

where the symbol E_{bouncer} assigns the energy to the bouncer system. From Eq. (1.17) we immediately find that

$$mr^2\omega_0 = \hbar. \quad (1.18)$$

For the work-energy W_{bouncer} of Eq. (1.15) we get

$$W_{\text{bouncer}} = 2\pi\gamma\hbar. \quad (1.19)$$

In the generalized case of an N -dimensional space, we can separate each dimension with the use of Eq. (1.3) and get for the oscillators' amplitudes,

$$\begin{aligned} x_1(t) &= r_{x_1} \cos(\omega_0 t + \phi_{x_1}), \\ &\vdots \\ x_N(t) &= r_{x_N} \cos(\omega_0 t + \phi_{x_N}). \end{aligned} \quad (1.20)$$

We obtain the work-energy during each single period τ by integrating over the N components (1.20) and get

$$W_{\text{bouncer}} = \int_{\tau} 2\gamma m (\dot{r}_{x_1}^2 + \dots + \dot{r}_{x_N}^2) dt = N\gamma m \omega_0^2 r^2 \tau \quad (1.21)$$

with

$$r^2 = r_{x_1}^2 = \dots = r_{x_N}^2. \quad (1.22)$$

Assuming again (1.18), we can write down for any number N of dimensions that

$$W_{\text{bouncer}} = 2\pi N\gamma\hbar. \quad (1.23)$$

1.3. Brownian motion of a particle: The walker

After having discussed the first subsystem which fulfilled a harmonic oscillation, we focus on the second subsystem which obeys a Brownian motion, embedded in an environment comprising an energy bath with a white noise driving force (cf. [Cof04]). The latter oblige the subsystem to undergo rapid and random movements due to statistical independent kicks of random magnitude and direction.

The Brownian motion of a thus characterized particle, which we call a walker, is then described by a Langevin stochastic differential equation with velocity $u = \dot{x}$, a time-dependent stochastic force $f(t)$, and friction coefficient ζ (c.f. [Sch06, chapter 8.1] and [Cof04; UO30]),

$$m\dot{u} = -m\zeta u + f(t), \quad t \geq 0 \quad (1.24)$$

which describes stochastic processes which we investigate for $t \geq 0$ only. Since the force $f(t)$ is stochastic – and hence is the velocity stochastic – one has as usual for the averages

$$\langle f(t) \rangle = 0, \quad \langle f(t)f(t') \rangle = \phi(t - t'), \quad (1.25)$$

where $\phi(\tau)$ differs noticeably from zero only for intervals $\tau < \tau_c$. The correlation time τ_c denotes the time during which the fluctuations of the stochastic force remain correlated². We are only interested in the Brownian-type motion of the particle, therefore we restrict ourselves to $\tau \gg \tau_c$ that further allows us to introduce a coefficient λ that measures the strength of the mean square deviation of the stochastic force, such that

$$\phi(\tau) = \lambda\delta(\tau). \quad (1.26)$$

One solves the Langevin equation with the help of the retarded Green's function $G(t)$

$$\dot{G} + \zeta G = \delta(t), \quad G(t) = \Theta(t)e^{-\zeta t} \quad (1.27)$$

with the Heaviside step function $\Theta(t) = \int_{-\infty}^t \delta(\tau) d\tau$. Letting

$$u(t=0) = u_0 \quad (1.28)$$

be the initial value of the velocity, one obtains

$$\begin{aligned} u(t) &= u_0 e^{-\zeta t} + \int_0^\infty d\tau G(t - \tau) f(\tau) / m \\ &= u_0 e^{-\zeta t} + e^{-\zeta t} \int_0^t d\tau e^{\zeta \tau} f(\tau) / m. \end{aligned} \quad (1.29)$$

Using this solution and the assumptions (1.25) we find for the mean value of the velocity³

$$\langle u(t) \rangle = \underbrace{\langle u_0 \rangle}_{=u_0} e^{-\zeta t} + \int_0^t d\tau e^{-\zeta(t-\tau)} \underbrace{\langle f(\tau) \rangle}_{=0} / m = u_0 e^{-\zeta t}, \quad (1.30)$$

²Under the precondition that the collisions of the particles undergoing a Brownian motion are completely uncorrelated, the correlation time is roughly equal to the duration of a collision. [Sch06]

³The mean value $\langle \rangle$ can be understood either as an average over time or an average over an ensemble at a fixed time, $\langle x(t) \rangle = \int_{-\infty}^\infty x P(x, t) dx$. For a stationary process the mean value is constant because of $P(x, t) = P(x)$ (see e.g. [BY07; Sch06]).

where no average is involved over the friction terms because they are constant describing the averaged interaction of the system with the bath. Therefore, one does not consider the average value of $u(t)$, but instead that of its square,

$$\begin{aligned}
 \langle u^2(t) \rangle &= \langle u_0^2 \rangle e^{-2\zeta t} + 2e^{-2\zeta t} \int_0^t d\tau e^{\zeta\tau} \underbrace{\langle u_0 f(\tau) \rangle}_{=0} \frac{1}{m} \\
 &\quad + e^{-2\zeta t} \int_0^t d\tau \int_0^t d\tau' e^{\zeta(\tau+\tau')} \langle f(\tau') f(\tau) \rangle \frac{1}{m^2} \\
 &= u_0^2 e^{-2\zeta t} + e^{-2\zeta t} \int_0^t d\tau \int_0^t d\tau' e^{\zeta(\tau+\tau')} \phi(\tau - \tau') \frac{1}{m^2} \\
 &= u_0^2 e^{-2\zeta t} + \frac{\lambda}{2\zeta m^2} (1 - e^{-2\zeta t}) \xrightarrow{t \gg \zeta^{-1}} \frac{\lambda}{2\zeta m^2}
 \end{aligned} \tag{1.31}$$

where the velocity u_0 at $t = 0$ is independent of and hence uncorrelated with the random force $f(t)$ and hence $\langle u_0 f(\tau) \rangle = \langle u_0 \rangle \langle f(\tau) \rangle = 0$. For $t \gg \zeta^{-1}$, the term containing u_0 becomes negligible, i.e. ζ^{-1} then plays the role of a relaxation time. We require that our particle attains thermal equilibrium [Grö08; Grö09] after long times so that due to the *equipartition theorem on the sub-quantum level*⁴ the average value of the kinetic energy becomes

$$\langle E_{\text{kin}} \rangle = \frac{1}{2} m \langle u^2(t) \rangle \xrightarrow{t \gg \zeta^{-1}} \frac{\lambda}{4\zeta m} =: E_{\text{zp}}, \tag{1.32}$$

with E_{zp} being the average kinetic energy of the zero-point field. One can define the E_{zp} per degree of freedom as⁵

$$E_{\text{zp}} := \frac{kT_0}{2} \tag{1.33}$$

with k being a constant equivalent to Boltzmann's constant k_{B} , and T_0 denotes the vacuum temperature in our scenario in close analogy to the usual thermodynamical formalism.

⁴We assume the equipartition theorem to be the same and hence borrowed from classical statistical mechanics.

⁵As we are probably at a length scale where the thermodynamical laws have not yet proven valid, we stick to formally using E_{zp} . Surely, Eq. (1.33) is the sub-quantum analogon to the thermodynamical expression $k_{\text{B}}T/2$, however, as for today we neither know T_0 nor the constant k – unless it should turn out as identical to k_{B} .

Next we derive the velocity correlation function

$$\begin{aligned}
 \langle u(t)u(t') \rangle &= \langle u_0^2 \rangle e^{-\zeta(t+t')} + e^{-\zeta(t+t')} \int_0^t d\tau \int_0^{t'} d\tau' e^{\zeta(\tau+\tau')} \langle f(\tau)f(\tau') \rangle \frac{1}{m^2} \\
 &\quad + e^{-\zeta(t+t')} \left(\int_0^t d\tau e^{\zeta\tau} \underbrace{\langle u_0 f(\tau) \rangle}_{=0} + \int_0^{t'} d\tau e^{\zeta\tau} \underbrace{\langle u_0 f(\tau) \rangle}_{=0} \right) \frac{1}{m} \\
 &= u_0^2 e^{-\zeta(t+t')} + e^{-\zeta(t+t')} \int_0^t d\tau \int_0^{t'} d\tau' e^{\zeta(\tau+\tau')} \delta(\tau - \tau') \frac{\lambda}{m^2} \\
 &= \frac{\lambda}{2\zeta m^2} e^{-\zeta|t-t'|} + \left(u_0^2 - \frac{\lambda}{2\zeta m^2} \right) e^{-\zeta(t+t')}.
 \end{aligned} \tag{1.34}$$

For $t, t' \gg \zeta^{-1}$ one can neglect the last term in (1.34). Then, one obtains the mean square displacement of $x(t)$ by integrating (1.34) twice, assuming $x(0) = 0$, which yields ⁶

$$\langle x^2(t) \rangle = \int_0^t d\tau \int_0^t d\tau' \frac{\lambda}{2\zeta m^2} e^{-\zeta|\tau-\tau'|} \xrightarrow{t \gg \zeta^{-1}} \frac{\lambda}{\zeta^2 m^2} t = 2Dt, \tag{1.35}$$

with the diffusion constant

$$D = \frac{\lambda}{2\zeta^2 m^2} = \frac{2E_{\text{zp}}}{\zeta m}. \tag{1.36}$$

Next, we calculate the work-energy W_{walker} of the stationary system. We remind ourselves that we have to do with a steady-state system. Due to the friction ζ , there exists a flow of (kinetic) energy into the environment. Consequently, there must also exist a work-energy flow back into our system of interest. Therefore, we calculate the averaged power by multiplying Eq. (1.24) by $u = \dot{x}$ and obtain an averaged power-balance equation

$$m \langle \ddot{x}\dot{x} \rangle = -m\zeta \langle \dot{x}^2 \rangle + \langle f(t)\dot{x} \rangle. \tag{1.37}$$

In contrast to Eq. (1.10) we are dealing with stochastic variables and thus we are fine with averaged values for the power-balance. Even though, we assume in close analogy

⁶We stress that even if we use the same character x as for the oscillating particle, now the meaning is different: $x(t)$ in section 1.2 signified a deterministic harmonic displacement of mass point m in the case of an oscillating particle (bouncer), whereas $x(t)$ now means a stochastic random walk variable for the particle that carries out a Brownian motion of the walker.

to Eq. (1.10), that the average system's energy being constant due to a stationary state of the system. Therefore, the terms on the right hand side of Eq. (1.37) providing the power balance must cancel. This yields for the duration of time τ the net work-energy of the walker

$$W_{\text{walker}} = \int_{\tau} m\zeta \langle \dot{x}^2 \rangle dt = \int_{\tau} m\zeta \langle u^2 \rangle dt. \quad (1.38)$$

Here, we want to ensure that the work-energy we shall obtain is comparable with Eq. (1.19). Therefore, we choose the basic time interval $\tau = 2\pi/\omega_0$ of the walker-system the same as in Eq. (1.14) of the bouncer-system. Furthermore, as we are dealing with a walker-system that obeys a stochastic motion, we have to work with mean values to make all fluctuating contributions negligible due to averaging over these statistical variations.

Inserting (1.32) into (1.38), we obtain

$$W_{\text{walker}} = \tau m\zeta \langle u^2(t) \rangle = 2\tau\zeta E_{\text{zp}}. \quad (1.39)$$

The work-energy for the particle undergoing Brownian motion can thus be written as

$$W_{\text{walker}} = \frac{4\pi}{\omega_0} \zeta E_{\text{zp}}. \quad (1.40)$$

Turning now to the N -dimensional case, the average squared velocity of a particle is

$$\langle u^2 \rangle = \langle u_{x_1}^2 \rangle + \dots + \langle u_{x_N}^2 \rangle, \quad (1.41)$$

with equal probability for each direction,

$$\langle u_{x_1}^2 \rangle = \dots = \langle u_{x_N}^2 \rangle = \frac{1}{N} \langle u^2 \rangle. \quad (1.42)$$

Accordingly, the average kinetic energy of a moving particle with N degrees of freedom becomes

$$E_{\text{zp}}^{(N)} = \frac{1}{2} m \langle u^2 \rangle = N E_{\text{zp}} \quad (1.43)$$

and thus

$$\langle u^2(t) \rangle = 2N \frac{E_{\text{zp}}}{m}. \quad (1.44)$$

Again, we note that Eq. (1.44) describes an energy equipartition which, however, here relates to the sub-quantum level, i.e. to the vacuum temperature T_0 . It should

thus not be confused with the equipartition theorem as discussed, e.g. with respect to blackbody radiation and the Planck spectrum.

With the analogical explanation as for the one-dimensional case, we find for the work-energy of the walker in N -dimensional space

$$W_{\text{walker}} = m\zeta \int_{\tau} \left[\langle u_{x_1}^2(t) \rangle + \cdots + \langle u_{x_N}^2(t) \rangle \right] dt = m\zeta \int_{\tau} \langle u^2(t) \rangle dt. \quad (1.45)$$

Inserting (1.44), we obtain

$$W_{\text{walker}} = \tau m \zeta \langle u^2(t) \rangle = 2\tau \zeta N E_{\text{zp}}, \quad (1.46)$$

which is N times the value of the one-dimensional case in Eq. (1.40). Therefore, the work-energy for the particle undergoing Brownian motion can be written as

$$W_{\text{walker}} = \frac{N4\pi}{\omega_0} \zeta E_{\text{zp}}, \quad (1.47)$$

for the general case of N degrees of freedom.

1.4. The walking bouncer

Our model of a single-particle quantum system comprises a bouncer-system and a walker-system. So far, we have analysed these two systems independently. Now we construct an energy exchange mechanism for our model where we assume a continuous energy flow from the bath to the oscillator, and *vice versa*. Accordingly, the walker gains its energy from the heat bath via the oscillations of the bouncer–bath system in N dimensions: The bouncer pumps energy to and from the heat bath via the friction γ .

In the centre of mass frame, the system is characterized by a single degree of freedom. However, in the N -dimensional reference frame of the laboratory, the oscillation is not fixed *a priori*. Rather, possible exchanges of energy will be equally distributed in a stochastic manner. Concerning the latter, the flow of energy is on average distributed evenly via the friction γ in all N dimensions of the laboratory frame. It can thus also be considered as the stochastic source of the particle moving in N dimensions, each described by the Langevin equation (1.24).

Therefore, we recognize *friction* in both cases, as represented by γ and ζ , respectively, to generally describe the coupling between the oscillator (or particle in motion) on the one hand, and the bath on the other hand. Moreover, and most importantly, during that flow, the averaged coupling of the bouncer can be assumed to be exactly identical with

the coupling of the walker. For this reason we directly compare the results of Eqs. (1.23) and (1.47),

$$W_{\text{bouncer}} = W_{\text{walker}}, \quad (1.48)$$

providing

$$2\pi N\gamma\hbar = \frac{N4\pi}{\omega_0}\zeta E_{\text{zp}}. \quad (1.49)$$

Now, our single-particle quantum model consists of two parts, each of which possesses a certain energy, which we expressed by Eqs. (1.17) and (1.32), respectively. Even described by two different mechanisms, the bouncer-system and the walker-system are still two different aspects of our assumed single-particle quantum model. Therefore, the energy E of each system must be the same, being the minimum energy of the single particle. We derived the energies of the sub-systems as

$$E_{\text{bouncer}} = \frac{m\omega_0^2 r^2}{2} = \frac{\hbar\omega_0}{2} \quad (1.50)$$

being the energy of the bouncer and as

$$E_{\text{zp}} = \frac{kT_0}{2} \quad (1.51)$$

being energy of the walker, respectively. Comparing these two equations yields

$$\frac{\hbar\omega_0}{2} = \frac{kT_0}{2} \quad (1.52)$$

and hence the zero-point energy in terms of $\hbar\omega$ reads as

$$E_{\text{zp}} = \frac{\hbar\omega_0}{2}. \quad (1.53)$$

Substituting this result into Eq. (1.49) leads directly to

$$\gamma = \zeta \quad (1.54)$$

which means the bouncer and the walker are coupled with the same strength to the ZPF bath, i.e. the friction coefficient for both the bouncer and the walker is identical.

For a quantitative derivation of the friction coefficients of both the bouncer and the walker, we introduce the action function $S(\mathbf{x}, t)$ such that the total energy of the whole system is given by

$$E_{\text{tot}}(\mathbf{x}, t) = -\frac{\partial S(\mathbf{x}, t)}{\partial t}. \quad (1.55)$$

We need to specify that a quantum system's total energy consists of the energy of the system of interest (i.e., the particle with frequency ω_0), and of some term representing energy throughput related to the surrounding vacuum, i.e. effectively some function F of the heat flow ΔQ , [Grö08]

$$E_{\text{tot}}(\mathbf{x}, t) = E(\omega_0, \mathbf{x}, t) + F[\Delta Q(\mathbf{x}, t)]. \quad (1.56)$$

The first term in Eq. (1.56) corresponds to a particle's energy. The second term, being equivalent to some kinetic energy, can be recast with the aid of a fluctuating momentum term, $\delta\mathbf{p}$, of the particle with momentum \mathbf{p} , by

$$F[\Delta Q(\mathbf{x}, t)] = \frac{(\delta\mathbf{p})^2}{2m}. \quad (1.57)$$

We consider as usual the momentum \mathbf{p} of the particle as given by

$$\mathbf{p}(\mathbf{x}, t) = \nabla S(\mathbf{x}, t) = m\mathbf{v}, \quad (1.58)$$

noting, however, that this will not be the effective particle momentum yet, due to the additional momentum coming from the heat flow, described by momentum fluctuation of Eq. (1.57) as

$$\delta\mathbf{p} = \delta(\nabla S) = \nabla(\delta S) := m\mathbf{u}, \quad (1.59)$$

where velocity \mathbf{u} is assumed to be the same as in the Langevin equation (1.24). Our task is now to find an adequate expression for $\delta\mathbf{p}$ from our central assumption, i.e., from an underlying nonequilibrium thermodynamics. To begin, we remember the distinction between “heat” as disordered internal energy on one hand, and mechanical work on the other: heat as disordered energy cannot be transformed into useful work by any means. According to Boltzmann, if a particle trajectory is changed by some supply of heat ΔQ to the system, this heat will be spent either for the increase of disordered internal energy, or as ordered work furnished by the system against some constraint mechanism, [Bol66]

$$\Delta Q = \Delta E_{\text{internal}} + \Delta W_{\text{constraints}}. \quad (1.60)$$

Now, in order to proceed in our quest to obtain an expression for the momentum fluctuation (1.59) from our thermodynamical approach, we can again rely on a formula originally derived by Ludwig Boltzmann. As mentioned above, Boltzmann considered the change of a trajectory by the application of heat ΔQ to the system. Considering a very slow transformation, i.e., as opposed to a sudden jump, Boltzmann derived a formula which is easily applied to the special case where the motion of the system of interest is oscillating with some period $\tau = 2\pi/\omega_0$. Boltzmann's formula for periodic

systems (A.50) relates the applied heat ΔQ to a change in the action function (A.45) $S = \int (E_{\text{kin}} - V) dt$, i.e., $\delta S = \delta \int E_{\text{kin}} dt$, providing⁷

$$\Delta Q = 2\omega_0 \delta S = 2\omega_0 [\delta S(\tau) - \delta S(0)]. \quad (1.61)$$

The gradient reads as

$$\nabla Q = 2\omega_0 \nabla(\delta S), \quad (1.62)$$

with abbreviation $\nabla(\Delta Q) =: \nabla Q$, which leads by using (1.59) to

$$m\mathbf{u} = \frac{\nabla Q}{2\omega_0}. \quad (1.63)$$

As the friction force in Eq. (1.24) is equal to the gradient of the heat flux,

$$m\zeta\mathbf{u} = \nabla Q, \quad (1.64)$$

comparison of (1.63) and (1.64) together with (1.54) provides

$$\zeta = \gamma = 2\omega_0. \quad (1.65)$$

Note that with Eqs. (1.53) and (1.65) one obtains in any one dimension the expression for the diffusion constant (1.36) as

$$D = \frac{2E_{\text{zp}}}{\zeta m} = \frac{\hbar}{2m}, \quad (1.66)$$

which is exactly the usual expression for D in the context of quantum mechanics.

1.5. Conclusions and perspectives

In this chapter a new type of objects has been presented obeying the laws of Newtonian mechanics which can exhibit simultaneously particle and wave properties. As a prerequisite, classical non-equilibrium thermodynamics has been assumed, i.e. a mechanism of stationary energy flow, which enables a work-energy exchange between an oscillating bouncer and a stochastically driven walker. It has been shown that such an exchange can be derived with two classical differential equations, the Newtonian equation and the Langevin equation, together describing the two-fold perspective of a single particle called the walking bouncer. Each of these equations contains a friction factor, which

⁷The period τ is assumed to remain constant during a change ΔQ .

has been shown to be equal for both equations, on the one hand, and responsible for the coupling and hence the characteristic feature of the transfer, on the other hand.

Both equations used, the Newtonian and the Langevin equation, are classical equations leading naturally to classical solution. To build a connection to the quantum regime, the minimum energy of a quantum oscillator has been used to introduce energy quantisation. Once applied this step, all used attributes turned out to be equal to the ones known from quantum mechanics, especially the diffusion constant.

The given picture leaves open which part, the bouncer or the walker, is the sender of the energy transfer and which one the receiver of the exchanged energy, respectively. Certainly, one could surely find an answer for macroscopic particles when taking a close look at Couder's experiments. However, one should not expect to determine thereby an adequate answer for the mechanism translated into the language of quantum mechanics as the model presented herein should rather be considered a toy-model hopefully giving one a clue to find a precise mathematical description of the whole system underlying quantum mechanics. In this sense, the derived walking bouncer should be recognized as a model for further discussions on how an object could act as a particle and a wave simultaneously, thereby replacing the old fashioned picture of an object that could either act as a particle or a wave, dependent on particular circumstances.

In the following chapters we will implicitly make use of such type of a particle, even though the zitterbewegung, modelled by the stochastic movement of the walker, will silently disappear in the mathematical description due to averaging processes. This also means we shall leave here the level of stochastic description and turn towards a phenomenological approach of a particle's behaviour, i.e. the decay of a Gaussian distribution.

2. Probability distributions and velocities

Following the same idea as in section 1.1, it should be worth to investigate the mechanism of the microscopic picture of the fluid droplet in particular with regard to underlying processes. Also, Bohmian theory gives an answer to this question, however, with regard to the underlying diffusion processes, we shall in fact find a different answer: In this chapter we shall provide a completely different view of the diffusion process which emerges out of uncorrelated Gaussian position distributions as well as momentum distributions, with the spreading of the resulting wave packet being characterized as a ballistic diffusion.

By introducing a slit setup which will serve as the main environment to our investigations further on, it is sufficient to analyse one-dimensional distributions only. In a further step, we shall derive the ballistic diffusion equation which allows us the complete description of the spreading wave packet.

2.1. Outline

Based on the results derived in chapter 1, we move now towards a phenomenological approach of a particle's behaviour. Therefore, we assume the particles to emerge from a source one by one propagating through a slit, and finally hitting a screen becoming visible, or being measured there. According to our discussion in chapter 1, we model a system in which each single particle obeys the random motion of Brownian-type. We draw conclusion from the measurement patterns of such experiments that in the average of a sufficiently big number of single events we can assume smooth trajectories thereby describing the influence of an underlying diffusion process. In order to keep things simple, we always assume an aperture with whose edges the particle's interaction is negligible. Furthermore, we restrict our investigations to Gaussian-shaped probability distributions only, as this is a function class widely used in physical theory, which reproduces all the quantum measurements considered herein. As a result, such a smooth diffusion process

will turn out to be a ballistic diffusion¹.

2.2. The constituting setup

For the following, it will be helpful to let ourselves be guided by the picture provided by the walkers² introduced in chapter 1.3. For also with a walker, one is confronted with a rapidly oscillating object, which itself is guided by an environment that also contributes some fluctuating momentum to the walker’s propagation. In fact, the walker creates waves surrounding the particle, and the detailed structure of the wave configurations influences the walker’s path, just as in our approach the particle, both absorbs heat from and emits heat into its environment, which can be described in terms of momentum fluctuations.

If we imagine the bouncing of a walker in its fluid environment, the latter will become excited or heated up wherever the momentum fluctuations direct the particle to. After some time span – which can be rather short, considering the very rapid oscillations of elementary particles – a whole area of the particle’s environment will be modified by the throughput of energy in this way. Considering the electron, for example, the fact that it bounces roughly 10^{21} times per second, with each bounce eventually providing a slight displacement from the original path’s momentum, one can thus understand the area filling capacity of any quantum path.

Now, let us assume we have a source of identical particles, which are prepared in such a way that each one ideally has an initial (classical) velocity \mathbf{v} moving towards a slit-setup containing at least one aperture. The latter is assumed to be formed with unsharp edges to avoid diffraction effects to good approximation. This slit-setup will be passed by one particle at a time, as usual in quantum mechanical experiments, thereby generating a probabilistic distribution of particle locations in the course of time which is the subject of our investigation. Therefore, our model describes the evolution of said locations from right after the slit towards a screen (or even beyond) which allows us to develop and explain the mechanisms of the particle’s motion.

At this point we want, however, to point out the difference to Bohmian theory (see, e.g., Bohm and Hiley [BH93], Holland [Hol93], or Sanz and Miret-Artéz [SM12; SM14]), which also describes the above-mentioned particle path between a slit and a screen: The subject of our model is the description of the influence of an assumed sub-quantum medium on the velocities along the averaged trajectories and the probability currents³

¹The term ballistic diffusion will be defined in chapter 2.5 by Eq. (2.25).

²Although the fluid droplet model includes both, a bouncer and a walker, we consider it a single system due to the tight coupling. We prefer to point out the walker facet of the duality as this aspect suits better to ones understanding of the propagating particle.

³On the definition of probability currents see chapter 3.2.

in the domain between the slit(s) and the screen. In the mean of a vast number of particles our description converges to Bohm's one. As will be shown in this chapter, we do not provide a single particle's path as the outcome of a single experiment because the underlying (sub-quantum) environment is of statistical nature, similar to a classical Brownian motion. Accordingly, our model does not predict single-particle trajectories, instead, the Bohm-type motion emerges from our model as smoothed out motions of a vast number of single-particle's statistical hence erratic motions.

Even if we let the particles emerge one at a time only, the local probability density P right after the slit is assumed to be a Gaussian one. This comes along with a heat distribution generated by the oscillating particle, with a maximum at the centre of the aperture x_0 . To keep things simple, we describe the Gaussian decay as a function of its

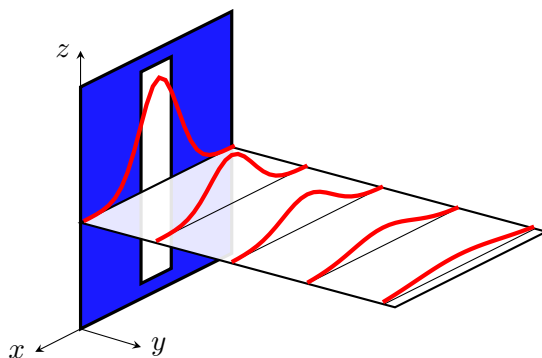


Figure 2.1.: Setting of a single-slit experiment in three dimensions with sketched spreading on an exemplary layer

distance y straight ahead from the slit (cf. Fig. 2.1). Even more, we connect the y -axis with time t by a constant velocity,

$$y(t) = \frac{\hbar k_y t}{m} = v_y t \tag{2.1}$$

with wave-vector k_y in y -direction and mass m . The idea behind this constant velocity v_y is that the incident sub-quantum wave before the slit-setup can be considered a plane wave which is cut by the slits into smaller parts continuing their propagation with the same, hence constant, velocity v_y . Any tentative propagation of the Gaussian shape orthogonal to said straight motion, i.e. a side motion into x -direction, will be compensated by an Ehrenfest motion later on by replacing $x_0 \rightarrow x_0 + v_x t$, i.e. an additive motion of the Gaussian centre along the x -axis (cf. Fig. 2.5).

According to the chosen setup, the Gaussian shape broadens only along the x -axis. There is no spreading along the direction of its propagation because of the assumed

steady heat flow from the particle's origin which is usually an oven in a fixed position far from the slit-setup in the negative y -direction. Further, there is also no spreading in the z -direction which is also the extent of the slit. A thus assumed spreading of a Gaussian in a plane along the z -direction is compensated by the spreading of a neighbored plane, as sketched out in Fig. 2.2, settled directly above or below of the current one, respectively, because of equal conditions in neighbouring plane. For simplicity, we neglect the impact of the slit's edges and assume for our inquest a sufficiently large distance from the upper and lower borders, too.

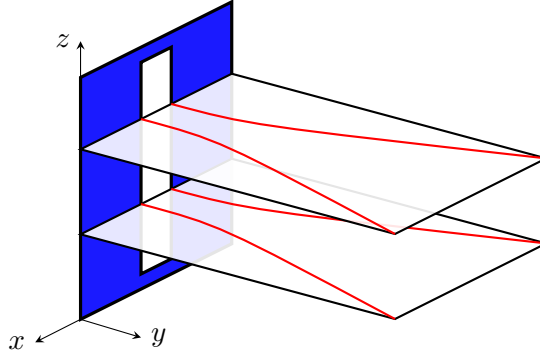


Figure 2.2.: Setting of a single-slit experiment in three dimensions with Bohm-type trajectories sketched on different layers

All problems treated in this thesis contain a Gaussian intensity dispersion appearing right behind the slit. The dispersion is assumed to be an ideal Gaussian function not being refracted at the slit's edges. Furthermore, the Gaussian extends along the whole x -direction, i.e. the Gaussian function is not cut by the slit it runs through, as indicated in Fig. 2.1 by the left most shape not cut by the slit. Thus one does not need to consider phase-free spaces along any light-cone-like structures which would arise otherwise.

In our model, the sub-quantum medium is the mediator between the vacuum energy and the particle itself. When said sub-quantum medium is excited, i.e. heated up by the oven, it builds immediately a landscape in the oven's surrounding which includes the setup comprising the slit(s) and the screen. In terms of an effective theory, the particle, once sent out by the oven, propagates on average along these trajectories which are already embedded in said landscape. "On average" means that the particle's propagation is most likely as described, but in a statistical sense. However, as discussed before, the path of a unique particle may be completely different.

In other words, when handling the particles' propagations, we make use of the probabilistic view in that we cannot describe the trajectory of a single particle but instead have a probability density $P(x, t)$ to find the particle within the interval $[x, x + dx]$ at

time t . Even though, quantum mechanics is already a tool to find solutions of probability density $P(x, t)$ for given setups, i.e. in the example before, the outcome $P(x, t)$ of the measurement at a screen being at a distance from a slit where the particles passed through, it lacks a deeper level explanation of this outcome.

2.3. Orthogonality relations and fluctuations

In chapter 1 we have distinguished two velocities: The osmotic velocity \mathbf{u} (1.59) and the diffusive velocity \mathbf{v} (1.58). They have already been provided in textbooks, e.g., Holland [Hol93], however, herein we will sketch the concise path provided by Grössing [Grö04]. Therefore, within the scope of this single chapter, we extend the coordinate x to its three-dimensional equivalent, \mathbf{x} , in order to describe orthogonality relations correctly.

We demand a Gaussian-shaped probability density $P(\mathbf{x}, t)$ to obey particular requirements, namely the normalization (B.1) such that the integration over the whole domain \mathbf{x} yields 1,

$$\int_{t=\text{const.}} P(\mathbf{x}, t) d^3x = 1, \quad (2.2)$$

and the continuity equation

$$\frac{\partial P(\mathbf{x}, t)}{\partial t} = -\nabla \cdot (\mathbf{v}P(\mathbf{x}, t)) \quad (2.3)$$

with the velocity $\mathbf{v}(\mathbf{x}, t)$ along the trajectory derived from a classical action function $S(\mathbf{x}, t)$ by

$$\mathbf{v}(\mathbf{x}, t) = \frac{\mathbf{p}}{m} = \frac{\nabla S(\mathbf{x}, t)}{m}. \quad (2.4)$$

From the assumed uniqueness and differentiability of $S(\mathbf{x}, t)$ follows that the paths don't cross each other. These paths correspond to particle trajectories orthogonal to surfaces (wave fronts) with constant action function $S(\mathbf{x}, t)$, as sketched in Fig. 2.3.

The example of Fig. 2.3 is but a particular one. In accordance with Huygens' principle, another wide-spread example is given by spherical wave surfaces. Here, the surface is initially concentrated at a point and then expands in a series of closed surfaces, such that the motion can be compared to that of a shock wave emanating from a "disturbing" point of a surface, i.e., as a travelling wave front (Fig. 2.4).

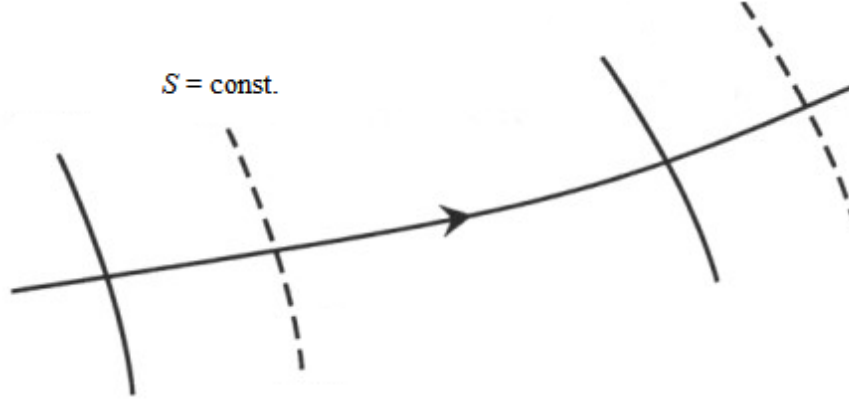


Figure 2.3.: Surfaces of constant action function $S(\mathbf{x}, t)$ representing wave fronts, with orthogonal particle trajectory. Courtesy Gerhard Grössing [Grö04]

To emphasise the orthogonality between a particle trajectory and a wave front, we, firstly, restrict ourselves to considering the stationary state of constant flow only, such that the l.h.s. of Eq. (2.3) is equal to zero. Then dividing by P we get

$$\nabla \cdot \mathbf{v} = -\frac{\nabla P}{P} \cdot \mathbf{v}. \quad (2.5)$$

In general, however, Eq. (2.5) is an expression for the non-conservation of momentum $\mathbf{p} = m\mathbf{v}$.

Secondly, we observe that the classical, so-called Hamiltonian flow (i.e. of incompressible fluids) given by

$$\nabla \cdot \mathbf{v} = 0$$

is only obtained if the r.h.s. of Eq. (2.5) vanishes, too, i.e.

$$\frac{\nabla P}{P} \cdot \mathbf{v} = 0. \quad (2.6)$$

Thus, unless trivially $\nabla P = 0$, the Hamiltonian flow can also be characterized by two orthogonal vectors, the vector $\mathbf{v} = \nabla S/m$ as of Eq. (2.4), $\mathbf{u} = \nabla(\delta S)/m$ as of Eq. (1.59) and the vector

$$\frac{\nabla P}{P} =: \text{const} \cdot \mathbf{u} = \text{const} \cdot \frac{\nabla(\delta S)}{m}, \quad (2.7)$$

which can also be set as proportional to a velocity \mathbf{u} . In fact, the totality of all vectors $\mathbf{u} = \nabla(\delta S)/m$ orthogonal to \mathbf{v} represents the velocity field of the spherical wave fronts

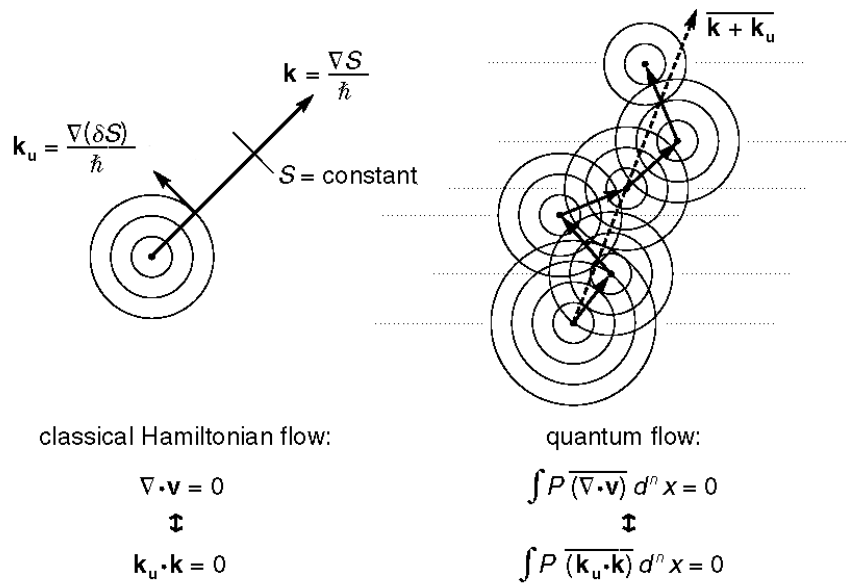


Figure 2.4.: Schematic distinction of classical Hamiltonian flow (left) and quantum flow (right). The dotted lines in the figure on the right indicate symbolically that the waves pictured represent only the local surroundings of a generally extending probability field, thus illustrating that the fluctuations shown are to be seen in the context of the whole embedding environment. Courtesy Gerhard Grössing [Grö04]

which can be considered to permanently emanate from the particle as Huygens waves. Using as a result from Grössing [Grö04] that

$$\frac{\Delta Q}{kT} = \frac{2\omega\delta S}{\hbar\omega}, \quad (2.8)$$

where we used relations (1.52) and (1.61) which fulfil the requirement of equal kinetic energies⁴ as discussed in chapter 1, we obtain the relation between the momentum variation $\delta\mathbf{p}$ (1.59) and the probability distribution P as

$$\delta\mathbf{p}(\mathbf{x}, t) = m\mathbf{u}(\mathbf{x}, t) =: \hbar\mathbf{k}_u(\mathbf{x}, t) = \nabla(\delta S(\mathbf{x}, t)) = -\frac{\hbar}{2} \frac{\nabla P(\mathbf{x}, t)}{P(\mathbf{x}, t)}, \quad (2.9)$$

where \mathbf{k}_u denotes the wave vector associated to the osmotic velocity \mathbf{u} .⁵ Combining with Eq. (1.59) and using Eq. (B.15) we find for the osmotic velocity

$$\mathbf{u}(\mathbf{x}, t) = -\frac{\hbar}{2m} \frac{\nabla P(\mathbf{x}, t)}{P(\mathbf{x}, t)} = -\frac{\hbar}{2m} \nabla \ln P(\mathbf{x}, t). \quad (2.10)$$

By setting Eqs. (2.5) and (2.7) we found an orthogonality condition for the velocities \mathbf{v} and \mathbf{u} which, however, is valid for a classical Hamiltonian flow. Considering additional fluctuations as discussed by the bouncer–walker model, we shall demand less stringent requirements, namely the vanishing of Eq. (2.5) *on average*,⁶

$$\overline{\nabla \cdot \mathbf{v}} = -\frac{\overline{\nabla P}}{P} \cdot \mathbf{v} = 0, \quad (2.11)$$

as shown in Fig. 2.4. The essential difference is given by a vanishing divergence of the velocity of the probability current, $\nabla \cdot \mathbf{v} = 0$, in the Hamiltonian flow, whereas in the quantum flow the average over fluctuations and positions of the average divergence be identical to zero (Eq. (2.11)).

The consequences on the averaging process as provided in $\overline{\mathbf{u}\mathbf{v}} = 0$ (2.11) are explicated by Grössing [Grö04] and later on by our group [Grö10b] in much deeper detail. In the latter, we also derived quantum mechanical dispersion as a consequence of this averaging process.

⁴Let us here repeat the note in context with Eq. (1.33): Although we are probably at a length scale where the thermodynamical laws have not yet proven valid, we use Eq. (1.52) as the sub-quantum analogon to the thermodynamical expression $k_B T/2$. However, as for today we neither know T nor the constant k – unless it should turn out as identical to k_B .

⁵The r.h.s. of Eq. (2.9) is readily confirmed by insertion of the r.h.s. of Eq. (2.8) into (2.9).

⁶The mean value $\overline{(\cdot)}$ can be understood either as an average over space or an average over an ensemble at a fixed position, $\overline{a(x)} = \int_{-\infty}^{\infty} aP(x, t) dx$. For a stationary process the mean value is constant because of $P(x, t) = P(t)$ (see e.g. [BY07; Sch06]).

2.4. From classical phase-space distributions to quantum mechanical dispersion

In accordance with the classical model, we shall now relate it more directly to the walker-bouncer analogy gleaned from Couder and Fort [CF12]. For, as shown, e.g., in Holland [Hol93] or Elze [Elz11], one can construct various forms of classical analogies to quantum mechanical Gaussian dispersion. The two mechanisms may refer to an early idea of de Broglie [dBro60] to model quantum behaviour by a two-fold process, i.e. by the movement of a hypothetical point-like singularity solution of the Schrödinger equation, and by the evolution of the usual wave function that would provide the empirically confirmed statistical predictions. Recently, Couder and Fort [CF12] have used this ansatz to describe the behaviour of their bouncer droplets: On an individual level, one observes particles surrounded by circular waves they emit through the phase-coupling with an oscillating bath, which provides, on a statistical level, the emergent outcome in close analogy to quantum mechanical behaviour like, e.g., diffraction or double-slit interference. [Mes13]

In the context of the double solution idea, which is related to correlations on a statistical level between individual uncorrelated particle positions x and momenta p , respectively, we consider the free Liouville equation for the probability distribution function $f(x, p, t)$ in phase-space of a mechanical system

$$\frac{\partial f}{\partial t} + \sum_{i=1}^3 \frac{p_i}{m} \frac{\partial f}{\partial x_i} - \sum_{i=1}^3 \frac{\partial V}{\partial x_i} \frac{\partial f}{\partial p_i} = 0 \quad (2.12)$$

with potential V and mass m . Here, we return to the one-dimensional description which is sufficient for further investigations. Liouville's equation (2.12) implies the continuity equation in phase-space and has the property that precise knowledge of initial conditions is not lost in the course of time. That is, it provides a phase-space distribution $f(x, p, t)$ that shows the emergence of correlations between x and p from an initially uncorrelated product function of non-spreading (classical) Gaussian position distributions as well as momentum distributions,

$$f_0(x, p) = \frac{1}{2\pi\sigma_0\pi_0} e^{-x^2/2\sigma_0^2} e^{-p^2/2\pi_0^2}, \quad (2.13)$$

where $\sigma_0 = \sigma(t = 0)$, and $\pi_0 := mu_0$ are the half-widths in space and momentum, respectively. The general solution of the free Liouville equation (2.12) for the case where the particles in the ensemble all have an initial velocity p/m at vanishing potential, $V = 0$, is

$$f(x, p, t) = f_0(x - pt/m, p), \quad (2.14)$$

inserting Eq. (2.13) reads

$$f(x, p, t) = \frac{1}{2\pi\sigma_0 m u_0} e^{-(x-pt/m)^2/2\sigma_0^2} e^{-p^2/2m^2 u_0^2}. \quad (2.15)$$

The probability density in x -space is given by

$$P(x, t) := \int f dp = \frac{1}{\sqrt{2\pi} \sigma(t)} e^{-x^2/2\sigma^2(t)}. \quad (2.16)$$

whereby the integration has been carried out by completing the square of p in Eq. (2.15). As a result, we find the variance at time t given by

$$\sigma^2(t) = \sigma_0^2 + u_0^2 t^2. \quad (2.17)$$

By superposition of the constant-width Gaussians with a moving centre we obtain the spreading Gaussian distribution with variance (2.17) which obviously reflects the fact that faster particles move further in a given time interval.⁷

The stochastic process described by the Langevin equation (1.24) involves momentum fluctuations $\delta p = m u$, now described by the momentum distribution in Eq. (2.13). Therefore, in u_0 as defined in Eq. (1.28) we have a connection to our walker model. This means that u_0 is related to the sub-quantum medium and hence to the particle's mass m revealed by the definition of the walker in Eq. (1.24). The half-width σ_0 is in turn tightly related to the slit-width as will be discussed later in chapter 5.5. Nonetheless, the half-widths σ_0 and π_0 of the distribution (2.13) are uncorrelated. On the other hand, according to the usual picture for dispersion (2.17) there actually is an initial spread of velocities $u_0 = \pi_0/m$. According to the minimal uncertainty principle⁸ the scale of the fluctuations of σ_0 and π_0 is given by \hbar via

$$\Delta x \Delta p = \sigma_0 \pi_0 = \frac{\hbar}{2}. \quad (2.18)$$

Using $\pi_0 = m u_0$, the diffusion constant (1.66), $D = \hbar/2m$, and Eq. (2.18) yields

$$u_0 = \frac{D}{\sigma_0}. \quad (2.19)$$

⁷We shall use the fact that the Gaussian shape remains a Gaussian in chapter 2.6 by replacing $x \rightarrow x - v_x t$, $v_x = \text{const.}$

⁸See also Bohm and Hiley [BH93, p. 46] who point out the fact that eventually the width of the packet corresponds to the spread of distances covered by the particles which is in turn determined by the spread of velocities which is equal to Δv ; velocity v being well-defined in the causal interpretation.

This leads, by substituting Eq. (2.19) into (2.17), to

$$\sigma^2(t) = \sigma_0^2 \left(1 + \frac{D^2 t^2}{\sigma_0^4} \right) \quad (2.20)$$

which explicitly contains σ_0 as an expression for the given slit which determines σ_0 . The properties of the particle are yet given by the constant $D = \hbar/2m$.

2.5. Derivation of the time-dependent diffusion equation

In section 2.4, the probability density $P(x, t)$ is modelled Gaussian shaped. For this class of functions we can now investigate a generalized diffusion equation with a time-dependent diffusion coefficient (cf. [Mes12; Mes13]). Therefore, we make an ansatz for a more general relationship of diffusion equations,

$$\frac{\partial P}{\partial t} = kt^\alpha \frac{\partial^2 P}{\partial x^2}, \quad (2.21)$$

with factor alpha, $0 \leq \alpha \leq 2$, determining the type of diffusion, e.g., $\alpha = 0$ reduces (2.21) to the usual heat equation (cf. [Bol10]). Factors t and k denote the time and a constant factor, respectively. We ask for possible values of k and α .

Inserting $P(x, t)$ of Eq. (2.16) as a known solution into Eq. (2.21) yields

$$\frac{P\dot{\sigma}}{\sigma} \left(\frac{x^2}{\sigma^2} - 1 \right) = kt^\alpha \frac{P}{\sigma^2} \left(\frac{x^2}{\sigma^2} - 1 \right), \quad (2.22)$$

and by integrating the simplified equation (2.22), $\dot{\sigma}\sigma = kt^\alpha$, we find

$$\sigma^2 = 2k \frac{t^{\alpha+1}}{\alpha+1} + c_0. \quad (2.23)$$

A comparison of Eq. (2.20) and (2.23) yields $c_0 = \sigma_0^2$, $\alpha = 1$, and

$$k = \frac{D^2}{\sigma_0^2}. \quad (2.24)$$

Finally, inserting this result into Eq. (2.21) leads to

$$\frac{\partial P}{\partial t} = \underbrace{\frac{D^2 t}{\sigma_0^2}}_{D_t} \frac{\partial^2 P}{\partial x^2}, \quad (2.25)$$

where one immediately recognizes the time-dependent diffusion coefficient

$$D_t(t) = \frac{D^2}{\sigma_0^2} t = u_0^2 t = \frac{\hbar^2}{4m^2\sigma_0^2} t, \quad (2.26)$$

which, because of its linearity of time t , gives Eq. (2.25) the name *ballistic diffusion equation*. This condition is only fulfilled by $\alpha = 1$, which is the only possible diffusion equation whose solution has the form (2.16).

If the diffusion depends on space, one has to deal with a diffusion coefficient $D_t(x, t)$, and thus

$$\frac{\partial P}{\partial t} = \frac{\partial}{\partial x} \left(D_t(x, t) \frac{\partial P}{\partial x} \right). \quad (2.27)$$

However, this is not in the scope of this thesis, though the handling of space-dependent diffusion equations can be found in, e.g., the textbook of John C. Strikwerda [Str04].

2.6. Spreading of the wave packet

Now we generalize the discussion of chapter 2.4 as mentioned in the footnote on page 27 and add the displacement⁹ $x - vt$ to the Gaussian distributions of Eqs. (2.15) and (2.16). The easiest way to follow the decay in the evolution of time is to observe a point with distance $\xi(t)$ from the centre of the Gaussian shape (see Fig. 2.5) defined by

$$\xi(t) = \xi(0) \frac{\sigma(t)}{\sigma_0} \quad (2.28)$$

with

$$\frac{\sigma(t)}{\sigma_0} = \sqrt{1 + \frac{D^2 t^2}{\sigma_0^4}} \quad (2.29)$$

being the dispersion (2.20) of the wave packet. Due to definition (2.28) the probability

$$\int_{vt}^{vt+\xi(t)} P(x, t) dx \quad (2.30)$$

is time-independent.

In Fig. 2.5 the spreading according to Eq. (2.28) is sketched.

⁹The particle moves with velocity $v_y = \text{const.}$ which is not relevant to this one-dimensional examination. The optional additive, constant motion along the x -axis is depicted by v for short. Accordingly, $v = v_x = \text{const.}$, otherwise noted.

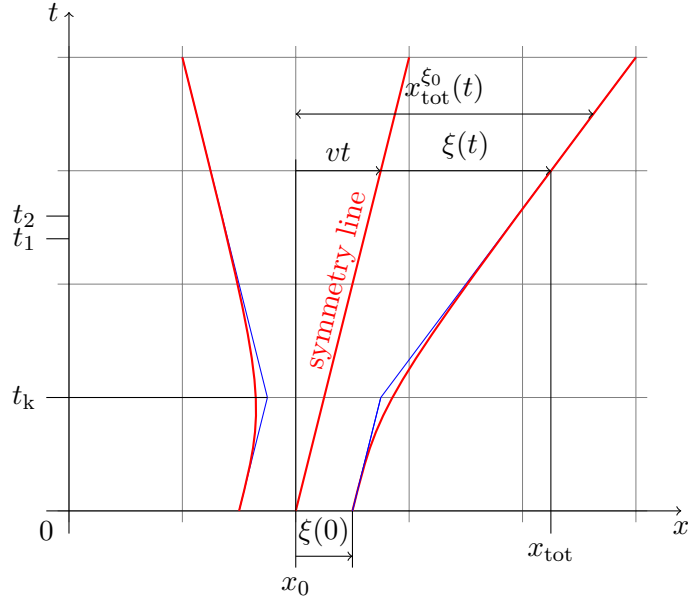


Figure 2.5.: Bohm-type trajectories for a quantum particle with initial Gaussian distribution exhibiting the characteristics of ballistic diffusion

The functional relationship (2.30) is clearly valid for the particular point $\xi(0) = \sigma_0$ which, substituted into (2.28), leads immediately to $\xi(t) = \sigma(t)$, and hence the evidence that this particular point follows the variance of the decaying Gaussian. However, the relation $\xi(t) \propto \sigma(t)$ is, for all starting points $\xi(0)$, always true as the Gaussian remains a Gaussian but broadens during decay for all $t > 0$, which is reflected in Eq. (2.30).

As the packet spreads according to Eq. (2.29), $\xi(t)$ describes the result of the average motion along a trajectory of a point of this packet that was initially at $\xi(0)$. Depending on the initial value of $|\xi(0)|$, i.e. the distance from x_0 of the initial centre point of the packet, said spreading happens faster or slower. In our model picture, this is easy to understand: For a trajectory exactly at the centre of the packet, $x_{\text{tot}}(t) = x_0 + vt \Leftrightarrow \xi(0) = 0$, the momentum contributions from the heated up environment on average cancel each other for symmetry reasons. However, the further off a trajectory is from that centre, the stronger this symmetry will be broken, i.e. leading to a position-dependent net acceleration or deceleration, respectively, or, in effect, to the decay of the wave packet. The actual decay of the wave packet starts, roughly spoken, at a time t_k , indicated by a kink in Fig. 2.5 which is due to the squared time-behaviour in Eq. (2.29). By dividing the trajectories at t_k into two time domains, one can see its behaviour for $t \ll t_k$, where $\xi(t) \propto \xi(0) = \text{const.}$, and $t \gg t_k$, where $\xi(t) \propto t$ – and hence ballistic: The propagations described by $\xi(t)$ are linear in both domains just kicked off to either side from the

symmetry line (see Fig. 2.5).

From Fig. 2.5 we find $x_{\text{tot}}(t) = x_0 + vt + \xi(t)$. Without loss of generality we set $x_0 = 0$ further on. With the use of Eq. (2.28) we obtain

$$x_{\text{tot}}^{\xi_0}(t) = vt + \xi(t) = vt + \xi(0) \frac{\sigma(t)}{\sigma_0} = vt + \xi(0) \sqrt{1 + \frac{u_0^2 t^2}{\sigma_0^2}}. \quad (2.31)$$

In our model picture, $x_{\text{tot}}^{\xi_0}$ maps time t to the position of the *smoothed out trajectories*, i.e. those averaged over a very large number of Brownian motions.

Moreover, one can now also calculate the *average total velocity field of a Gaussian wave packet* as

$$v_{\text{tot}}^{\xi_0}(t) = \frac{dx_{\text{tot}}^{\xi_0}(t)}{dt} = v + \xi(0) \frac{u_0^2 t / \sigma_0^2}{\sqrt{1 + u_0^2 t^2 / \sigma_0^2}}, \quad (2.32)$$

which describes the velocity $v_{\text{tot}}^{\xi_0}$ of a point along a trajectory at time t .

Finally, we derive the *average total acceleration field of a Gaussian wave packet* is

$$a_{\text{tot}}^{\xi_0}(t) = \frac{dv_{\text{tot}}^{\xi_0}(t)}{dt} = \xi(0) \frac{u_0^2 / \sigma_0^2}{\sqrt{(1 + u_0^2 t^2 / \sigma_0^2)^3}}, \quad (2.33)$$

describing the acceleration of a point along the trajectory at time t . Eqs. (2.31) to (2.33) allow us to calculate the quantities along a trajectory only out of a given starting point, indicated by $\xi(0)$.

Actually we are interested in the dynamics at any given position (x, t) directly. Using

$$\xi(t) = x - vt \quad (2.34)$$

and Eq. (2.28) we rewrite

$$\xi(0) = \frac{x - vt}{\sqrt{1 + u_0^2 t^2 / \sigma_0^2}} \quad (2.35)$$

which leads to the generalized fields,

$$x_{\text{tot}}(x, t) = x, \quad (2.36)$$

$$v_{\text{tot}}(x, t) = v + \xi(t) \frac{u_0^2 t / \sigma_0^2}{1 + u_0^2 t^2 / \sigma_0^2} = v + (x - vt) \frac{u_0^2 t}{\sigma^2(t)}, \quad (2.37)$$

$$a_{\text{tot}}(x, t) = \xi(t) \frac{u_0^2 / \sigma_0^2}{(1 + u_0^2 t^2 / \sigma_0^2)^2} = (x - vt) \frac{u_0^2 \sigma_0^2}{\sigma^4(t)}, \quad (2.38)$$

which will be used in the simulations.

Eqs. (2.31) to (2.38) provide the trajectory distributions and the velocity field of a Gaussian wave packet as derived solely from classical physics. The trajectories here only represent the averaged behaviour of a statistical ensemble, i.e. averaged over many single trajectories of ballistic diffusion assuming Eq. (2.18), i.e. a relation between the initial spatial and momentum distributions. The results are in full accordance with quantum theory, and in particular with Bohmian trajectories (see, for example, Holland [Hol93] or Sanz [SM08], or the figures for the Gaussian wave packet example of von Bloh [vBlo10], which are in excellent agreement with our Fig. 2.6). This is so despite the fact that neither a quantum mechanical wave function, nor the Schrödinger equation, nor a guiding wave equation, nor a quantum potential has been used yet.

Fig. 2.6 provides a graphic representation of Eq. (2.31) for an exemplary set of trajectories. Considering the particles of a source as oscillating bouncers, they can be shown to heat up their – generally nonlocal – environment in such a way that the particles leaving the source are guided through the thus created thermal landscape. In the Fig. 2.6, the classically simulated evolution of exemplary *averaged* trajectories is shown.

The figures show results of simulations with coupled map lattices (cf. section 5.2.1) of classical diffusion and a time-dependent diffusivity as given by Eq. (2.26). Two examples are shown, with different half-widths of the initial Gaussian distribution, respectively: space-time diagrams, providing the intensity field with time development from bottom to top and averaged trajectories in agreement with Eq. (2.31). In Fig. 2.6(a), the initial σ_0 is half the value in Fig. 2.6(b). Note that the narrower the Gaussian distribution is concentrated initially around the central position, the more the thus stored heat energy tends to push trajectories apart.

2.7. Conclusions and perspectives

As a follow-up of chapter 1, the constituting single-slit setup has been introduced in this chapter. A distant oven has been supposed to be the particle source for the later experiment. Before a particle ever drops out of the oven and would be taken into account, a continuously emitted energy wave, borne by the sub-quantum medium, has been assumed to be produced by the oven. The wave itself, when reaching the setup, has been approximated by a plane wave being cut-out and sliced when passing the slit. Immediately after the slit, the remaining, cut wave has been assumed taking shape of a Gaussian.

Two velocities, the osmotic velocity \mathbf{u} and the diffusive velocity \mathbf{v} , have been assumed to be orthogonal on average. This kind of orthogonality – not valid for a single event

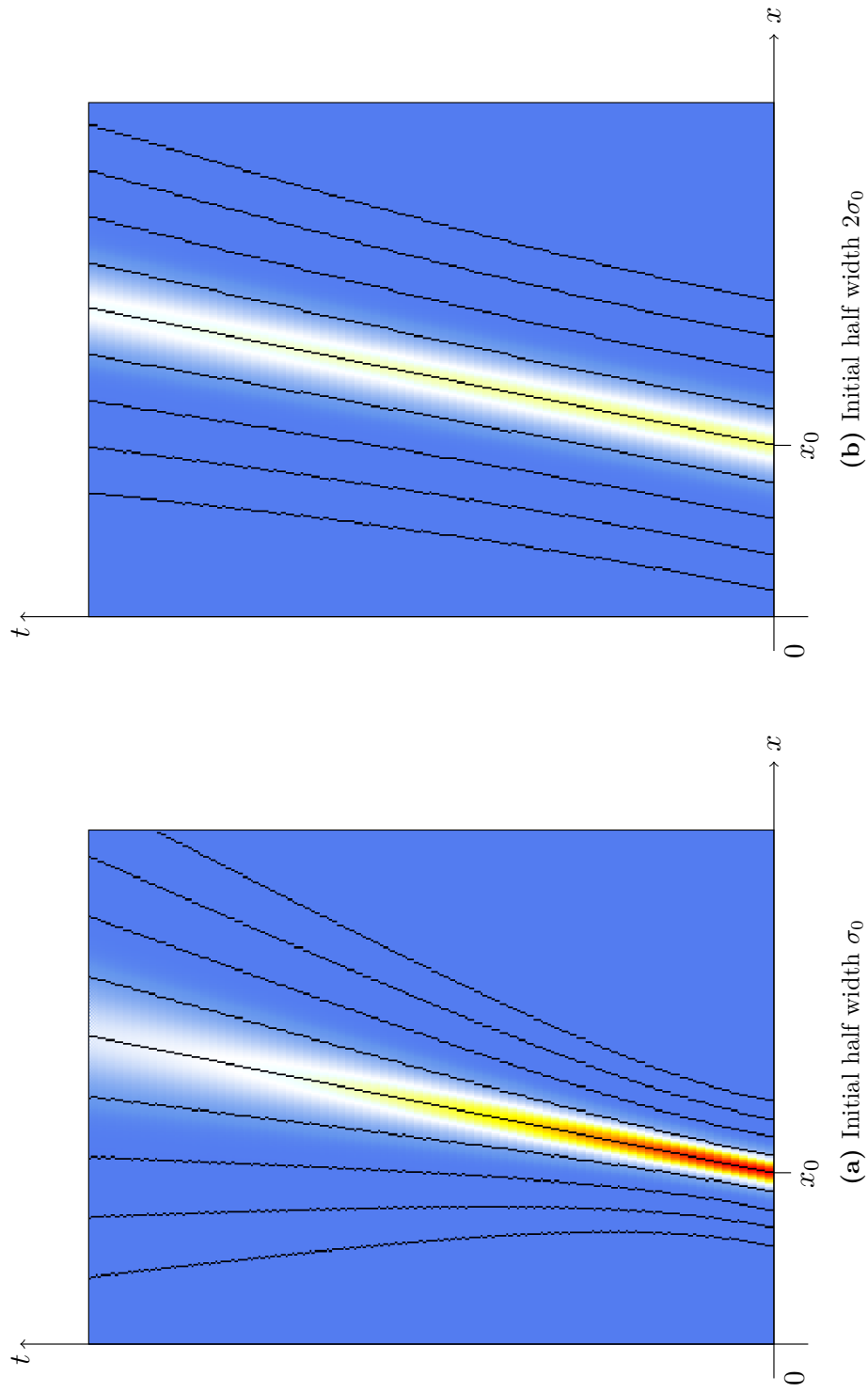


Figure 2.6.: Dispersion of a free Gaussian wave packet with trajectories representing the averaged behaviour of a statistical ensemble for two different initial spreadings

but for a vast number of events – has also been stated to be the main difference to the Bohmian philosophy. As on average our results converge to the Bohmian ones, the characteristic of our ansatz may be called a phenomenological one.

From classical phase-space distribution comprising non-spreading Gaussian position and momentum distributions, the quantum mechanical dispersion has been derived. This then has led to the time-dependent diffusion equation, or more precisely, the ballistic diffusion equation. With these tools available, the spreading of a wave packet could be established, founded on the ballistic diffusion equation only, which in turn allowed for quickly performed simulations of said spreading fields.

Yet no phase relations have been required because the setup has comprised of a single slit only. Consequently, the next step shall be expanding the setup by at least one further slit and studying the then importantly needed phase relations.

3. Current-based theory on interference effects

In this chapter we investigate the phase relations due to adding one further slit and eventually an arbitrary number of slits. By considering both the classical and the emergent distributions' relations as well as the orthogonality relations between the convective and osmotic currents discussed in chapter 2, we shall derive a set of current-based rules providing calculation recipes for both, the total intensity P_{tot} and the total current \mathbf{J}_{tot} in a systematic way.

As an application of these current-based rules, we shall provide simulation results of double-slit setups and discuss the sub-quantum behaviour according to our phenomenological approach.

In a final step, we shall extend the current-based rules to multi-slit scenarios and discuss the Talbot effect by means of simulations based on these rules.

3.1. Interference and emergence at a Gaussian double-slit

In Fig. 3.1 the underlying geometry for the wave vectors in a double-slit setup is sketched, both for the classical interference and the emergent¹ case (cf. [Fus14; Grö16b]). For illustration, we show the three-dimensional setup with two exemplary planes emphasised. The upper one contains a sketch of the classical picture according to wave optics, the lower one contains a simulated resulting image and trajectories to illustrate the emergent picture. The incident wave² is indicated by parallel wave vectors \mathbf{k} of a plane wave in

¹Emergence is a process whereby larger entities arise through interactions among smaller or simpler entities such that the larger entities exhibit properties the smaller/simpler entities do not exhibit (cf. [Wik16]). The interference pattern in Fig. 3.1 is considered to be emergent in this sense.

²To get a picture of what it is that is oscillating, we stress the walker-bouncer picture again and consider the wave to comprise the oscillating sub-quantum medium having the properties known from wave optics.

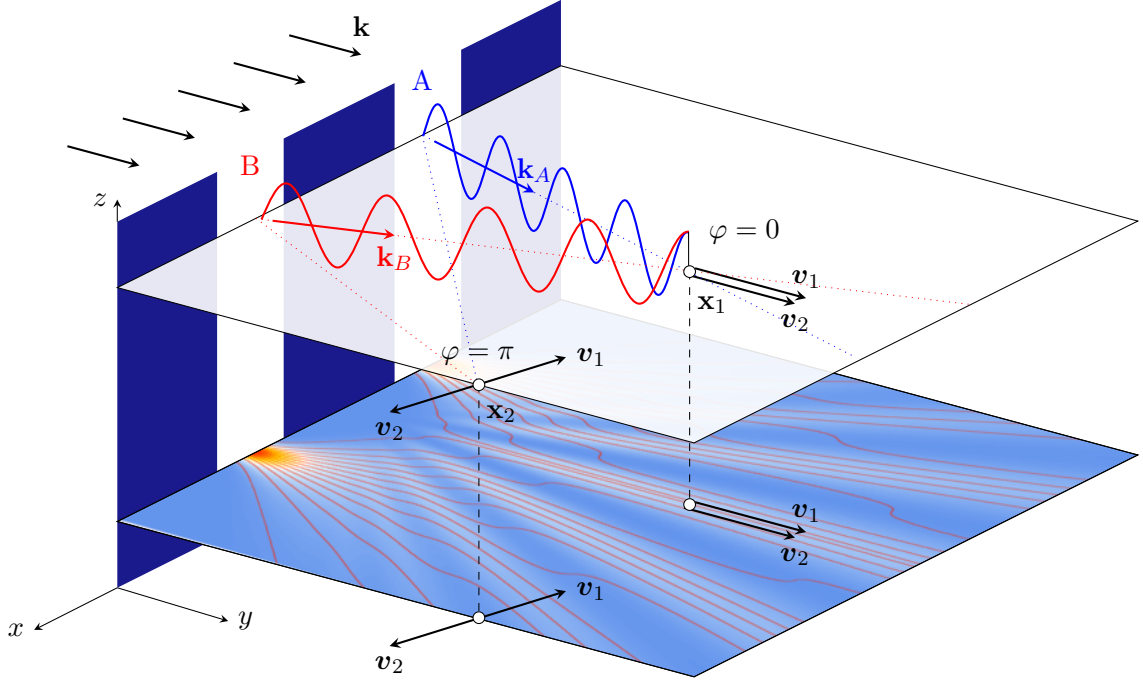


Figure 3.1.: Geometry of interference at a double-slit at exemplary points \mathbf{x}_1 and \mathbf{x}_2

the xz -plane propagating in y -direction as is used in our simplified model to keep things clearly arranged. All vectors are assumed to be located in the xy -plain, i.e. they are independent of z , whereby $y \propto t$ as defined by Eq. (2.1).

Let us start with the upper plain. In the classical picture the incoming wave vector

$$\mathbf{k} = \frac{2\pi}{\lambda} \hat{\mathbf{k}}, \quad (3.1)$$

with $\hat{\mathbf{k}} = \mathbf{k}/|\mathbf{k}|$ being the unit vector and λ the wavelength, splits up at the Gaussian slits³ A and B into \mathbf{k}_A and \mathbf{k}_B , both are orthogonal to the particular propagating wave fronts. As the slits A and B act like coherent sources the resulting interference pattern is time-independent. The respective phases for each of the beams are usually denoted as⁴

$$\varphi_{A(B)} = \mathbf{k}_{A(B)} \cdot \mathbf{r}_{A(B)}, \quad (3.2)$$

³The distribution after the slit is assumed to be an ideal Gaussian not being refracted at the slit's edges as explained in chapter 2.2.

⁴We use this notation for short, with $A(B)$ meaning that either the left character is to be used for the whole equation, or the character inside the parentheses. However, they must not be mixed up, i.e. $\varphi_{A(B)} = \mathbf{k}_{A(B)} \cdot \mathbf{r}_{A(B)}$ means $\varphi_A = \mathbf{k}_A \cdot \mathbf{r}_A$ and $\varphi_B = \mathbf{k}_B \cdot \mathbf{r}_B$, but $\varphi_A \neq \mathbf{k}_B \cdot \mathbf{r}_A$ etc.

with $\mathbf{r}_{A(B)}$ being a position vector from source $A(B)$ to point \mathbf{x} , marked as dotted lines in Fig. 3.1.

With Eq. (3.2) together with plane wave amplitudes at an arbitrary point \mathbf{x} of the spatio-temporal plane we aim at describing relations known from Bohmian theory like Eqs. (3.21) and (3.22). The amplitudes

$$R_{A(B)}(\mathbf{x}) = \sqrt{P_{A(B)}^S(\mathbf{x})}, \quad (3.3)$$

with $P^S(\mathbf{x})$ being an intensity distribution function of a single slit as defined in Eq. (2.16), allow for describing the beams coming from slits A and B as

$$\tilde{R}(\mathbf{x}, t) = R(\mathbf{x}) \operatorname{Re} \left\{ e^{i(\mathbf{k} \cdot \mathbf{r} - \omega t)} \right\} = R(\mathbf{x}) \cos(\mathbf{k} \cdot \mathbf{r} - \omega t) \quad (3.4)$$

wherein describing $R(\mathbf{x})$ thereby omitting the frequency ω is sufficient. Combining the beams of, say, two slits by simply adding the two components leads to

$$R(\mathbf{x}) = R_A(\mathbf{x}) \cos \varphi_A + R_B(\mathbf{x}) \cos \varphi_B. \quad (3.5)$$

Even though Eq. (3.5) is a usual method to describe the distribution correctly, we want to introduce in this chapter the results from the last chapters instead, namely the ballistic diffusion and the associated velocities derived for the single slit system.

Therefore, we turn towards the lower plane, the “emergent” scenario. We have to treat the two slits, or respective beam paths, as the sources of a flow of probability densities which we want to express by the involved wave vectors, or equivalently⁵, by the involved velocities. For this picture, we have in the foregoing chapters already introduced the (emergent) convective velocity $\mathbf{v}_i(x)$ and the (emergent) osmotic velocity $\mathbf{u}_i(\mathbf{x})$, both of which have its source originated in the slits A and B . However, the impacting velocities shall be denoted with numbers 1 and 2, instead of the letters A and B , respectively, in order to distinguish them from the classical picture. The osmotic velocities have to fulfil the condition of being unbiased w.r.t. the convective velocities, i.e. the orthogonality relation (2.11) for the *averaged* velocities, $\overline{\mathbf{v}\mathbf{u}} = 0$, since any fluctuations $\mathbf{u} = \nabla(\delta S)/m$ are shifts along the surfaces of action $S = \text{const.}$, as shown in Fig. 2.3.

Each point of the probability (or amplitude) landscape evolves on the spatial plane according to the convective velocities $\mathbf{v}_i(\mathbf{x})$, $i = 1, 2$ (exemplarily shown at \mathbf{x}_1 and \mathbf{x}_2 in Fig. 3.1). In addition, the osmotic velocity $\mathbf{u}(\mathbf{x})$ describes the dispersion 2.20 of the Gaussian and split up into $\mathbf{u}_1(\mathbf{x})$ and $\mathbf{u}_2(\mathbf{x})$ dependent of the slit which causes the respective osmotic velocity (Fig. 3.2). Since \mathbf{u}_i are orthogonal to \mathbf{v}_i , $\langle \mathbf{v}_i, \mathbf{u}_i \rangle = \frac{\pi}{2}$, all

⁵For the relation between wave vectors and velocities is about equation $\mathbf{p} = m\mathbf{v} = \hbar\mathbf{k}$ and the quantities used therein. See Eqs. (2.1) and (2.9).

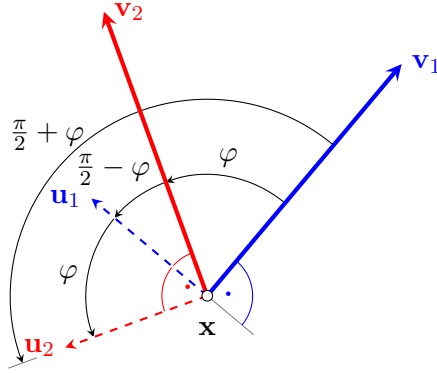


Figure 3.2.: Geometry of emergent velocities and relative phases for a two-beam setup.

enclosed angles can be expressed in terms of $\varphi = \sphericalangle(\mathbf{v}_1, \mathbf{v}_2)$. As can be seen in Fig. 3.2 we get

$$\begin{aligned}\sphericalangle(\mathbf{v}_1, \mathbf{u}_2) &= \frac{\pi}{2} + \varphi, \\ \sphericalangle(\mathbf{v}_2, \mathbf{u}_1) &= \frac{\pi}{2} - \varphi.\end{aligned}\tag{3.6}$$

3.2. A set of current rules

In the following⁶ we shall show how the trajectories representing the paths of the averaged velocities can be calculated with the help of a set of current rules leading to the expressions for the total current \mathbf{J}_{tot} and the total probability density P_{tot} at point \mathbf{x} .

As we have to deal with two velocities caused by the same slit, we introduce the term *channel* here, i.e. we have two channels per slit. To account for the different velocity channels $i = 1, \dots, 2N$, N being the number of slits, we now introduce for general cases generalized velocity vectors \mathbf{w}_i , with

$$\begin{aligned}\mathbf{w}_1 &:= \mathbf{v}_1, & \mathbf{w}_2 &:= \mathbf{u}_1, \\ \mathbf{w}_3 &:= \mathbf{v}_2, & \mathbf{w}_4 &:= \mathbf{u}_2,\end{aligned}\tag{3.7}$$

for the first (upper line) and second (lower line) channel in the case of $N = 2$. This renumbering procedure will turn out as an important practical bookkeeping tool.

For the weighting procedure to be introduced next, each amplitude R_i according to Eq. (3.3) is assumed to have its corresponding P_i^S of the interference-free single-slit, as

⁶We will omit the variable \mathbf{x} in the argument of any vector, amplitude, probability density, and probability current to improve readability.

if none of the probability distributions has interfered with any other hitherto. For the bookkeeping we apply the same nomenclature as before, i.e.

$$\begin{aligned} R_{\mathbf{w}_1} &= R_{\mathbf{w}_2} = R_1, \\ R_{\mathbf{w}_3} &= R_{\mathbf{w}_4} = R_2, \end{aligned} \tag{3.8}$$

again, for the case of $N = 2$. It should be noted that any $R_{\mathbf{w}_i}$ is the amplitude of the sub-quantum medium at point \mathbf{x} moving with velocity \mathbf{w}_i .

Now, we apply the usual definition of a probability current, which reads

$$\mathbf{J}_{\mathbf{w}_i} = \mathbf{w}_i P_{\mathbf{w}_i}, \quad i = 1, \dots, 4, \tag{3.9}$$

wherein the index runs from $1, \dots, 2N$ with N being the numbers of slits. Here the number of slits is $N = 2$. The general velocity vectors \mathbf{w}_i are defined in Eq. (3.7), such that a probability current $\mathbf{J}_{\mathbf{w}_i}$ at point \mathbf{x} is caused by the sub-quantum medium moving with velocity \mathbf{w}_i at that point. The total probability current is the sum over all partial currents (3.9) which reads

$$\mathbf{J}_{\text{tot}} = \sum_{i=1}^4 \mathbf{J}_{\mathbf{w}_i} = \sum_{i=1}^4 \mathbf{w}_i P_{\mathbf{w}_i}. \tag{3.10}$$

The local intensity of a partial current is dependent on all other currents, thus the total current composes of all partial components. This mutual dependence of a current's totality and its parts constitutes the essential part that leads to a convenient set of current rules. [Grö14c; JS12a; JS12b; Wal00; WG16] Notable, this concept uses the peculiarity of using currents as *basic* ingredient and not as derivation of some elementary entity like, e.g., an elementary particle.

However, in Eqs. (3.9) and (3.10) we shall define $P_{\mathbf{w}_i}$ different from the previously used P_i^S in that we want to incorporate interference processes between the channels. To account for that, we assume the probability density to be caused by \mathbf{w}_i under the influence of \mathbf{w}_j . We stick herein to the theory proposed by Fussy [Fus14] but adapt his procedure⁷ to a rather straightforward scheme that works as follows: The influencing, convective currents \mathbf{v}_1 and \mathbf{v}_2 determine the causing currents \mathbf{w}_i in such a way that only their projection

$$\cos \varphi_{i,j} := \hat{\mathbf{w}}_i \cdot \hat{\mathbf{w}}_j \tag{3.11}$$

⁷In Fussy [Fus14] the procedure works by splitting up the velocities \mathbf{u}_i in two parts, right and left, \mathbf{u}_{iR} and \mathbf{u}_{iL} , respectively, and hence associated unit vectors $\hat{\mathbf{u}}_{iR}$ and $\hat{\mathbf{u}}_{iL}$ that cancel each other during the projection. This is equivalent to the procedure shown herein, however, the argumentation is different.

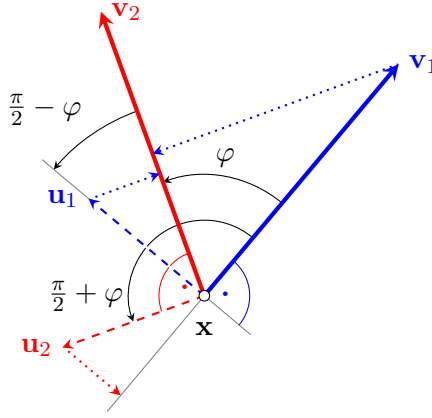


Figure 3.3.: Scheme for the construction of the the projections.

takes effect. The principle of the projection scheme is sketched in Fig. 3.3. Furthermore, the causing and influencing amplitudes, $R_{\mathbf{w}_i}$ and $R_{\mathbf{w}_j}$, respectively, both contribute to the resulting probability density. In this spirit, we define

$$P_{\mathbf{w}_i} = R_{\mathbf{w}_i} \hat{\mathbf{w}}_i \cdot (\hat{\mathbf{v}}_1 R_1 + \hat{\mathbf{v}}_2 R_2) \quad (3.12)$$

and the total intensity as

$$\begin{aligned} P_{\text{tot}} &= \sum_{i=1}^4 P_{\mathbf{w}_i} = \sum_{i=1}^4 \hat{\mathbf{w}}_i R_{\mathbf{w}_i} \cdot (\hat{\mathbf{v}}_1 R_1 + \hat{\mathbf{v}}_2 R_2) \\ &= (\hat{\mathbf{v}}_1 R_1 + \hat{\mathbf{v}}_2 R_2)^2 = P_{\mathbf{v}_1} + P_{\mathbf{v}_2} \end{aligned} \quad (3.13)$$

and obtain

$$P_{\text{tot}} = R_1^2 + R_2^2 + 2R_1 R_2 \cos \varphi. \quad (3.14)$$

From $\mathbf{J} = \mathbf{w}P$ we get the *emergent total velocity*

$$\mathbf{v}_{\text{tot}} = \frac{\mathbf{J}_{\text{tot}}}{P_{\text{tot}}} = \frac{\sum_{i=1}^4 \mathbf{w}_i P_{\mathbf{w}_i}}{\sum_{i=1}^4 P_{\mathbf{w}_i}}. \quad (3.15)$$

Thus we obtain amplitude contributions of the total system's wave field projected on each channel's amplitude at point \mathbf{x} via $P_{\mathbf{w}_i}$. Then, the usual symmetry, even in the classical interference case above, between $P_{\mathbf{w}_i}$ and $R_{\mathbf{w}_i}$ is broken:

$$P_{\mathbf{w}_i} \neq R_{\mathbf{w}_i}^2, \quad (3.16)$$

i.e. although each velocity component \mathbf{w}_i has an associated amplitude $R_{\mathbf{w}_i}$, the *partial* term $P_{\mathbf{w}_i}$ is not the mere squared amplitude any more. That is why $P_{\mathbf{w}_i}$ should rather be referred to as *relational intensity* since the intensities $P_{\mathbf{w}_i}$ of Eq. (3.12) may assume negative values which works well for contributions to the overall probability density P_{tot} (3.13) but lacks an interpretation as a probability itself.

Returning now to our previous notation of the four velocity components, \mathbf{v}_i and \mathbf{u}_i , $i = 1, 2$, the partial current associated with \mathbf{v}_1 is generated by constructing the scalar product of $\hat{\mathbf{v}}_1$ with all other unit vector components which reads (see Fig.3.3)

$$\mathbf{J}_{\mathbf{v}_1} = \mathbf{v}_1 P_{\mathbf{v}_1} = \mathbf{v}_1 R_1 \hat{\mathbf{v}}_1 \cdot (\hat{\mathbf{v}}_1 R_1 + \hat{\mathbf{v}}_2 R_2) = \mathbf{v}_1 (R_1^2 + R_1 R_2 \cos \varphi) \quad (3.17)$$

and analogously

$$\mathbf{J}_{\mathbf{v}_2} = \mathbf{v}_2 P_{\mathbf{v}_2} = \mathbf{v}_2 (R_2^2 + R_1 R_2 \cos \varphi). \quad (3.18)$$

The same applied to currents \mathbf{u}_i leads to (see Fig.3.3)

$$\begin{aligned} \mathbf{J}_{\mathbf{u}_1} &= \mathbf{u}_1 P_{\mathbf{u}_1} = \mathbf{u}_1 R_1 \hat{\mathbf{u}}_1 \cdot (\hat{\mathbf{v}}_1 R_1 + \hat{\mathbf{v}}_2 R_2) \\ &= \mathbf{u}_1 R_1 R_2 \cos \left(\frac{\pi}{2} - \varphi \right) = \mathbf{u}_1 R_1 R_2 \sin \varphi \end{aligned} \quad (3.19)$$

and

$$\begin{aligned} \mathbf{J}_{\mathbf{u}_2} &= \mathbf{u}_2 P_{\mathbf{u}_2} = \mathbf{u}_2 R_2 \hat{\mathbf{u}}_2 \cdot (\hat{\mathbf{v}}_1 R_1 + \hat{\mathbf{v}}_2 R_2) \\ &= \mathbf{u}_2 R_1 R_2 \cos \left(\frac{\pi}{2} + \varphi \right) = -\mathbf{u}_2 R_1 R_2 \sin \varphi \end{aligned} \quad (3.20)$$

with an asymmetry in the last line which is obvious from the geometry sketched in Fig. 3.2.

By summing up all current contributions according to Eq. (3.10) we obtain the final expression for the total density current built from the remaining $2N = 4$ velocity components

$$\mathbf{J}_{\text{tot}} = R_1^2 \mathbf{v}_1 + R_2^2 \mathbf{v}_2 + R_1 R_2 (\mathbf{v}_1 + \mathbf{v}_2) \cos \varphi + R_1 R_2 (\mathbf{u}_1 - \mathbf{u}_2) \sin \varphi. \quad (3.21)$$

The total velocity \mathbf{v}_{tot} according to Eq. (3.15) now reads as

$$\mathbf{v}_{\text{tot}} = \frac{R_1^2 \mathbf{v}_1 + R_2^2 \mathbf{v}_2 + R_1 R_2 (\mathbf{v}_1 + \mathbf{v}_2) \cos \varphi + R_1 R_2 (\mathbf{u}_1 - \mathbf{u}_2) \sin \varphi}{R_1^2 + R_2^2 + 2R_1 R_2 \cos \varphi}. \quad (3.22)$$

The obtained total probability current field \mathbf{J}_{tot} spanned by the various velocity components \mathbf{v}_i and \mathbf{u}_i we have denoted as the path excitation field (cf. chapter 2.6, and [Grö12b]). It is built by the sum of its partial currents, which themselves are built by an amplitude weighted projection of the total current. Furthermore, we observe that the superposition principle is violated for \mathbf{J} , and, analogously for P , in the following sense: In quantum mechanics the amplitudes of the wave function components have to be summed up coherently, i.e. superpositioned, in the case of undisturbed paths, and for calculation of the probability density this sum has to be taken as absolute value squared. In other words, the Schrödinger equation is linear, and observation of a state is regularized by Born's rule. In our case, all the relevant variables, i.e. $P_{\mathbf{w}_i}$ and $\mathbf{J}_{\mathbf{w}_i}$, are nonlinear. Consequently, to obtain the correct total probability density P_{tot} or total current \mathbf{J}_{tot} , respectively, one has to take into account *all* elementary, i.e. partial, contributions to the corresponding variable.

Summarizing, the shift to a new projection rule of Eq. (3.12) build the kernel for a set of relations of current rules. It is characterized by summing up the nonlinear partial currents, where each of the latter contains information about the total field via the projection rule. This property is characterized in that any change in a local field affects the total field, and *vice versa*.

The trajectories or streamlines, respectively, are obtained according to $\dot{\mathbf{x}} = \mathbf{v}_{\text{tot}}$ in the usual way by integration. By re-inserting the expressions for convective velocities from Eq. (2.4),

$$\mathbf{v}_i = \frac{\nabla S_i}{m}, \quad (3.23)$$

and diffusive velocities from Eq. (2.10) together with (B.22),

$$\mathbf{u}_i = -\frac{\hbar}{m} \frac{\nabla R_i}{R_i}, \quad (3.24)$$

one immediately identifies Eq. (3.22) with the Bohmian guiding equation and Eq. (3.21) with the quantum mechanical pendant for the probability current [BH93; SM08].

3.3. Double-slit interference

It is straightforward to now also describe and explain quantum interference with our approach (cf. [Grö12a; Grö12b; Grö13]). We choose a textbook scenario in the form of the calculation of the intensity distribution and the particle trajectories in an electron interferometer. As we are also interested in the trajectories, we refer to, and compare our results with, the well-known work by Philippidis *et al.* [Phi79], albeit in the form as presented by Holland [Hol93].

We choose similar initial situations as Holland, i.e. electrons, represented by plane waves in the forward y -direction, from a source passing through soft-edged slits 1 and 2 in a barrier, located along the x -axis, and recorded at a screen. In our model, we therefore note two Gaussians representing the totality of the effectively heated-up path excitation field, one for slit 1 and one for slit 2, whose centres have the distances $+X$ and $-X$ from the plane spanned by the source and the centre of the barrier along the y -axis, respectively.

The results according to Eq. (3.14) is shown in Fig. 3.4 which depicts the interference of two beams emerging from Gaussian slits⁸. The trajectories are the flux lines obtained by choosing a set of appropriate initial points at $y = 0$. The trajectories follow a no-crossing rule⁹: Particles from the left slit stay on the left side and *vice versa* for the right slit. This feature is explained here by a sub-quantum build-up of kinetic (heat) energy acting as an emergent repellent along the symmetry line.

In Fig. 3.4 one can observe a basic characteristic of the averaged particle trajectories, which, just because of the averaging, are identical with the Bohmian trajectories. To fully appreciate this surprising characteristic, we remind the reader of the severe criticism of Bohmian trajectories as put forward by Scully and others [Scu98, and references therein]. The critics claimed that Bohmian trajectories would have to be described as “surreal” ones because of their apparent violation of momentum conservation. In fact, due to the no-crossing rule for Bohmian trajectories in Young’s double-slit experiment, for example, the particles coming from, say, the right slit – and expected at the left part of the screen if momentum conservation should hold on the corresponding macro-level – actually arrive at the right part of the screen – and *vice versa* for the other slit. In Bohmian theory, this no-crossing rule is due to the action of the non-classical quantum potential, such that, once the existence of a quantum potential is accepted, no contradiction arises and the trajectories may be considered “real” instead of “surreal”.

Here we can note that in our sub-quantum approach an explanation of the no-crossing rule is even more straightforward and actually a consequence of a detailed *microscopic momentum conservation* as discussed in section 2.3 and in [Grö12b]. As can be seen in Fig. 3.4, the trajectories are repelled from the central symmetry line. However, in our case this is only implicitly due to a quantum potential, but actually due to the identification of the latter with a kinetic rather than a potential energy: As has already been stressed in [Grö09], it is the *heat of the compressed vacuum* that accumulates along

⁸For details on how the simulations have been carried out see chapter 5.3, on the construction of the trajectories see chapter 5.4. Initial values for all simulations are $P_1 = P_2$, $\sigma_1 = \sigma_2$, $v_{x,1} = v_{x,2} = 0$, otherwise noted.

⁹From the assumed uniqueness and differentiability of $S(\mathbf{x}, t)$ follows that the paths don’t cross each other. See section 2.3 for further explanations. However, at this stage we are discussing an ontological point of view on how the no-crossing phenomenon can be explained.

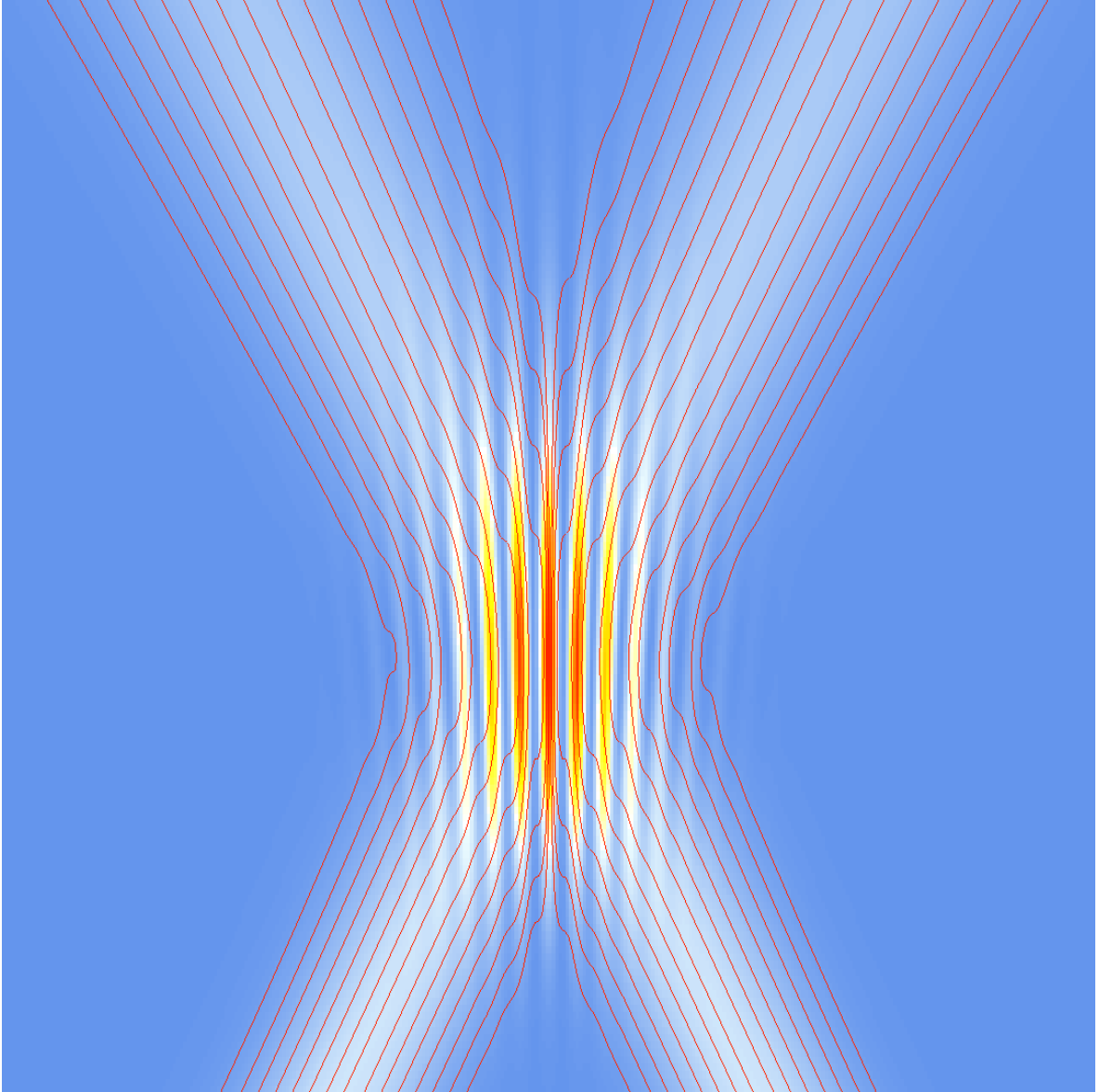


Figure 3.4.: Classical computer simulation of the interference pattern: Intensity distribution with increasing intensity from white through yellow and orange, with trajectories (red) for two Gaussian slits, and with small dispersion (evolution from bottom to top; $v_{x,1} = -v_{x,2}$).

said symmetry line, i.e. as reservoir of outward oriented kinetic energy, and therefore repels the trajectories. Fig. 3.4 is in full concordance with the Bohmian interpretation

(see, for example, [SM08] for comparison).

This can be shown even in greater detail. Whereas in the example of Fig. 3.4 the small amount of dispersion is practically negligible, we now discuss in more detail an interference scenario with significant dispersion of the two Gaussians, i.e. where initially the two Gaussians spread independently from each other due to the action of the diffusive velocities u_1 and u_2 , respectively.

In Fig. 3.5, trajectories according to Eq. (3.22) for the two Gaussian slits are shown. The interference hyperbolas for the maxima characterize the regions where the phase difference $\varphi = 2n\pi$, and those with the minima lie at $\varphi = (2n + 1)\pi$, $n = 0, \pm 1, \pm 2, \dots$. Note in particular the kinks of trajectories moving from the centre-oriented side of one relative maximum to cross over to join more central relative maxima. The trajectories are in full accordance with those obtained from the Bohmian approach, as can be seen by comparison with references [BH93; Hol93; SB09], for example. In our classical explanation of double-slit interference, a detailed micro-causal account of the corresponding kinematics can be given: Firstly, we note that the last term in Eq. (3.21), which is responsible for the genuinely quantum behaviour, is characterized by the vector $\mathbf{u}_1 - \mathbf{u}_2$ which in the interference region is always oriented into the forward direction away from the slits (Fig. 3.5). This means that said last term is modulated by $\sin \varphi$, with the result that the term alternates between forward directions where $\sin \varphi > 0$ and backward directions where $\sin \varphi < 0$.

Thus, in the backward cases, the trajectories coming from the relative maxima (bright fringes) loose velocity/momentum in the forward direction and cross over into the area of the relative minimum (dark fringes). Alternatively, in the forward cases, the trajectories coming from the relative minima (dark fringes) gain velocity/momentum in the forward direction and thus align with the other trajectories of the bright fringes. In other words, for the areas where $\sin \varphi < 0$, part of the current (along a relative maximum) is being removed (depletion), whereas for $\sin \varphi > 0$, parts of currents flow together to produce a newly formed bright fringe (accumulation). This is in accordance with an earlier description of quantum interference, where the effects of diffusion wave fields (cf. [Man00; Man01]) were explicitly described by alternating zones of heat accumulation or depletion, respectively [Grö09]. Towards the central symmetry line, then, one observes heat accumulation from both sides, and due to big momentum kicks from the central accumulation of heat energy, the forward particle velocities' directions align parallel to the symmetry axis. With the crossing-over of particle trajectories being governed by the last, diffusion-related, term on the right hand side of Eq. (3.21), one finds that for $\varphi = 0$ the resulting diffusive current is zero and thus, as total result of the overall kinematics, no-crossing is possible. Further, we note that our results are also in agreement with the experimental results by Kocsis *et al.* [Koc11].

Finally, to illustrate the straightforward applicability of our model to more general

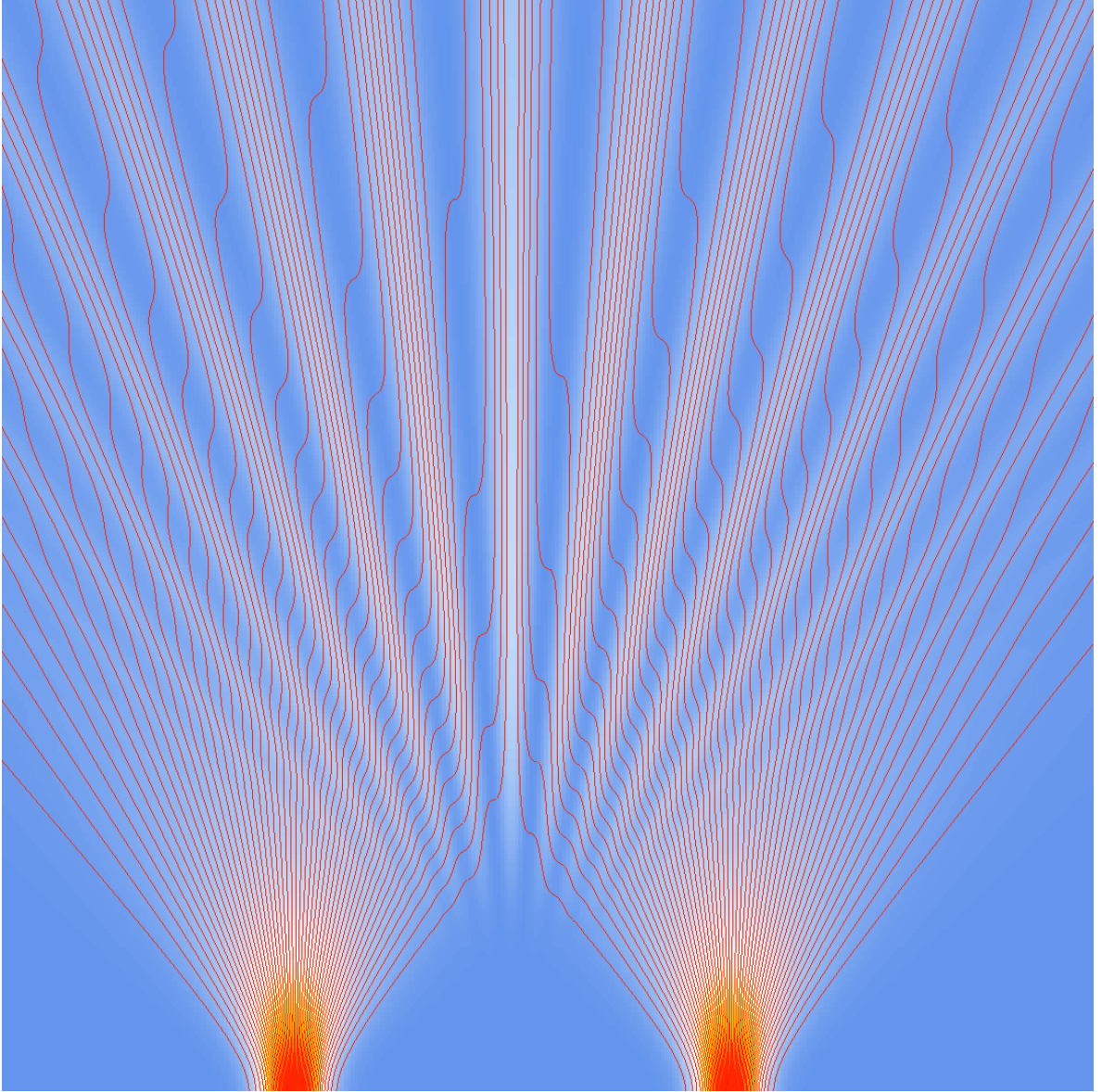


Figure 3.5.: Classical computer simulation of the interference pattern: Intensity distribution with increasing intensity from white through yellow and orange, with trajectories (red) for two Gaussian slits, and with large dispersion (evolution from bottom to top; $v_{x,1} = v_{x,2} = 0$)

situations, i.e. as compared to the simple symmetrical scenarios of Figs. 3.4 and 3.5, we now employ our simulation schema to cases where neither the Gaussians are identical

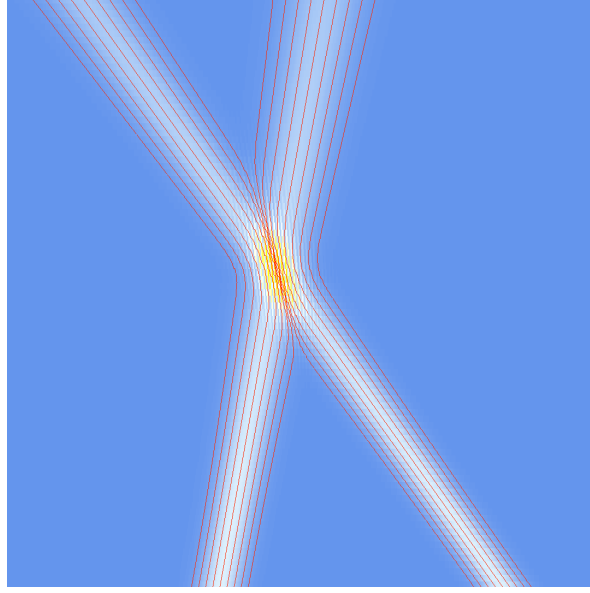


Figure 3.6.: Same as Fig. 3.4, but with different initial average velocities: $v_{x,2} = -4v_{x,1}$. Note again the no-crossing behaviour, with the two trajectory bundles repelling each other due to the kinetic (heat) energy along the slanted central line.

nor their weights. We thus study asymmetric coherent superpositions as discussed in ref. [SM08], and in our Figs. 3.6 to 3.8 we show results in accordance with the figures 4–6 of ref. [SM08]. The analysis of ref. [SM08] holds identically in our approach, so that we here restrict ourselves to pointing out that our figures display the following cases of varied properties for the beams emerging from the two slits:

- different modulus of the initial velocity/momentum,
- different initial spreading,
- different weights for the probability densities.

3.4. Entangling currents in the double-slit experiment

Because of the mixing of diffusion currents from both channels, we call the following decisive term in \mathbf{J}_{tot} (3.21) the *entangling current* [Grö12a; Grö13; Mes13]

$$\mathbf{J}_e = R_1 R_2 (\mathbf{u}_1 - \mathbf{u}_2) \sin \varphi = \frac{\hbar}{m} (R_1 \nabla R_2 - R_2 \nabla R_1) \sin \varphi \quad (3.25)$$

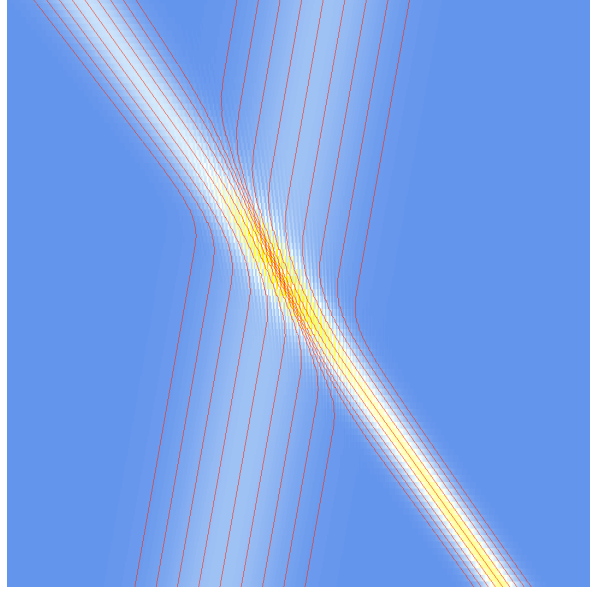


Figure 3.7.: Same as Fig. 3.6, but with different initial spreading: $\sigma_1 = 3\sigma_2$. Although the two partial beams altogether reflect off each other, one can clearly observe the effect of *microscopic momentum conservation*: The path excitation field of the right beam is propagated over to the micro-kinematics of the left beam, and *vice versa*.

where Eq. (3.24) has been substituted.

For illustration, Figs. 3.9–3.11 show our classical computer simulations of interference and the role of the entangling current \mathbf{J}_e in different situations. The entangling current \mathbf{J}_e (3.25) is characterized by the difference of the diffusive velocities \mathbf{u}_i , and is hence responsible for the nature of the process forming the interference pattern. Fig. 3.9 shows the emerging interference pattern and the average trajectories without, and Fig. 3.10 with an applied extra phase shift (according to Fig. 3.12(a)) at one slit. To bring out the shifting of the interference pattern more clearly, in Fig. 3.11 we apply – mainly for didactic reasons, as it is not clear what applying the phase to a slit in the distance means – the phase shift at much later times (according to Fig. 3.12(b)) than in Fig. 3.10. Thereby, also a decoupling of wave and particle behaviours becomes visible.

The distributions of P and \mathbf{J}_e in Fig. 3.11 are the same as in Fig. 3.9 for times $t < t_1$ and as in Fig. 3.10 for times $t > t_2$, respectively, and show the effect of the shifting of the interference fringes more clearly than Fig. 3.10. Note the radically different behaviours of the probability density related to wave-like interference on the one hand, and that of the average particle trajectories on the other hand. Although the currents \mathbf{J}_e dramatically cross the central symmetry line separating the areas of the two slits, the

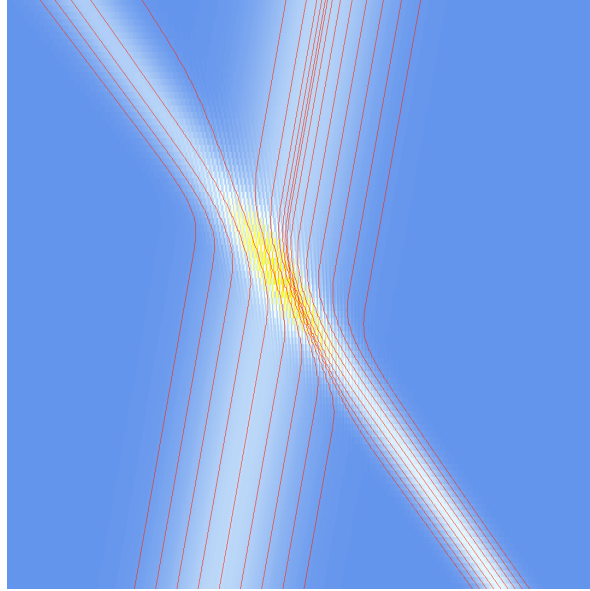


Figure 3.8.: Same as Fig. 3.7, but with different probability densities: $P_1 = 2P_2$. Note that the emerging beam behaviour compares more with inelastic scattering than with the elastic-type scattering of Fig. 3.7, as part of the left beam merges with the right one.

average particle trajectories (Fig. 3.11(a)) strictly obey the no-crossing rule familiar from, but not restricted to, the de Broglie–Bohm interpretation. This is a clear demonstration of the partial decoupling of wave and particle behaviour as envisaged in our model.

As a further example, we use a similar setup as in Fig. 3.4. The graphical result of a classical computer simulation of the interference pattern in a double-slit experiment, including the average trajectories, with evolution from bottom to top, is shown in Fig. 3.13(a). The Gaussian wave packets characterized by moderate spreading at the same standard deviations σ move towards each other with constant velocities $v_{x,1} = -v_{x,2}$. In Fig. 3.13(b), we use the same double-slit arrangement as in Fig. 3.13(a), but now include a phase shifter affecting slit 1, as sketched by the yellow rectangle on the left hand side. The exemplary choice of $\Delta\varphi = \pi$ results in a shift of the interference fringes. Comparing with Fig. 3.13(a), we recognize now a minimum of the resulting distribution along the central symmetry line.

Comparing Figs. 3.14(a) with 3.14(b), one notes that the dramatic shift from maxima to minima, and *vice versa*, as observed in the interference patterns of Fig. 3.13(a) and Fig. 3.13(b), respectively, is essentially caused by the changes in these entangling currents. This corresponds to a sub-quantum account of the processes underlying

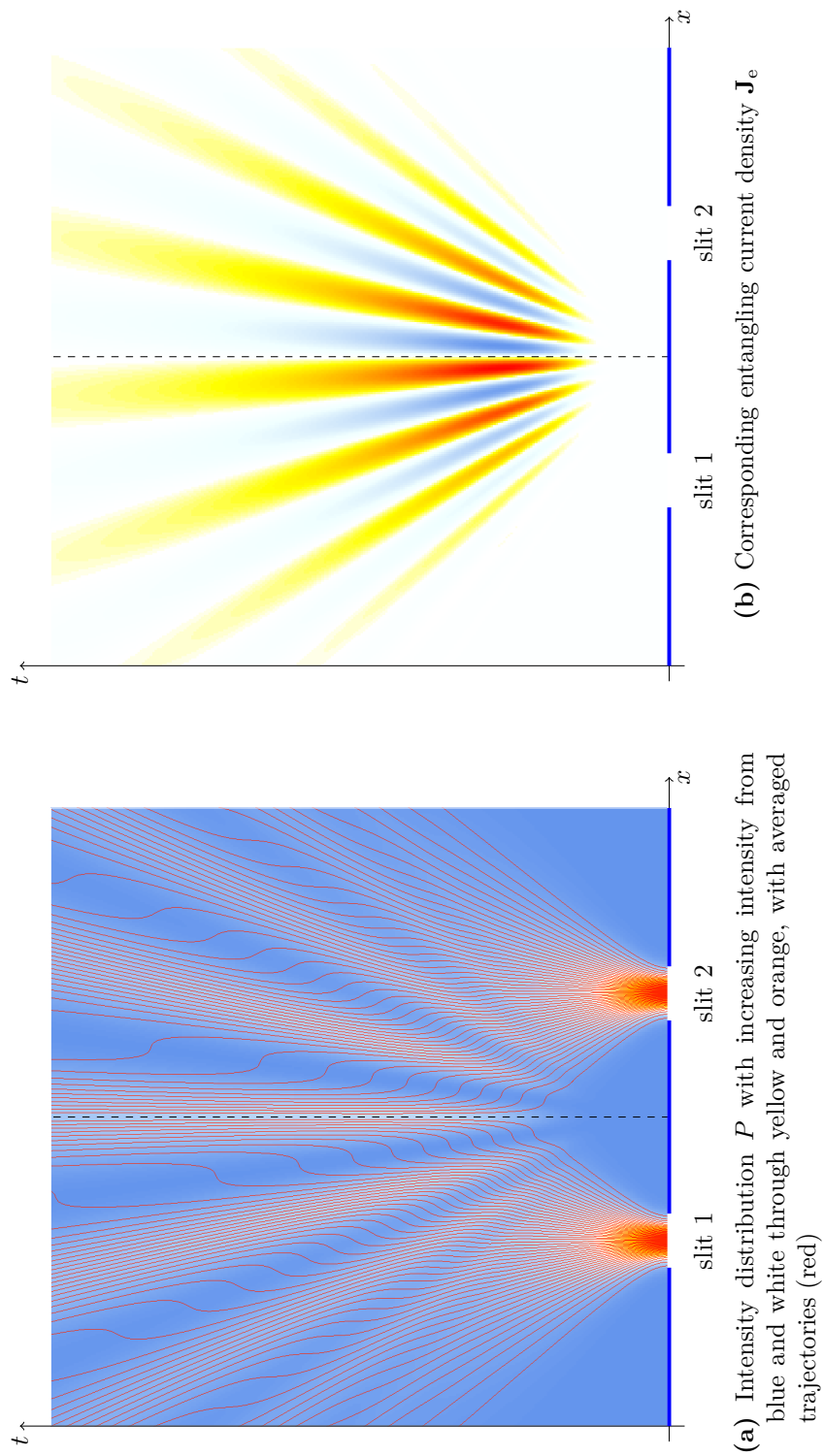


Figure 3.9.: Classical computer simulation of the interference pattern of the interference pattern with equal slit widths for two Gaussian slits ($v_{x,1} = v_{x,2} = 0$)

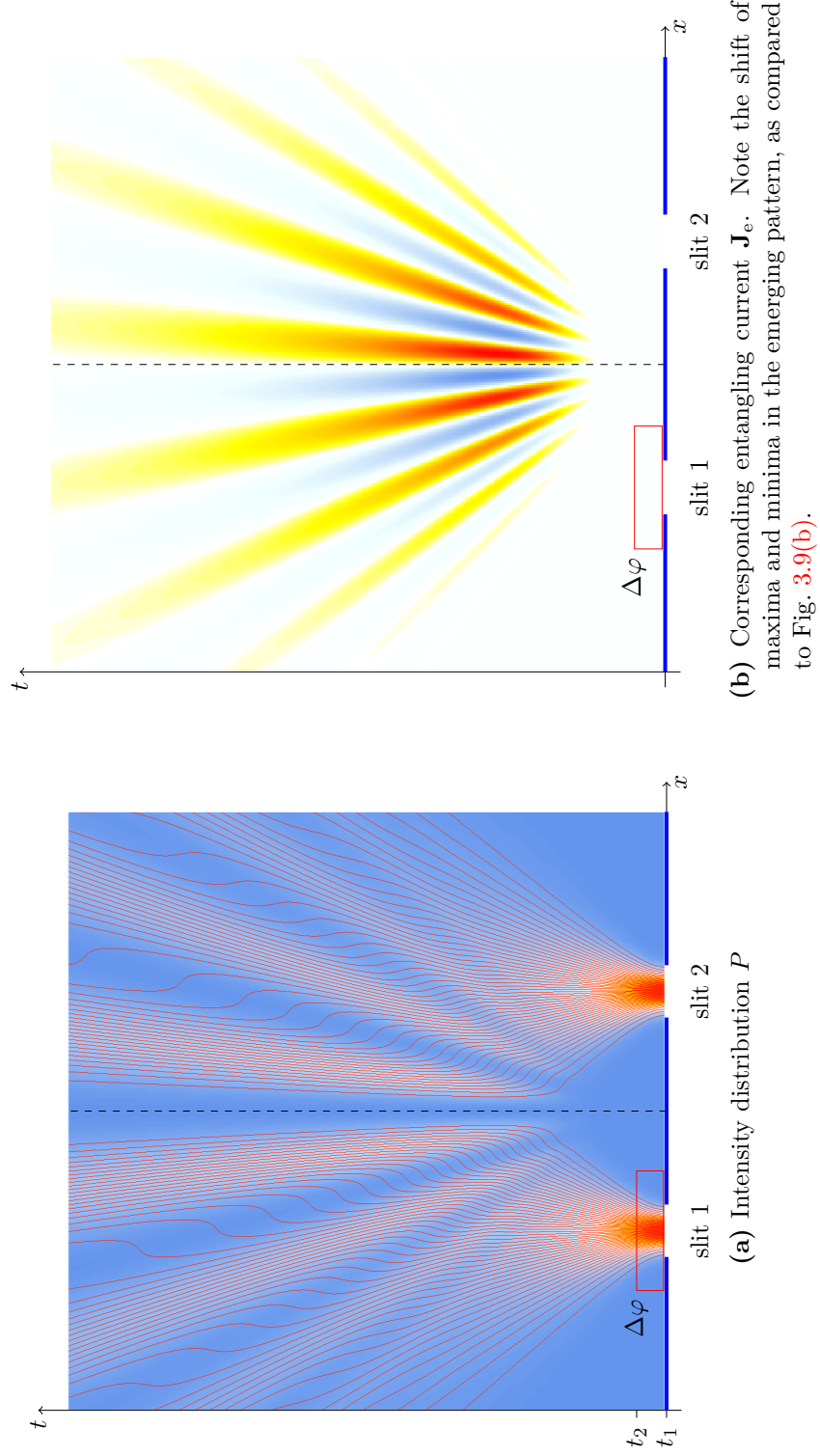


Figure 3.10.: Classical computer simulation as in Fig. 3.9, but with additional phase shift $\Delta\varphi = 3\pi$ gradually accumulated during the time interval between t_1 and t_2 at slit 1

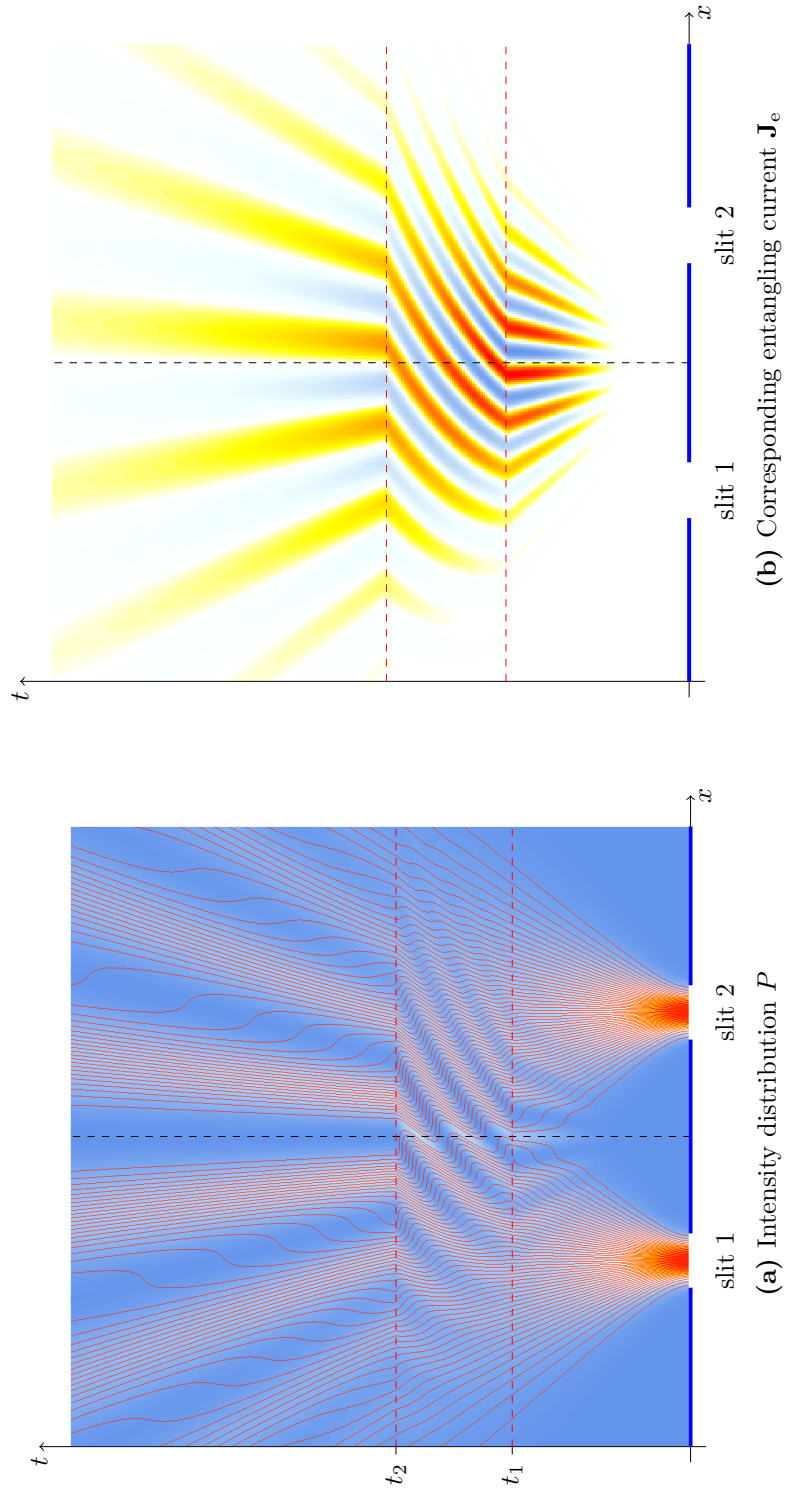


Figure 3.11.: Classical computer simulation as in Fig. 3.10, but with different times t_i and with gradually accumulated additional phase $\Delta\varphi = 5\pi$. Values for both, P and \mathbf{J}_e being equal to that of Fig. 3.9 for $t < t_1$ and Fig. 3.10 for $t > t_2$, respectively

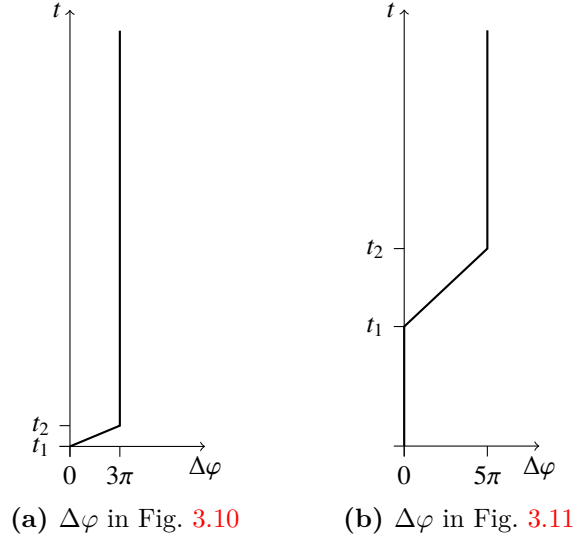


Figure 3.12.: Additional phase shift $\Delta\varphi$ accumulated during the time interval between t_1 and t_2 at slit 1. Different phase shifts of $\Delta\varphi = 3\pi$ and $\Delta\varphi = 5\pi$, respectively, lead to identical distributions of P and J_{tot} at last.

quantum interference.

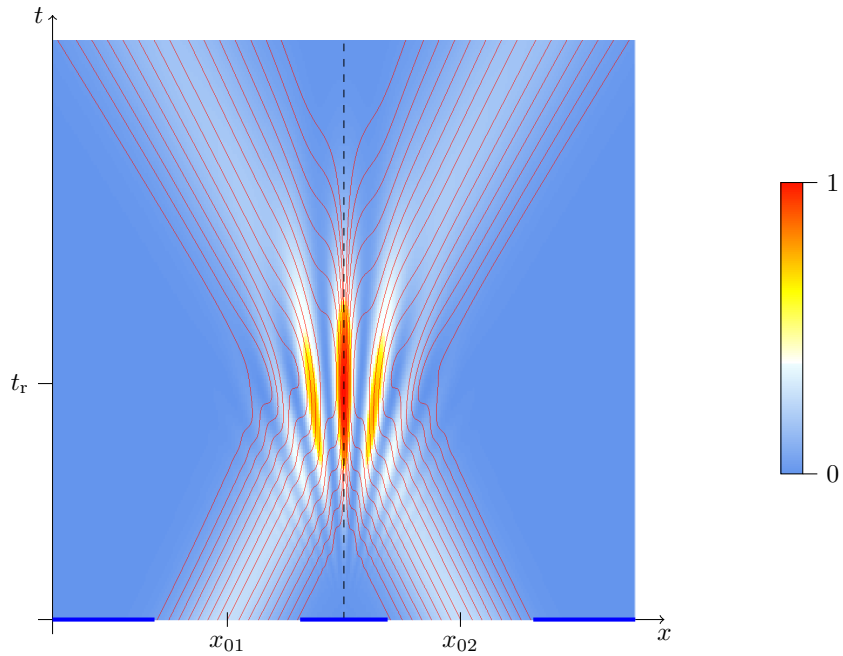
The result of our computer simulation of the probability current (3.21) is shown in Fig. 3.14 corresponding to the intensity distributions of Fig. 3.13. One recognizes the change of the maximum values of the probability current along the central symmetry line in Fig. 3.14(b) in comparison with those of Fig. 3.14(a). Since the figures display the one-dimensional case, the current flow is along the x -axis only. Interestingly, at the time t_r of the reversal of the trajectories, the current flow comes to a hold, and starts again for times $t > t_r$ with reversed signs. This can be understood as a reversal of the relative flow of heat $Q_2 - Q_1$ between the two channels, since we have from (1.63) that

$$\mathbf{u}_i = -\frac{1}{2\omega m} \nabla Q_i, \quad (3.26)$$

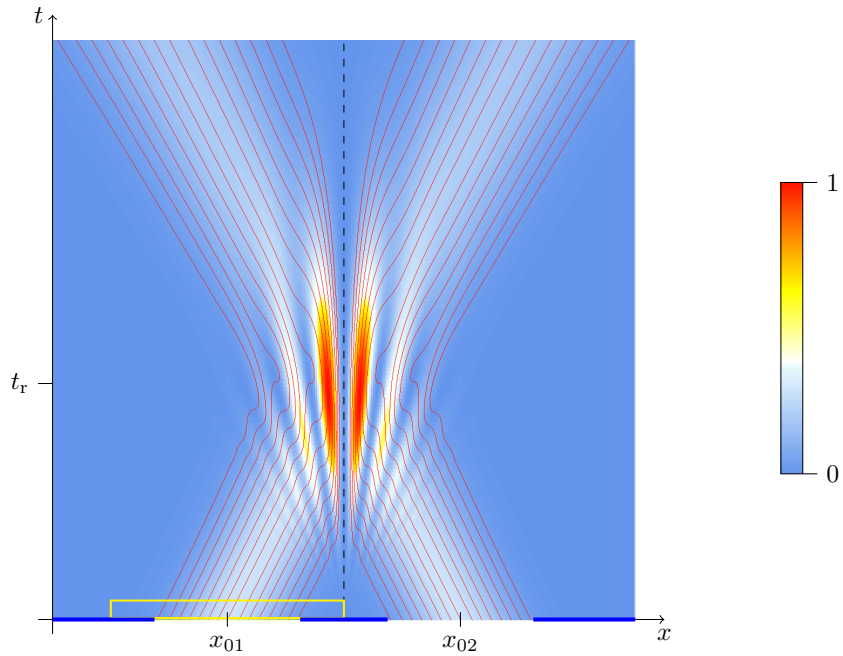
such that the last term of \mathbf{J}_e (3.25) reads as

$$\frac{1}{2\omega m} \sqrt{P_1 P_2} \nabla(Q_2 - Q_1) \sin \varphi_{12}. \quad (3.27)$$

The probability current \mathbf{J}_{tot} in both figures essentially only consists of its last terms, i.e. \mathbf{J}_e (3.25), as the convective velocities \mathbf{v}_i and the osmotic velocities \mathbf{u}_i typically differ by many orders of magnitude. In other words, the probability current \mathbf{J}_{tot} is *always*

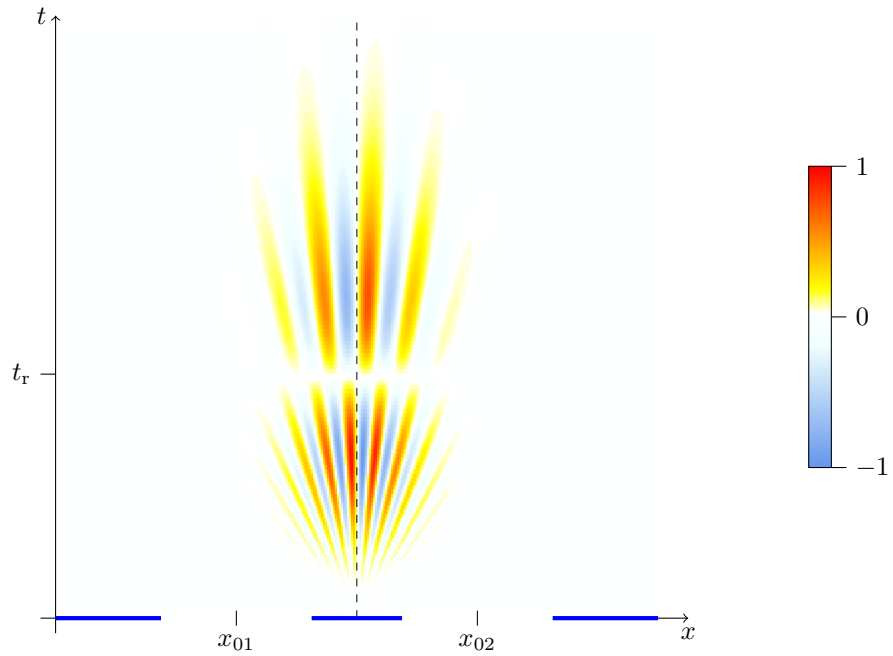


(a) No additional phase

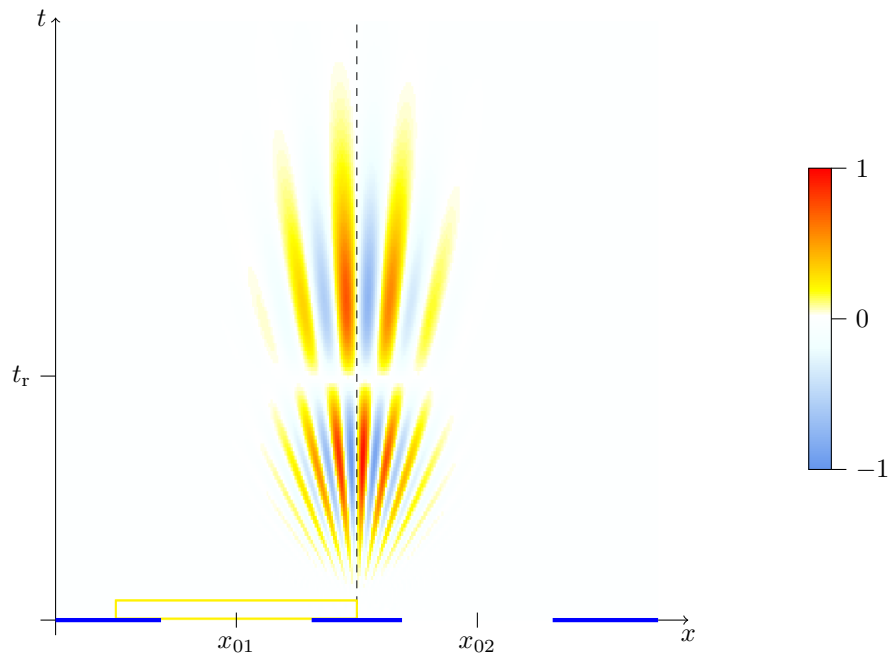


(b) Same as Fig. 3.13(a), with an additional phase $\Delta\varphi = \pi$ at slit 1

Figure 3.13.: Classical computer simulation of the interference pattern in a double-slit experiment; with $v_{x,1} = -v_{x,2}$



(a) Same setup as in Fig. 3.13(a), with arbitrary normalization and $v_{x,1} = -v_{x,2}$



(b) Same as Fig. 3.14(a), with an additional phase shift of $\Delta\varphi = \pi$ at slit 1

Figure 3.14.: Classical computer simulation of the total average entangling current density \mathbf{J}_e in a double-slit experiment

dominated by the quantum mechanical *entangling current* \mathbf{J}_e (3.25) which is connected to the osmotic velocities, \mathbf{u}_1 and \mathbf{u}_2 , and implies the existence of strong correlations. As we have just seen, this entangling current can also be understood as describing the heat flow between the two channels. As opposed to the average total probability current \mathbf{J}_{tot} , in the distribution of the probability density P_{tot} (3.14) alone the entangling part is not explicitly visible.

The phenomenon of entanglement is thus possibly rooted in the existence of the path excitation field. In other words, one can say that the entanglement characteristic for two-particle interferometry is a natural consequence of the fact demonstrated here, i.e. that already in single-particle interferometry one deals with entangling currents, which generally are of a nonlocal nature.

3.5. Multi-slit interference and the quantum Talbot effect

We can already infer from the three-slit device that due to the pairwise selection of the velocity field components \mathbf{v}_i and \mathbf{u}_i , $i = 1, \dots, N$, N being the number of slits, the interference effect of every higher order grating can be reduced to successive double-slit algorithms (cf. [Fus14]). For a compact description of the N -slit case we return to the notation (3.7) of general velocity vectors \mathbf{w}_i with

$$\begin{aligned} \mathbf{w}_1 &:= \mathbf{v}_1, & \mathbf{w}_2 &:= \mathbf{u}_1, \\ \mathbf{w}_3 &:= \mathbf{v}_2, & \mathbf{w}_4 &:= \mathbf{u}_2, \\ &\vdots & &\vdots \\ \mathbf{w}_{2N-1} &:= \mathbf{v}_N, & \mathbf{w}_{2N} &:= \mathbf{u}_N, \end{aligned} \tag{3.28}$$

with $\mathbf{w}_{2i-1} := \mathbf{v}_i$ and $\mathbf{w}_{2i} := \mathbf{u}_i$, $i = 1, \dots, N$, denoting the convective and osmotic velocities, respectively, for each slit i . Analogously, we define the amplitudes

$$\begin{aligned} R_{\mathbf{w}_1} &= R_{\mathbf{w}_2} = R_1, \\ R_{\mathbf{w}_3} &= R_{\mathbf{w}_4} = R_2, \\ &\vdots \\ R_{\mathbf{w}_{2N-1}} &= R_{\mathbf{w}_{2N}} = R_N. \end{aligned} \tag{3.29}$$

According to the Eqs. (3.12) to (3.10), now with a general number N of slits, the calculation for the total probability density is straightforward, as only contributions of

the convective velocities are involved. We get

$$\begin{aligned}
 P_{\text{tot}}^N &= \sum_{i=1}^{2N} P_{\mathbf{w}_i} = \sum_{i=1}^{2N} \hat{\mathbf{w}}_i R_{\mathbf{w}_i} \cdot \sum_{j=1}^N \hat{\mathbf{v}}_j R_j = \left(\sum_{i=1}^N \hat{\mathbf{v}}_i R_{\mathbf{v}_i} \right)^2 \\
 &= \sum_{i=1}^N P_{\mathbf{v}_i} = \sum_{i=1}^N \left(R_i^2 + \sum_{j=i+1}^N 2R_i R_j \cos \varphi_{i,j} \right).
 \end{aligned} \tag{3.30}$$

For the generalized current density we obtain

$$\mathbf{J}_{\text{tot}}^N = \sum_{i=1}^{2N} \mathbf{J}_{\mathbf{w}_i} = \sum_{i=1}^{2N} \left(R_{\mathbf{w}_i} \mathbf{w}_i \cdot \sum_{j=1}^N \hat{\mathbf{v}}_j R_{\mathbf{v}_j} \right), \tag{3.31}$$

which leads after a short calculation to

$$\mathbf{J}_{\text{tot}}^N = \sum_{i=1}^N \left(R_i^2 \mathbf{v}_i + \sum_{j=i+1}^N R_i R_j \left\{ (\mathbf{v}_i + \mathbf{v}_j) \cos \varphi_{i,j} + (\mathbf{u}_i - \mathbf{u}_j) \sin \varphi_{i,j} \right\} \right) \tag{3.32}$$

with $\varphi_{i,j} = \sphericalangle(\mathbf{v}_i, \mathbf{v}_j) = \sphericalangle(\mathbf{u}_i, \mathbf{u}_j)$ as sketched in Fig. 3.2.

From these results we can clearly see that the addition of an arbitrary number of slits represents a simple inductive extension from the double-slit case as we had stated in the previous section.

In well-known manner one obtains the trajectories from $\dot{\mathbf{x}}_{\text{tot}} = \mathbf{v}_{\text{tot}} = \frac{\mathbf{J}_{\text{tot}}}{P_{\text{tot}}}$ [SM08]. As opposed to this analytical procedure, we use our simulation tools, which are displayed in the computer simulations of Figs. 3.15 to 3.18 for 7-, 13-, 25-, and 27-slit setup, respectively. Already for the 7-slit case one can observe the emergence of a repetitive short range pattern until the Fraunhofer regime¹⁰ is reached. At the so-called Talbot distance

$$z_T = d^2/\lambda, \tag{3.33}$$

where d denotes the grating period and λ the wavelength of the incident plane wave, the initial patterns of the 7 vertically arranged slit openings reappear with a shift of $d/2$. Table 3.1 shows the results for different values of λ and d , compares them with the observed values y_T of the Talbot distance for various N -slit cases.

To explain these results, we use the parameters for neutrons according to Table 3.1: $d = 1.06$ nm, $\lambda = 1$ nm, with mass $m_n = 1.675 \cdot 10^{-27}$ kg. The spatial step width is chosen as $\Delta x = 0.0378$ nm, the time resolution is set to $\Delta t = 1.92 \cdot 10^{-14}$ s. Then, said

¹⁰The patterns arise in the short range or Fresnel region, gradually disappear in the transition region and end up in the far-field or Fraunhofer region, cf. [SM12].

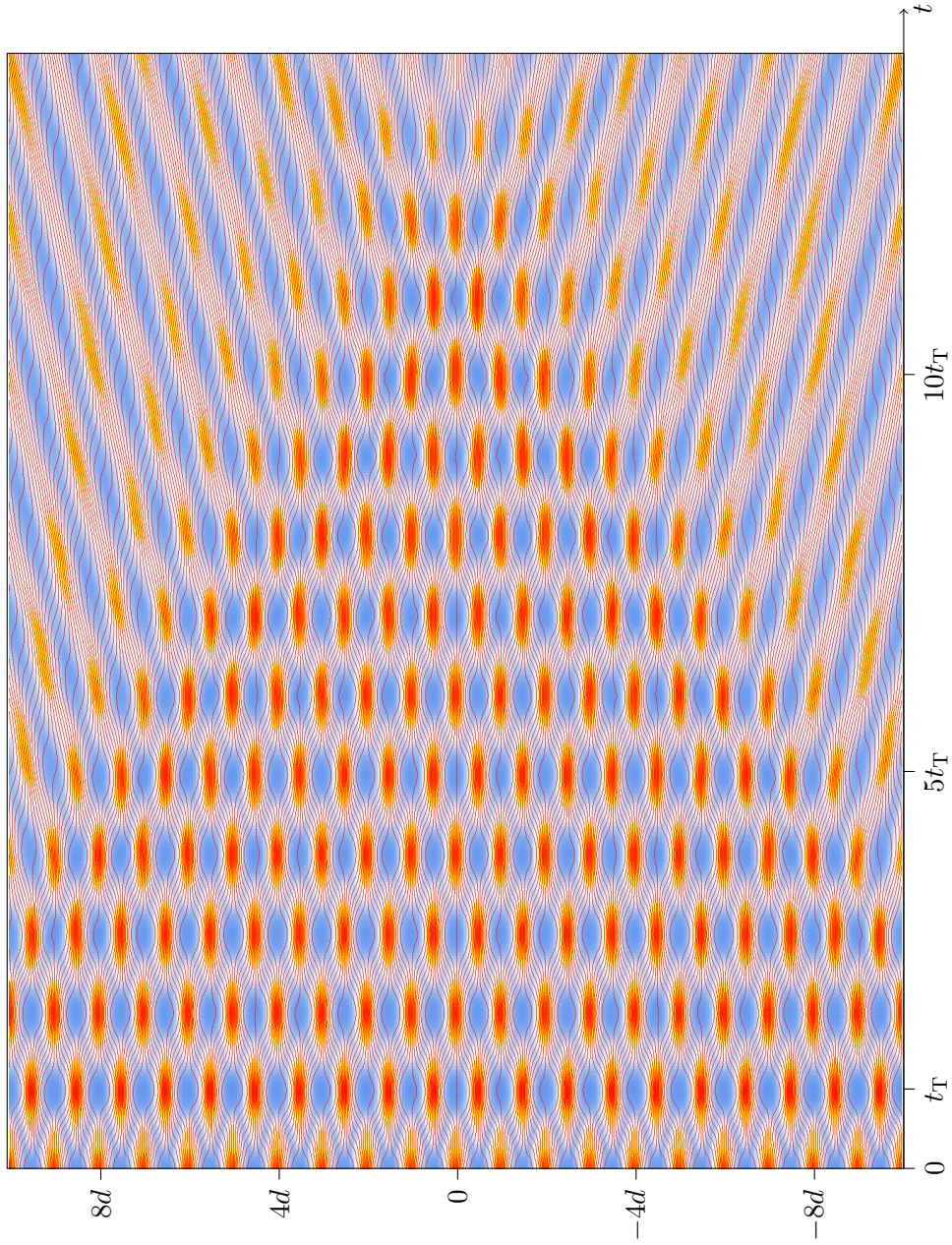


Figure 3.15.: Intensity distribution via classical computer simulation of the Talbot carpet for a 27-slit ($d = 0.53$ nm) setup of Table 3.1, respectively. Averaged particle trajectories are displayed in red.

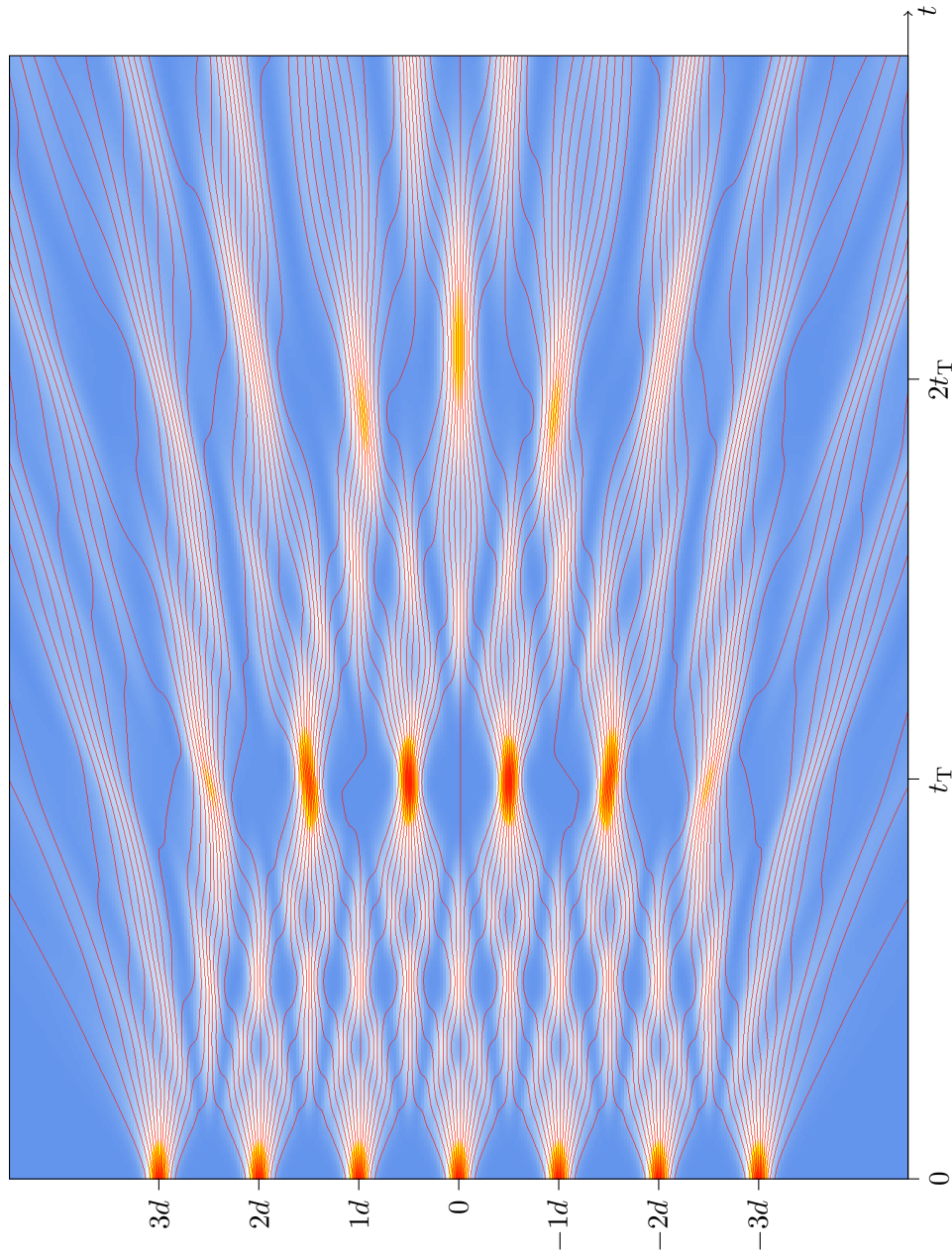


Figure 3.16.: Intensity distribution via classical computer simulation of the Talbot carpet for a 7-slit ($d = 1.06$ nm) setup of Table 3.1, respectively. Averaged particle trajectories are displayed in red.

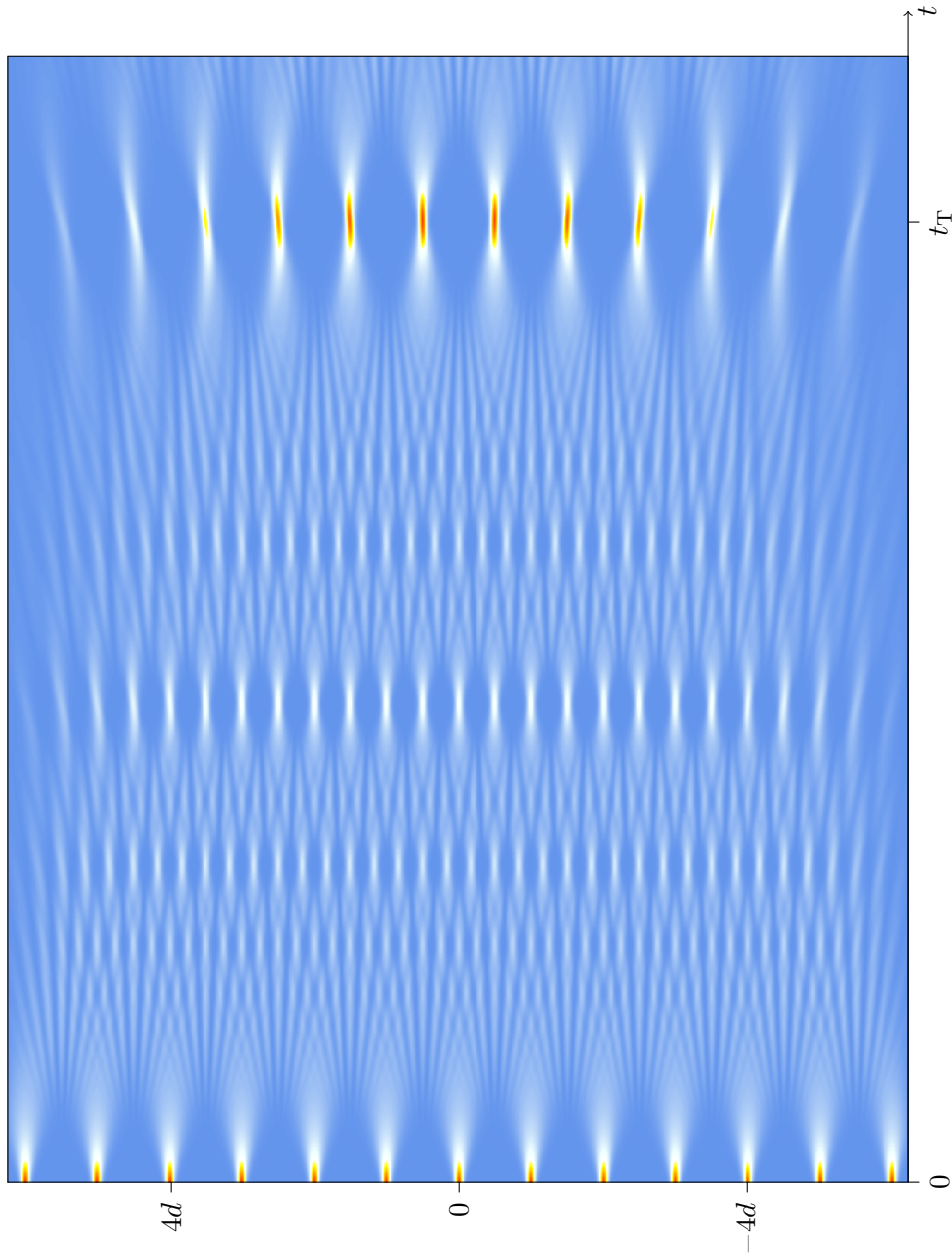


Figure 3.17.: Intensity distribution via classical computer simulation of the Talbot carpet for a 13-slit ($d = 1.59 \text{ nm}$) setup of Table 3.1, respectively.

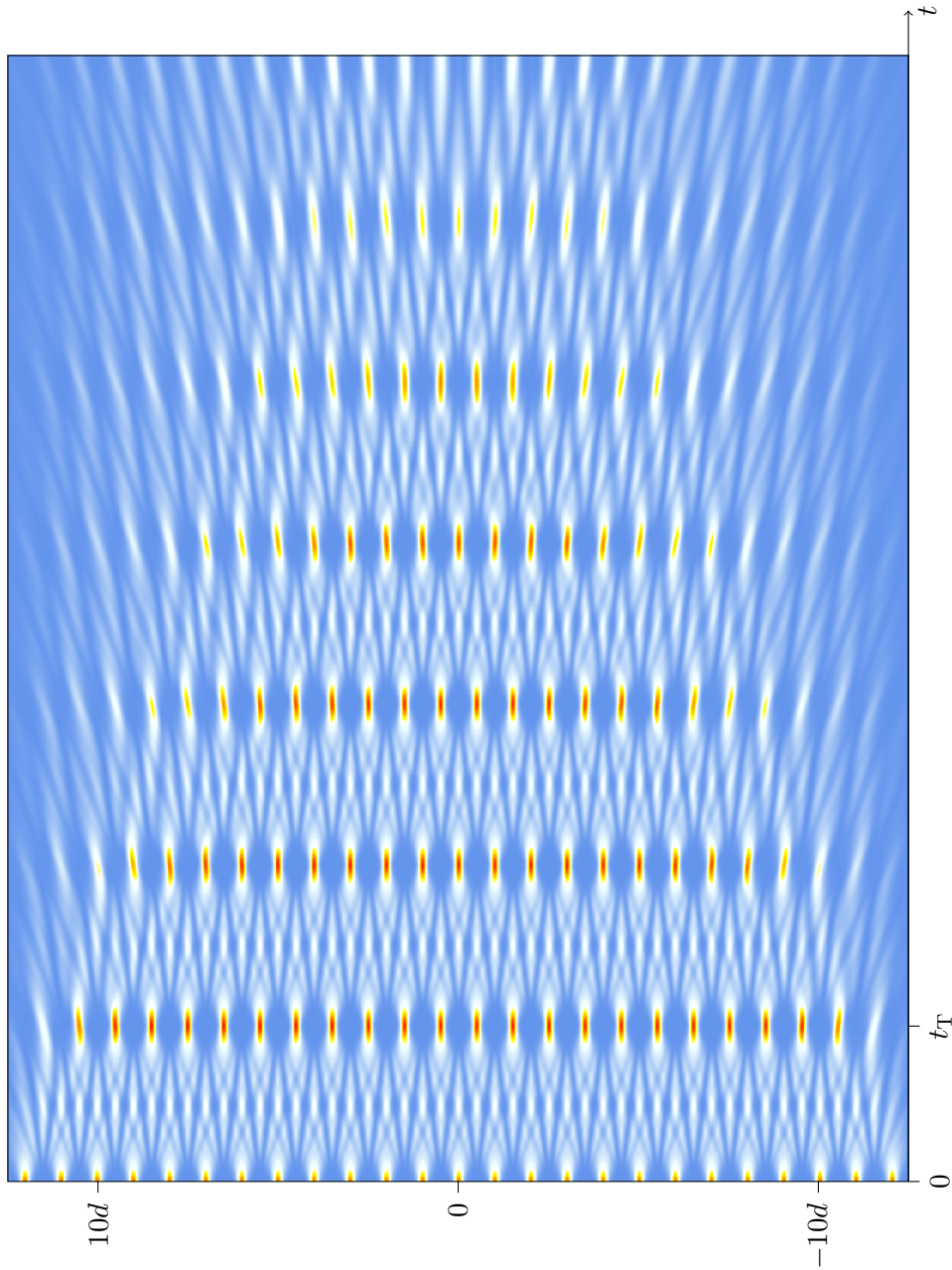


Figure 3.18.: Intensity distribution via classical computer simulation of the Talbot carpet for a 25-slit ($d = 2.12 \text{ nm}$) setup of Table 3.1, respectively.

Setup	Fig. 3.15	Fig. 3.16	Fig. 3.17	Fig. 3.18
λ	1 nm	1 nm	1 nm	1 nm
d	0.53 nm	1.06 nm	1.59 nm	2.12 nm
z_T	0.28 nm	1.13 nm	2.53 nm	4.5 nm
$y_{T,7\text{-slit}}$	0.28 nm	1.14 nm	2.53 nm	4.52 nm
$y_{T,N\text{-slit}}$	0.29 nm ($N = 27$)	1.13 nm (27)	2.53 nm (25)	4.49 nm (13)

Table 3.1.: Parameters for the Talbot carpet simulations

shifted reappearance of the pattern occurs for the first time at time step 150, i.e. at $t_T = 150 \cdot \Delta t = 2.88 \cdot 10^{-12}$ s. The standard transformation into the two-dimensional case by re-parametrizing the t -axis according to Eq. (2.1), $y = \hbar k_n \Delta t / m_n = h \Delta t / (\lambda m_n)$, leads to the observed distance $y_T = h t_T / (\lambda m_n) = 1.14$ nm, which matches nicely with the formula of the Talbot distance z_T (3.33). The observed values for the Talbot distance y_T in our discretised model agree for any N -slit setup as expected in accordance with Eq. (3.33), which only depends on d and λ . Moreover, we also obtain the correct results for any other choice of m or λ .

For multiples of $2z_T$ the recurrence of the original state is observed, as it is particularly obvious in the case of 27 slits. Due to the non-crossing of all trajectories, as has been discussed in section 3.3, the caverns in the middle stay confined until they are broken up by the influence of the boundary area via the light-like cone. In the limit of an indefinitely extended grating the pattern clearly would be maintained *ad infinitum*.

Since the averaged trajectories obtained with our derived current set are identified with the Bohmian trajectories of Sanz *et al.* [SM07], we have thus shown that the emerging quantum carpet for N slits constituted by characteristic repetitive patterns can be reproduced without any quantum mechanical state function.

3.6. Conclusions and outlook

It has also been shown how our model entails the existence of a path excitation field, i.e. a field spanned by the average velocity fields \mathbf{v} and \mathbf{u} , respectively, where the latter refers to diffusion processes reflecting also the stochastic parts of the zero-point field. Then, on the basis of classical physics, the exact intensity distribution on a screen behind a double-slit has been derived, as well as the details of the more complicated particle

current, or of the Bohmian particle trajectories, respectively.

Furthermore, general formulas for the N -slit current densities have been derived, thus enabling us to give a micro-causal account for the kinematics of the quantum Talbot effect. The Talbot distance could be reproduced also quantitatively in this model.

4. Beam attenuation in double-slit experiments

In this chapter we shall employ a double-slit setup with one slit's probability density being attenuated by a huge factor. Therefore, we start with a survey on different absorber types used in interference experiments and discuss the resulting consequences of using these.

In a phenomenological approach we shall study the probability distribution of said double-slit and show the emergence of a lateral drift of the interference zone due to increasing attenuation factors applied to one of the slits. This drift phenomenon, the *quantum sweeper effect*, will be compared to both coherent and incoherent beams and shown to be existing in either case.

As a result of our investigations we shall propose an advanced measurement method comprising a side-screen which is oriented along the spreading direction, i.e. the side-screen turned by an angle of 90° compared to its usual position.

4.1. Outline

In the search of new, and perhaps surprising, features of quantum systems, one option is to steadily decrease the intensity of a slit into one spatially constrained area, as compared to a reference intensity in another, equally constrained area. For example, one can employ the usual double-slit experiments and modify one of the two slits' channels in such a way that the corresponding outgoing probability density is very low compared to that of the other slit. We call a combination of such distributions of high and low probability densities, or intensities, respectively, *intensity hybrids* (cf. [Grö15a; Grö15b; Grö16a; Mes16]).

Since the 1980ies, one possibility to experimentally establish and probe such hybrids has been through the introduction of beam attenuation techniques, as demonstrated in the well-known papers by Rauch's group in neutron interferometry [Rau90; RS84]. Here, we re-visit these experiments and results from a new perspective, and we also discuss new, previously unexpected effects. Our main result is that in employing ever weaker

channel intensities, nonlinear effects become ever more important, which are a crucial characteristic of sub-quantum models such as the one developed by our group. Whereas the intensity distributions are predicted to be the same for the standard quantum mechanical as well as our approach, respectively, more detailed information is available when the behaviour of average trajectories is studied.

4.2. Deterministic and stochastic beam attenuation

4.2.1. Beam attenuation in neutron interferometry

Deterministic and stochastic beam attenuation have been studied extensively in neutron interferometry, beginning with the work by Rauch and Summhammer in 1984 [RS84]. More recently, an interesting model of these results has been presented by De Raedt *et al.* [DeR12] with the aid of event-by-event simulations, thus confirming the possibility to describe the known results even without the use of quantum mechanics.

In [Rau90; RS84], a beam chopper (Fig. 4.1) was used as a deterministic absorber in one arm of a two-armed interferometer, whereas for stochastic absorption semitransparent foils of various materials were used. Despite the net effect of the same percentage of neutrons being attenuated, the quantum mechanical formalism predicts the following

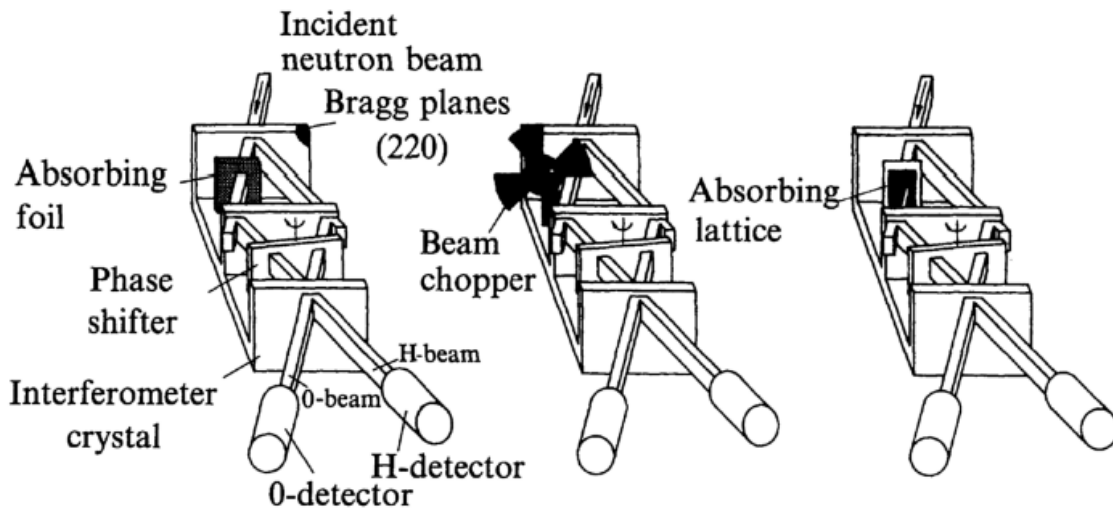


Figure 4.1.: Stochastic type absorber (left and right) and deterministic type absorber (middle). From [Sum87]

different behaviours for the two cases. Introducing the *transmission factor* a as the beam's transmission probability, in the case of a (deterministic) chopper wheel it is given by the temporal open-to-closed ratio,

$$a = \frac{t_{\text{open}}}{t_{\text{open}} + t_{\text{closed}}}, \quad (4.1)$$

whereas for a (stochastic) semitransparent material defined by its absorption cross section, it is simply the relation of the intensity I with absorption compared to the intensity I_0 without, i.e.

$$a = \frac{I}{I_0}. \quad (4.2)$$

In a quantum mechanical description the beam modulation behind the interferometer is obtained in the following two forms. For the deterministic chopper system the intensity I_{det} is, with φ denoting the phase difference, given by¹ [RS84]

$$I_{\text{det}} \propto (1 - a) |\psi_1|^2 + a |\psi_1 + \psi_2|^2 \propto 1 - a + a |1 + e^{i\varphi}|^2 = 1 + a + 2a \cos \varphi, \quad (4.3)$$

whereas for stochastic beam attenuation with the semitransparent material the intensity I_{sto} is

$$I_{\text{sto}} \propto |\psi_1 + \psi_2|^2 \propto 1 + a + 2\sqrt{a} \cos \varphi. \quad (4.4)$$

Although the same number of neutrons is observed in both cases, in the first one the contrast of the interference pattern is proportional to a , whereas in the second case it is proportional to \sqrt{a} .

In our accounting for the just described attenuation effects, we choose the usual double-slit scenario, primarily because this will be very useful later on when discussing more extreme intensity hybrids.

4.2.2. Application to deterministic and stochastic beam attenuation experiments

Let us now display some typical results from our double-slit approach, as presented in chapter 3, to beam attenuation. We can simulate the propagation of a Gaussian whose

¹The quantum mechanical wave function ψ_j , for slits $j = 1$ or 2 , is connected with the probability density P_j and the amplitude R_j by

$$P_j = R_j^2 = |\psi_j|^2 = \psi_j^* \psi_j$$

variance increases due to the ballistic diffusion process (see chapter 2.5). To begin with, we consider deterministic attenuation first. Therefore, we use the ratio a (4.1) and simulate indirectly as a combination of

1. a single-slit experiment resulting in distribution $P_{\text{single}} = P_1 = R_1^2$, according to Eq. (3.3), as slit 2 is closed during time t_{closed} , and
2. a double-slit experiment resulting in $P_{\text{double}} = P_{\text{tot}}$ (3.14) with both slits are opened, both beams having equal intensities, during time t_{open} .

As the ratio of the two intensities is set to $P_1 = P_2$ the resulting distribution after incoherent summing up reads

$$\begin{aligned}
 P_{\text{det}} &= (1 - a)P_{\text{single}} + aP_{\text{double}} \\
 &= (1 - a)P_1 + a(P_1 + P_1 + 2\sqrt{P_1 P_1} \cos \varphi) \\
 &= P_1 + aP_1 + 2aP_1 \cos \varphi \\
 &= P_1(1 + a + 2a \cos \varphi).
 \end{aligned} \tag{4.5}$$

Accordingly, we have in complete agreement with Eq. (4.3) that

$$I \propto 1 + a + 2a \cos \varphi. \tag{4.6}$$

For stochastic attenuation we find with the intensity ratio a (4.2), i.e. $P_2 = aP_1$, thus with the amplitude of the attenuated slit 2, and according to Eq. (3.14) that

$$\begin{aligned}
 P_{\text{sto}} &= P_1 + P_2 + 2\sqrt{P_1 P_2} \cos \varphi \\
 &= P_1 + aP_1 + 2\sqrt{aP_1 P_1} \cos \varphi \\
 &= P_1(1 + a + 2\sqrt{a} \cos \varphi).
 \end{aligned} \tag{4.7}$$

Again, we have complete agreement with Eq. (4.4), i.e.

$$I \propto 1 + a + 2\sqrt{a} \cos \varphi. \tag{4.8}$$

In Fig. 4.2 we show the results of our computer simulations following Eqs. (4.5) and (4.7), respectively, for the probability density distributions of a neutron beam for three different values of the beam transmission factor a . The typical wavelength used is $\lambda = 1.8 \text{ nm}$ (cf. [RW00]). The Gaussian slits each are $22 \mu\text{m}$ wide, with their centres being $200 \mu\text{m}$ apart, and the intensity distributions are recorded on a screen located in the forward direction at a distance of 5 m from the double-slit. Corresponding to the different behaviours of the contrast in deterministic and stochastic attenuation,

respectively, one can see the different contributions to the overall probability density distribution, with the differences becoming smaller and smaller with ever decreasing transmission factor a . For consistency, we have also checked and confirmed that the total areas below the two curves are identical, as they must be in order to represent the same overall throughput of the number of neutrons.

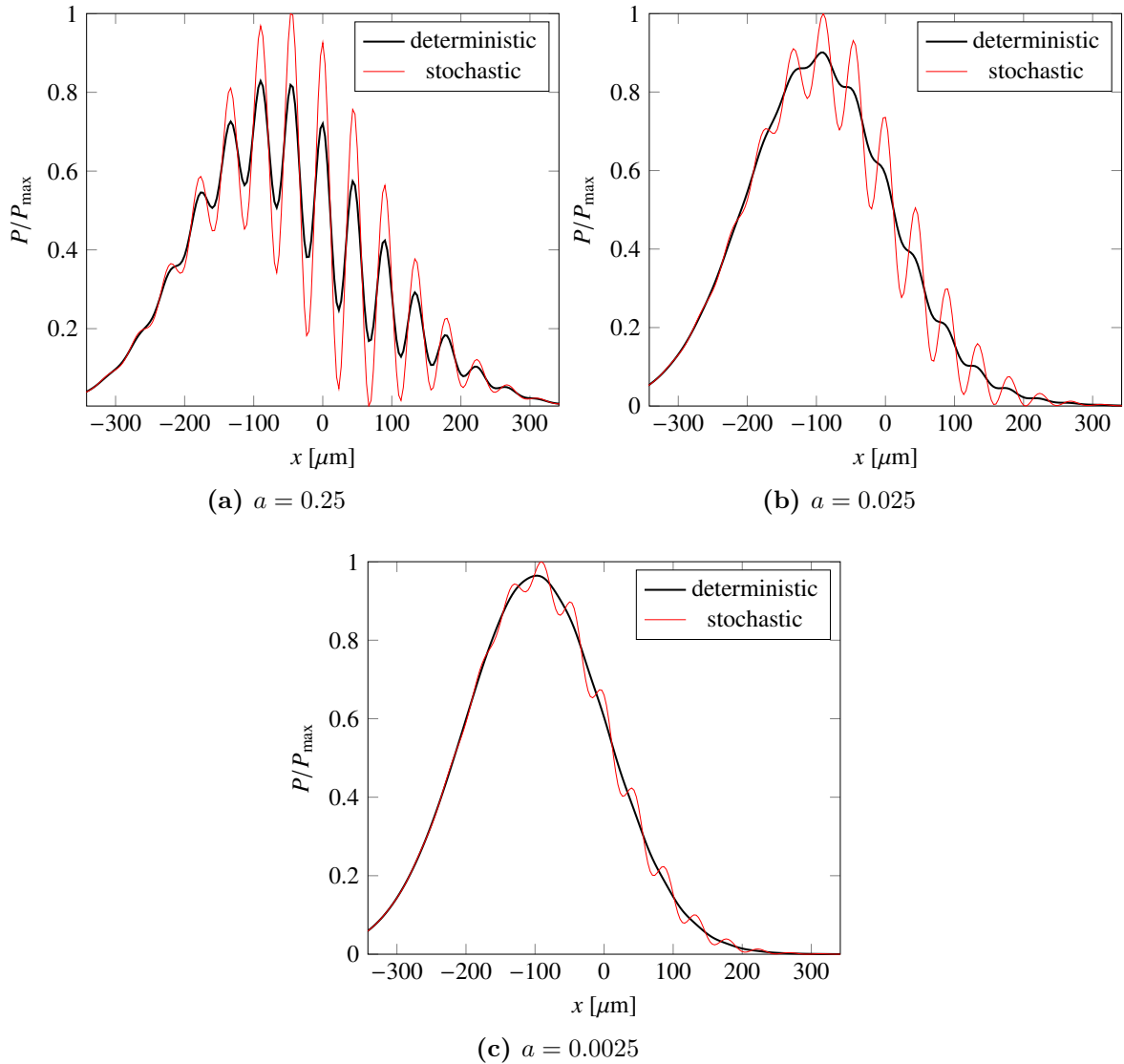


Figure 4.2.: Simulation of probability density distributions with beam attenuation a at slit 2, in complete accordance with standard quantum mechanics.

4.3. Phenomenology of the quantum sweeper for coherent and incoherent beams

We assume a coherent beam in a double-slit experiment, with the intensity distribution being recorded on a screen, and we are going to discuss a particular effect of the stochastic attenuation of one of the two emerging Gaussians at very small transmission factors. With the appropriate filtering of the particles going through one of the two slits, the recorded probability density in the surroundings of the experiment will appear differently compared to what one would normally expect. That is, if one had a low beam intensity coming from one slit, one would expect that the contributions from the fully open slit would become dominant until such a low counting rate from the attenuated slit is arrived at that essentially one would have a one-slit distribution of recorded particles on the screen. This tendency is at least clearly visible in Fig. 4.2. One would thus expect for ever smaller values of a that the oscillatory behaviour of the stochastic case would more and more disappear to finally merge with the smoothed-out pattern of an essentially one-slit distribution pattern, and that no other effects would be observed.

Interestingly, this is not exactly what one obtains at least for very low values of a when going through the calculations and computer simulations² with our bouncer model. The latter encompasses, among other features, an explicit form of the velocity field \mathbf{v}_{tot} (3.22) emerging from the double slit, as well as of the probability current \mathbf{J}_{tot} (3.21) associated with it. Whereas full agreement exists with the standard quantum mechanical prediction of the probability density P_{tot} , viz. Eqs. (4.5) and (4.7), respectively, the probability current \mathbf{J}_{tot} exhibits an unexpected behaviour, which we are going to discuss now.

Fig. 4.3 shows the quantum sweeper effect: A series of probability density distributions plus averaged trajectories for the case that the intensity in slit 2 is gradually diminished. We use the same model as described in section 2.6: Wave packets, represented by plane waves in the forward y -direction, from a coherent source passing through soft-edged slits in a barrier, located along the x -axis, and recorded at a screen in the forward direction, i.e. parallel to the barrier. This situation is described by two Gaussians representing the totality of the effectively heated-up path excitation field, one for slit 1 and one for slit 2, whose centres have the same distances from the plane spanned by the source and the centre of the barrier along the y -axis, respectively (see Fig. 3.2).

Now, with ever lower values of the transmission factor a during beam attenuation, one can see a steadily growing tendency for the low counting rate particles of the attenuated beam to become swept aside. In our model, this is straightforward to understand, because we have the analytical tools to differentiate between the forward

²See chapter 5 on how simulations have been practically realized.

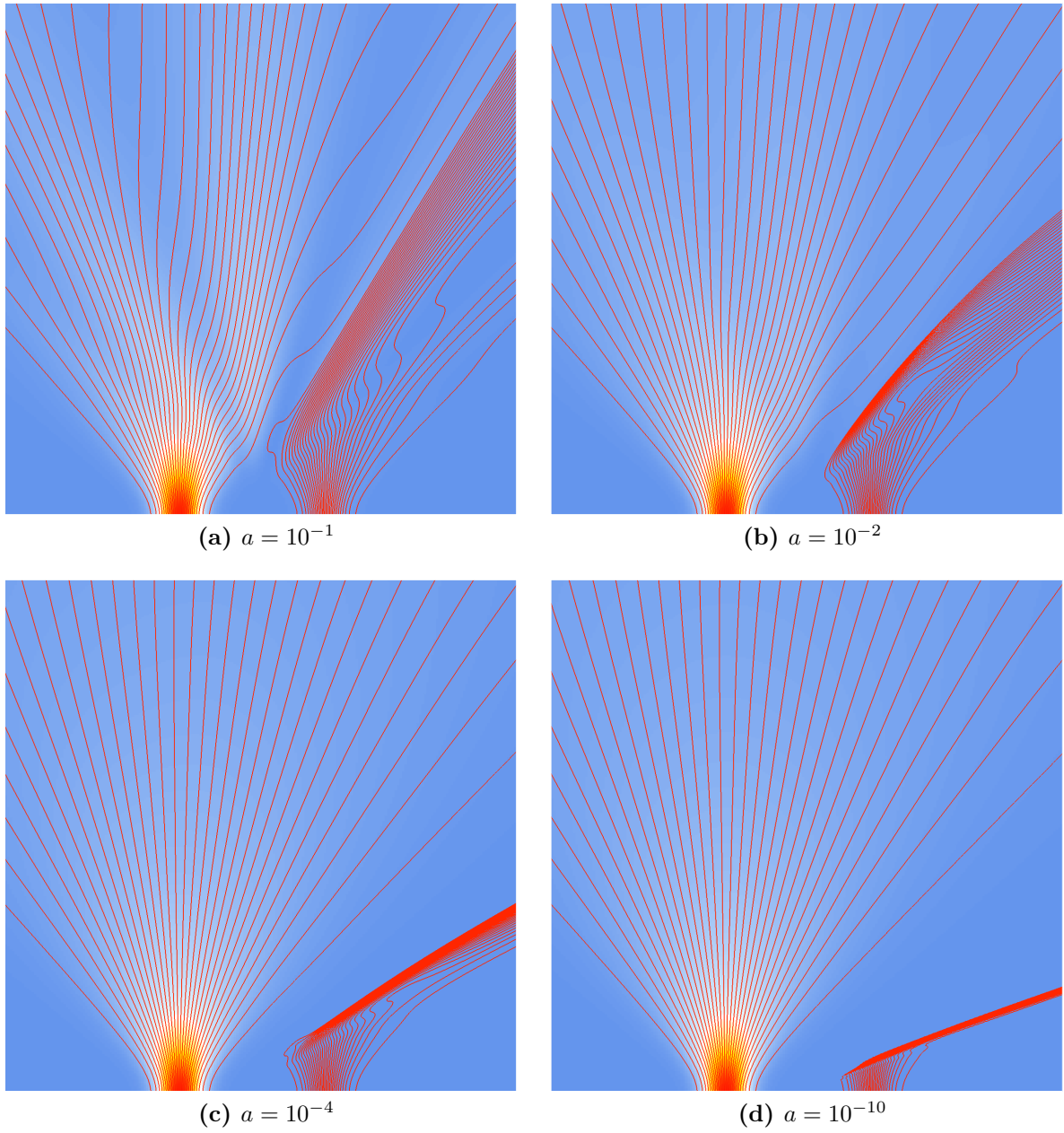


Figure 4.3.: The quantum sweeper effect for different transmission factors a . To demonstrate the effect more clearly, we use the same number of trajectories for each slit.

convective \mathbf{v}_i (3.23) and the osmotic influences of velocities \mathbf{u}_i (3.24), as distinguishable contributions from the different slits i . Thus, it is processes of diffusion which are seen in operation here, due to the presence of accumulated heat, i.e. kinetic energy, primarily in the strong beam. So, in effect, we understand Fig. 4.3 as the result of the vacuum heat sweeping aside the very low intensity beam, with a no-crossing line³ defined by the balancing out of the diffusive momenta, $m(\mathbf{u}_1 + \mathbf{u}_2) = 0$.

Importantly, for certain slit configurations and sizes of the transmission factor, the sweeper effect leads to a bunching of trajectories which may become deflected into a direction almost orthogonal to the original forward direction. In other words, one would need much wider screens in the forward direction to register them, albeit then weakened due to a long travelling distance. On the other hand, if one installed a screen orthogonal to the forward screen, i.e. one that is parallel to the original forward motion – and thus to the y -axis – one could significantly improve the contrast and thus register the effect more clearly (see also Fig. 4.5 further below). Further, we note that changing the distance between the two slits does not alter the effect, but demonstrates the bunching of the low counting rate arrivals in essentially the same narrow spatial area even more drastically. So, again, if one places a screen orthogonally to the forward direction, one registers an increased local density of particle arrivals in a narrow spatial area under an angle that is independent of the slit distance.

Let us now turn to the case of incoherent beams. For, although we shall refrain from constructing a concrete model of incoherence and implementing it in our schema, we already have the tools of an effective theory, i.e. to describe incoherence without the need of a specified mechanism for it. Namely, as full incoherence between two (Gaussian or other) beams is characterized by the complete absence of the interference term in the overall probability distribution of the system, this means that $P_{\text{tot}} = R_1^2 + R_2^2$, since the interference term

$$R_1 R_2 (\mathbf{v}_1 + \mathbf{v}_2) \cos \varphi = 0 \tag{4.9}$$

vanishes. For the case $\cos \varphi = 0$, i.e. with $\varphi = \frac{\pi}{2}$, Eq. (4.9) vanishes which effectively describes the situation of two incoherent beams in the double-slit system. What about the two interference terms in the probability current \mathbf{J}_{tot} (3.21), then? Well, the first term is identical with the vanishing (4.9), but for the second term we obtain from entangling current (3.25) with $\varphi = \frac{\pi}{2}$

$$\frac{\hbar}{m} R_1 R_2 \left(\frac{\nabla R_2}{R_2} - \frac{\nabla R_1}{R_1} \right) = \frac{\hbar}{m} (R_1 \nabla R_2 - R_2 \nabla R_1). \tag{4.10}$$

³From the assumed uniqueness and differentiability of $S(\mathbf{x}, t)$ follows that the paths don't cross each other. See section 2.3 for further explanations. However, at this stage we are discussing an ontological point of view on how the no-crossing phenomenon can be explained.

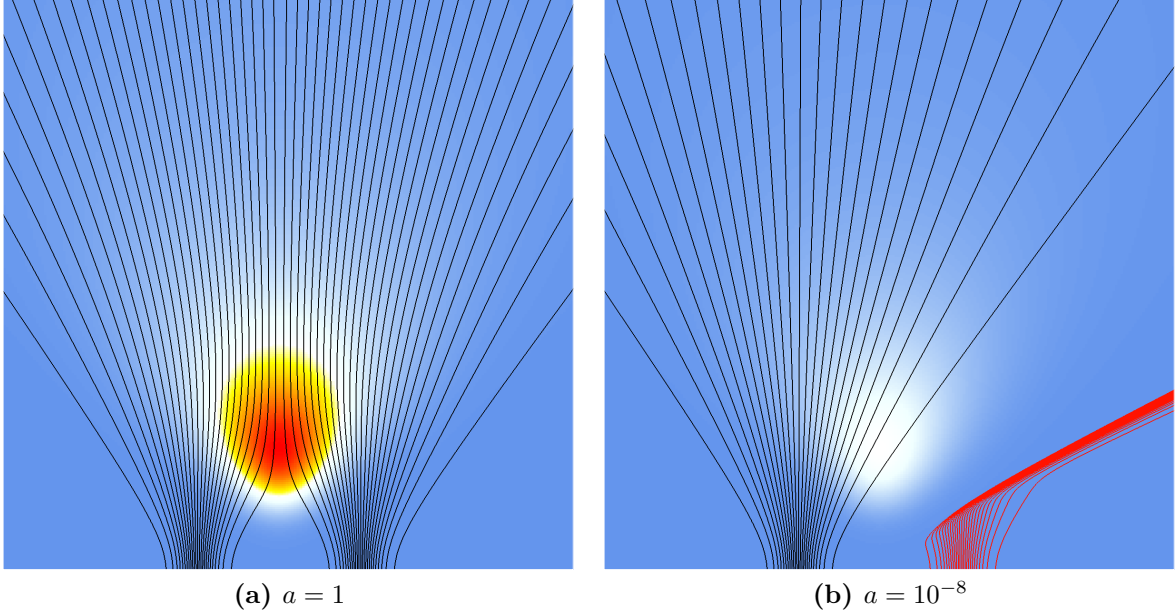


Figure 4.4.: Double-slit experiment with completely incoherent channels. The right hand side beam is weakened by factor a .

As the distributions R_i may have long wiggly tails – summing up, after many identical runs, to a Gaussian with no cut-off, but spreading throughout the whole domain of the experimental setup (cf. section 2.2 and [Grö13]) – the expression (4.10) is not at all guaranteed to vanish. In fact, a look at Fig. 4.4 shows that there is an effect even for incoherent beams: Although the product $R_1 R_2$ is negligible and therefore leads to no interference fringes on the screen, nevertheless expression (4.10) has the effect of bending average trajectories so as to obey the no-crossing rule well known from our model as well as from Bohmian theory.

As was already pointed out in [SB09], or more recently, in [LS15], the resulting trajectories of Fig. 4.4(a) can be understood as a nonlinear effect that is not usually considered in standard quantum mechanics, but explainable in the Bohmian picture. There, it is the structure of the velocity field which is genuinely nonlinear and therefore allows for the emergence of the type of trajectory behaviour. However, also in our approach, the emergence of the trajectories of Fig. 4.4 is completely understandable as it can be traced back to the non-vanishing of expression (4.10): The average trajectories never cross the central symmetry line in Fig. 4.4(a), a fact due to the diffusion related hot spot indicated in red-to-yellow-to-white (depicting both interference terms of Eq. (4.10)), which represents a kinetic energy reservoir that effectively gives particles a push in the

forward direction; The intensity of Eq. (4.10) is weakened by the factor $a = 10^{-8}$ in Fig. 4.4(b), which is why it does not affect the strong beam. However, it is sufficient for the attenuated beam to become deflected.

In sum, then, performing a double-slit experiment with incoherent beams leads to an emergent behaviour of particle propagation which can be explained by the effectiveness of diffusion waves with velocities \mathbf{u}_i interacting with each other, thereby creating a hot spot where the intensity of the diffusive currents is highest and leads to a deflection into the forward direction such that no-crossing of the average velocities beyond the symmetry line is made possible (Fig. 4.4(a)). This is therefore in clear contradiction to the scenario where only one slit is open for the particle to go through. If the slits are not open simultaneously, the particles could propagate to locations beyond the symmetry line, i.e. to locations forbidden in the case of the second slit being open. [SB09]

As our velocity fields \mathbf{v}_i (3.23) and \mathbf{u}_i (3.24) are identical with the Bohmian and the osmotic momentum, respectively, one can relate them also to the technique of weak measurements. The latter have turned out [dGdG16; dGos16; Hil12; Hil16; Lea05; Wis07] to provide said velocities as *weak values*, which are just given by the real and complex parts of the quantum mechanical expression

$$\frac{\langle \mathbf{r} | \hat{p} | \Psi(t) \rangle}{\langle \mathbf{r} | \Psi(t) \rangle}, \quad (4.11)$$

i.e. the weak values associated with a weak measurement of the momentum operator \hat{p} followed by the usual (“strong”) measurement of the position operator \hat{r} whose outcome is \mathbf{r} . In other words, in principle the trajectories for intensity hybrids generally, and for the quantum sweeper in particular, are therefore accessible to experimental confirmation.

In the standard quantum mechanical description of double-slit experiments with intensity hybrids one is usually only concerned with the gradual fading out of wave-like properties like interference fringes. However, in our model we are dealing with diffusion-based wave-like properties throughout all magnitudes of attenuation of, e.g., slit 2, even in the case of incoherent beams. For here, if we observe particles coming through slit 2 characterized by a very low intensity such as $a = 10^{-8}$, one faces the sweeper effect (Fig. 4.5).

The number $n(a)$ of particles which we do see come through slit 2 and which produces the distribution (red) in Fig. 4.5(a) actually is deflected from the forward screen when slit 1 is opened, but the same number $n(a)$ can easily be detected on the sideways screen to the right in Fig. 4.5(b). Although the particles would eventually also be detected on a more elongated forward screen as in Fig.4.7, the effect would be much smaller simply due to the geometry, whereas the sideways screen setup allows the registration with maximal contrast. In principle, for beam attenuation as schematized in Fig. 4.5, if one employs a sideways screen, one thus obtains a different outcome than the one

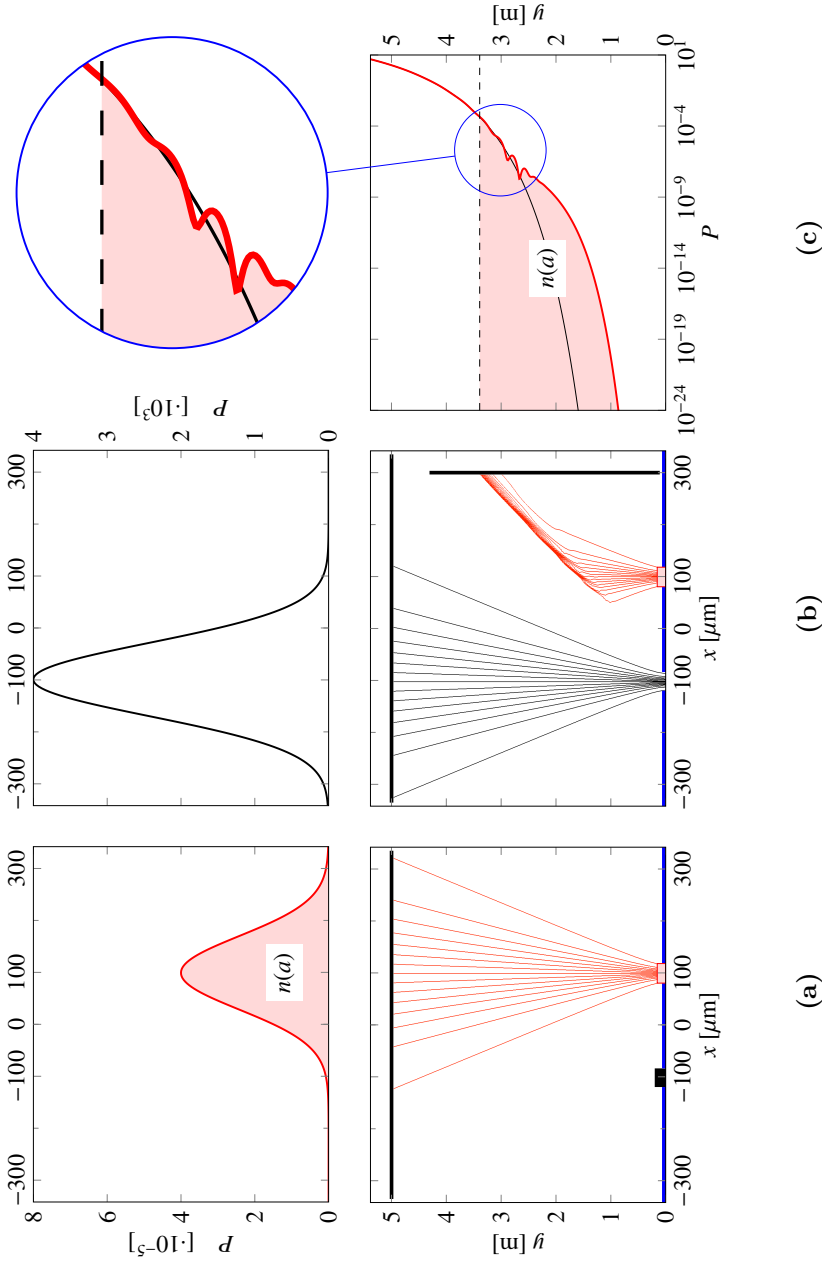


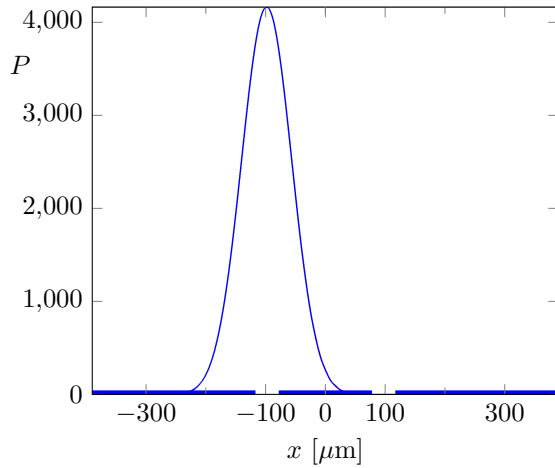
Figure 4.5.: Registration of particles during extreme beam attenuation, $a = 10^{-8}$. (a) If slit 1 is closed, a small number $n(a)$ of particles coming from slit 2 is registered on the forward screen. (b) If, then, slit 1 is fully opened (i.e. with $a = 1$), one registers a much higher number of particles for slit 1, but apparently none for slit 2. Instead, $n(a)$ particles are then registered on the sideways screen parallel to the y -axis. (c) The probability density distribution for the latter exhibits marked signs of interference effects due to the compressed wave superpositions within the bunching area caused by the sweeper effect.

expected due to standard quantum mechanical lore. According to the latter, the beam from slit 2 should be unaffected by the situation at slit 1. This would mean that in the unaffected scenario less than a number of $\frac{n(a)}{2}$ particles could eventually be registered on any sideways screen parallel to the y -axis along a wide spatial extension, whereas our result predicts that the totality of the number $n(a)$ of particles can be registered within a comparatively narrow spatial domain. In Fig. 4.5(c), the vertical screen setup reveals interesting features of the probability density distribution, accounting both for the interference and the sweeper effects. The black line indicates the continuation of the probability density distribution for the one-slit case, which is of course being modified once the interference effect in the coherent case of adding an attenuated beam is allowed for. However, even in the incoherent scenario not showing the comparatively small interference effects, one still obtains the full sweeper effect, with a smooth transition between the two curves in the upper and the lower parts of Fig. 4.5(c), respectively. This is due to the non-vanishing of (4.10), i.e. a significant contribution from the diffusive terms despite the smallness of the transmission factor a .

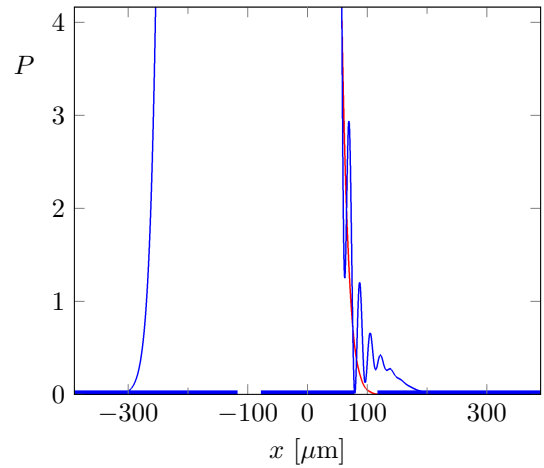
4.4. The quantum mechanical description of the sweeper effect

Let us now consider the stochastic attenuation discussed above in purely quantum mechanical terms. As already mentioned, the probability density distribution is given by Equation (4.4). A graphic representation of this distribution in a distance of 5m from the double slit is shown in Fig. 4.6. Two cases of the attenuation factor at one of the two slits of a double slit system are shown, i.e. $a = 10^{-4}$ and $a = 10^{-8}$ affecting the right slit, respectively. As is to be expected, on a linear scale the distribution will appear as if practically the whole intensity goes through the left un-attenuated slit (Fig. 4.6(a)). Zooming in with a factor of 1000 as shown in Fig. 4.6(b), one can see the faint rest of interference phenomena for the case of $a = 10^{-4}$ (blue), whereas for $a = 10^{-8}$ (red) apparently smooth behaviour is seen. Still, the full effect is best visible on the logarithmic scale shown in Fig. 4.6(c). Compared to the dotted initial distributions for the cases of $a = 10^{-4}$ (blue) and $a = 10^{-8}$ (red), respectively, the whole distribution clearly shows interference phenomena which have been “swept aside” far to the right. The probability distribution for latter is shown in Fig. 4.7 in which the relative positions of the red and blue arrow are the same as in Fig. 4.6(c) indicating the positions of the detected interference zones. Thus, the quantum sweeper effect is confirmed also via orthodox language.

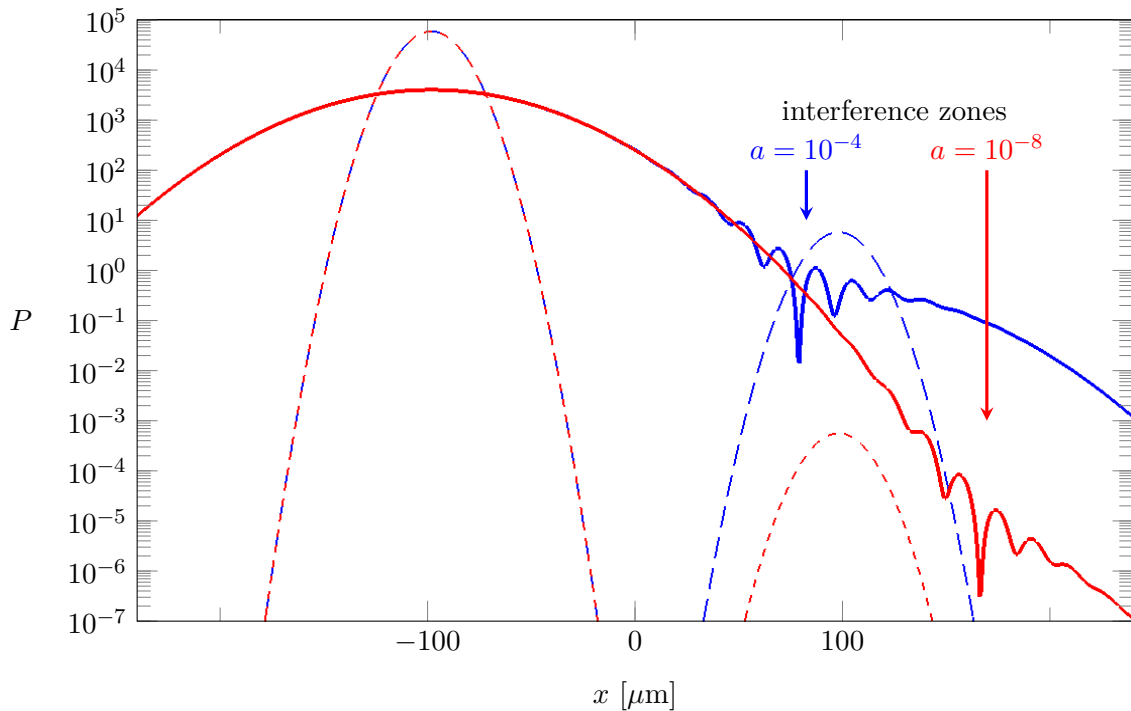
The bunching together of low counting rate particles within a very narrow spatial domain, or channel, respectively, counters naive expectations that with ever higher



(a) The two cases of the attenuation factor at the right slit of a double slit system, i.e. $a = 10^{-4}$ and $a = 10^{-8}$, respectively, essentially provide the same distribution at moderate resolution.



(b) Same as in (a); by zooming in with a factor of 1,000 two cases are discernible: interference phenomena for $a = 10^{-4}$ (blue), *vs.* apparently smooth behaviour for $a = 10^{-8}$ (red).



(c) Same as in (a) on a logarithmic scale. Dotted initial distributions for the cases of $a = 10^{-4}$ (blue) and $a = 10^{-8}$ (red), respectively, evolve into distributions clearly showing interference phenomena which have been “swept aside” far to the right.

Figure 4.6.: The sweeper effect as described by quantum mechanics. Probability density distribution P in a distance of 5 m from the double slit.

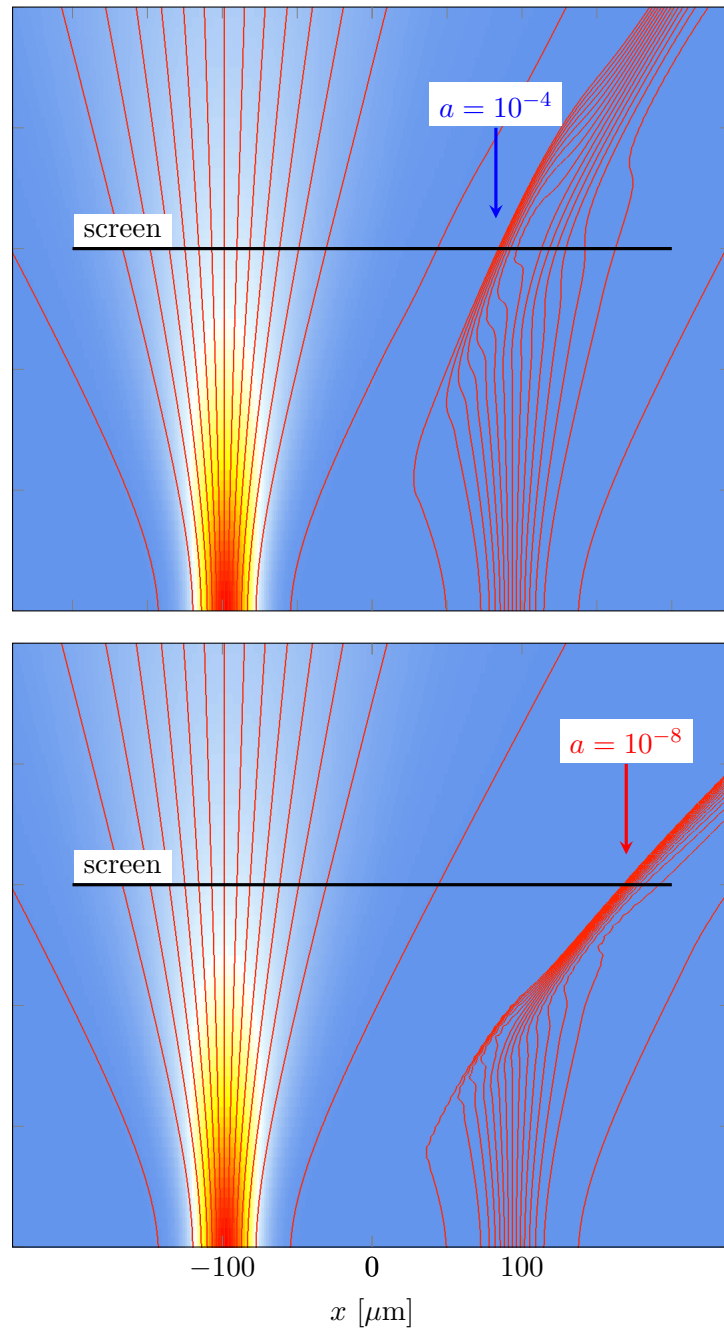


Figure 4.7.: Probability density distributions P emanating from the double slit with transmission factor $a = 10^{-4}$ (top) and $a = 10^{-8}$ (bottom) according to the red and blue distributions in Fig. 4.6, respectively. The arrows indicate the position of the interference zones as measured at the screen.

beam attenuation nothing interesting may be seen any more. The reason why these expectations are not met is given by the explicit appearance of the nonlinear structure of the probability current \mathbf{J}_{tot} (3.21) in these domains for very low values of a .

4.5. Implications

We have shown that for transmission factors below $a \lesssim 10^{-4}$ in intensity hybrids, new effects appear which are not taken into account in a naive, i.e. linear, extrapolation of expectations based on higher-valued transmission factors. We have described the phenomenology of these *quantum sweeper* effects, including the bunching together of low counting rate particles within a very narrow spatial domain, or channel, respectively. However, we also stress that these results are in accordance with standard quantum mechanics, since we just used a re-labelling and re-drawing of the constituent parts of the usual quantum mechanical probability currents. However, concerning the explicit phenomenological appearances due to the nonlinear structure of the probability current in the respective domains for very low values of a , our sub-quantum model is better equipped to deal with these appearances explicitly.

With the discovery of the quantum sweeper effect on the basis of a causal approach to quantum mechanics, we claim to have presented a first example as it was demanded by Rabi⁴. We are optimistic that through further developments, both in theory employing sub-quantum mechanics and in weak measurement techniques capable of probing the latter regime, more unexpected new effects can be predicted and eventually be confirmed in experiment.

4.6. Conclusion and outlook

Summarizing, it has been shown that for transmission factors below $a \lesssim 10^{-4}$ in intensity hybrids, new effects appear which are not taken into account in a naive, i.e. linear, extrapolation of expectations based on higher-valued transmission factors. One describes the phenomenology of these quantum sweeper effects, including the bunching together of low counting rate particles within a very narrow spatial domain. It has also

⁴In his criticism of David Bohm's causal interpretation of the quantum mechanical formalism, Isidor Rabi made the following statement in the 1950ies which is still shared by quite some researchers today: "I do not see how the causal interpretation gives us any line to work on other than the use of the concepts of quantum theory. Every time a concept of quantum theory comes along, you can say yes, it would do the same thing as this in the causal interpretation. But I would like to see a situation where the thing turns around, when you predict something and we say, yes, the quantum theory can do it too." [Fre05]

been stressed that these results are in accordance with standard quantum mechanics, since just a re-labelling and re-drawing of the constituent parts of the usual quantum mechanical probability currents has been used. The reason why the above-mentioned naive expectations are not met is given by the explicit appearance of the nonlinear structure of the probability current in these domains for very low values of a . In this regard, the presented sub-quantum model is better equipped to deal with these appearances explicitly.

5. Numerical methods

In chapters 2 to 4 we have already used numerical methods to produce distribution pictures. We shall here give a detailed explanation on how the results have been computed. As the mathematics of said numerical methods is rather extensive and would thus be misplaced in between the physically oriented explanations of the last chapters, an overview on the procedure of simulation shall be provided here. A quick overview on the simulation setup already provided in chapters 2.2 and 3.1 will be given. Then the practical handling of action and phase will be introduced as well as a note on the usage of diffusion coefficients as an addition to chapter 2.5.

A bigger part will be dedicated to finite difference procedures, especially the two particular ones we used throughout the work, coupled map lattices and the Crank–Nicolson’s method, as well as the respective stability criteria.

We shall present the construction of trajectories whose representation is not quite clear, especially in the sweeper figures of chapter 4. Finally, we shall show how to calibrate our tools by using measurement data of neutron double-slit experiments.

5.1. Preliminaries

5.1.1. The simulation setup

In section 2.2 the setting of a single-slit experiment has been sketched, which has been further extended to at least a double-slit in chapter 3.1 as shown in Fig. 5.1, comprising a three-dimensional problem with slits in the xz -plane elongated in z -direction. Consider a Gaussian entering a slit propagating in the positive y -direction. Its spreading in the xy -plane is essentially independent of the z -position as any spreading into the z -direction is compensated by the spreading of a neighbored plane. For simplicity, we neglect the impact of the slit’s top and bottom edges, thus assuming sufficiently large slits.

The dispersion is assumed to feature an ideal Gaussian shape not being refracted at the slit’s side edges. Furthermore, the Gaussians extends along the whole x -direction, i.e. the Gaussian function is not cut by the slit it runs through, as indicated in Fig. 2.1

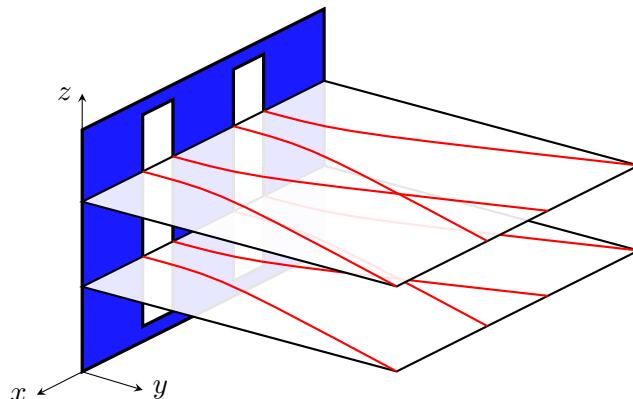


Figure 5.1.: Setting of a double-slit experiment in three dimensions with Bohm-type trajectories sketched on different layers

by the left most shape not cut by the slit. Then, one does not need to consider about phase-free spaces along any light-cone-like structures which would arise otherwise. Right after the slit the initial probability density at a given slit centre position x_0 reads as

$$P(x, 0) = \frac{1}{\sqrt{2\pi}\sigma_0} e^{-(x-x_0)^2/2\sigma_0^2} \quad (5.1)$$

at initial time $t = 0$ and initial standard deviation σ_0 . $P(x, 0)$ (5.1) is the distribution to start with in every single simulation. The connection between the y -axis and time t is given by Eq. (2.1),

$$y(t) = \frac{\hbar k_y t}{m}. \quad (5.2)$$

5.1.2. Action and phase

As soon as more slits are available in a given setup, the phase relations between the distributions after the slits have to be considered. In order to derive the phase relations of coherent beams, we recall the definition of the phase [Mes13]

$$\varphi(x, t) = S(x, t)/\hbar \quad (5.3)$$

with the classical action function $S(x, t)$ as defined in chapter 2.3. We identify the total velocity $v_{\text{tot}}(x, t)$ of Eq. (2.37) along a trajectory with

$$v_{\text{tot}}(x, t) = \frac{\nabla S(x, t)}{m}. \quad (5.4)$$

We assume that there is no potential and the paths described by $v_{\text{tot}}(x, t)$, as sketched in Fig. 2.3, correspond to particle trajectories of free particles and thus the energy is constant, $E = \text{const.}$

These presumptions then lead to the action

$$S(x, t) = \int_{vt}^x mv_{\text{tot}} dx' - \int_0^t E dt' = m \int_{vt}^x \left[v + \frac{u_0^2 t}{\sigma_0^2 + u_0^2 t^2} \xi(t) \right] dx' - \int_0^t E dt' \quad (5.5)$$

with E being the system's total energy and m the mass of the particle involved. According to Fig. 2.5, the lower bound of the integral in Eq. (5.5) is set to vt being the starting point of the diffusion which is different from zero due to velocity v causing an angle of inclination of the incident plane wave. According to the motion in t -direction, there is the constant component $mv_y^2 t$ to be added to $S(x, t)$ in Eq. (5.5) which we put into Et .

As $v = \text{const.}$ as well as $E = \text{const.}$ we can solve both integrals, providing

$$S(x, t) = mvx + \frac{mu_0^2}{2} \left[\frac{\xi(t)}{\sigma(t)} \right]^2 t - mv^2 t - Et. \quad (5.6)$$

In Eq. (5.6), the right most term depends on t only and will cancel out later.

Finally, we write the phase defined by Eq. (5.3) as

$$\varphi(x, t) = \frac{1}{\hbar} \left[mvx + \frac{mu_0^2}{2} \left[\frac{x - vt}{\sigma(t)} \right]^2 t - mv^2 t - Et \right]. \quad (5.7)$$

Expression (5.7) sticks to the coordinate system and will turn out to be very helpful for interference calculations on a grid.

Now, if we extend the setup to a double-slit system, as sketched in Figs. 5.1 or 5.2, we need the Gaussian shaped probability densities coming out from each slit as well as the overall phase which is a combination of the single phases $\varphi(x, t)$ (5.7). Since each Gaussian has its own phase (5.7) we are free to add a phase shifter $\Delta\varphi(x, t)$ for one of the slits of the two-slit experiment, say slit 1, which modifies $\varphi_1(x, t)$ to

$$\varphi'_1(x, t) = \frac{S_1(x, t)}{\hbar} + \Delta\varphi(x, t) \quad (5.8)$$

which yields for the phase difference

$$\begin{aligned} \varphi_{12}(x, t) &= \varphi_2(x, t) - \varphi'_1(x, t) \\ &= \frac{m}{\hbar} \left[v_2(x - x_{02}) - v_1(x - x_{01}) - (v_2^2 - v_1^2)t \right] - \Delta\varphi(x, t) \\ &\quad + \frac{mt}{2\hbar} \left[\frac{u_{02}^2(x - x_{02} - v_2 t)^2}{\sigma_2^2(t)} - \frac{u_{01}^2(x - x_{01} - v_1 t)^2}{\sigma_1^2(t)} \right]. \end{aligned} \quad (5.9)$$

Even though the phase shifter $\Delta\varphi(x, t)$ allows for modification of x and t independently, in this work we only provide simulations with the phase shifter $\Delta\varphi(t)$ being a function of time only, e.g. as is clearly indicated in Fig. (3.12).

5.1.3. The diffusion coefficient in computations

The two slits at positions x_{01} and x_{02} could also have different slit widths and hence different parameters, σ_{01} , $\sigma_1(t)$, u_{01} and σ_{02} , $\sigma_2(t)$, u_{02} , respectively, as sketched in Fig. 5.2. Note, the phase difference φ_{12} (5.9) is at any time defined for the whole domain

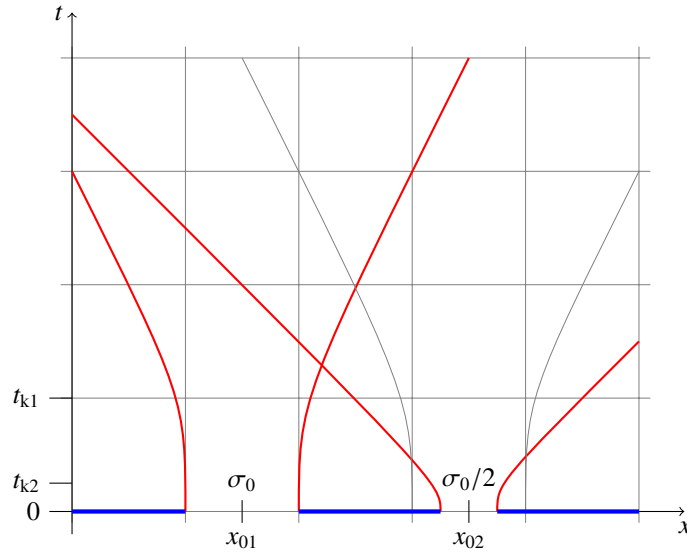


Figure 5.2.: Sketch of a double-slit with two different widths and Bohm-type trajectories (and same-widths scenario indicated by grey lines)

as already pointed out in section 5.1.1.

Now we take a closer look at the time $t = t_k$ of the kink (see Fig. 5.2), i.e. the time when the wave packet changes its spreading behaviour. According to Eq. (2.28),

$$\frac{\sigma(t)}{\sigma_0} = \sqrt{1 + \frac{D^2 t^2}{\sigma_0^4}}, \quad (5.10)$$

this is obviously when the two terms under the square root become of equal value, which yields

$$1 = \frac{D^2 t_k^2}{\sigma_0^4}, \quad (5.11)$$

hence the number under the square root becomes 2, thus we get $\sigma(t_k) = \sqrt{2}\sigma_0$. With the help of Eq. (2.26) we find that

$$D_t = \frac{t}{t_k} D. \quad (5.12)$$

At time $t = t_k$ the diffusion coefficient¹ becomes $D_t = D$. For an exemplary picture, consider the scenario depicted in Fig. 5.2 comprising two slits of different widths. We assume the initial Gaussians passing the slits have a standard deviation according to the respective slit widths, e.g., $\sigma_{01} = \sigma_0$ and $\sigma_{02} = \sigma_0/2$, respectively. The resulting Bohm-type trajectories of the two decaying Gaussians have the properties that the time at the kink quadruples while the spreading only doubles,

$$\sigma_{01} = 2\sigma_{02} \quad \implies \quad t_{k1} = 4t_{k2}, \quad (5.13)$$

t_{ki} being the time at which the kink arises at the respective slit i , as indicated in Fig. 5.2 by red lines compared with the greyed-out lines for the spreading of slit 2 for the case both slits would have standard deviation σ_0 . According to Eq. (2.26), the diffusion coefficients of the two slits, now different from each other and thus indicated by $D_{t,i}$ corresponding to slit i , yield

$$D_{t,1}(t) = \frac{D^2 t}{\sigma_{02}^2} \neq D_{t,2}(t) = \frac{D^2 t}{\sigma_{01}^2}, \quad \forall t > 0, \quad (5.14)$$

which implies that one cannot compute both spread distributions in a single step, as the associated diffusivities evolve different in time. Instead, one has to compute each single probability distribution and combine them afterwards according to Eq. (3.14).

As an example of a double-slit setup with different slit widths which considers also Eqs. (5.9) and (5.14) in comparison to a double-slit experiment with equal widths. [Grö12b; Mes13]

The graphical results providing the interference patterns thereto are shown in Fig. 5.3. In Fig. 5.3(a) the maximum of the intensity is distributed along the symmetry line exactly in the middle between the two slits, as well as in Fig. 5.3(b), though slit 2 has doubled width. In the exemplary figures, trajectories according to Eq. (3.14) for the two Gaussian slits are shown. For an explanation on the meaning of these patterns, see chapter 3.3.

¹Note that the diffusivity $D = \hbar/2m$ is constant for all times t and has to be distinguished from the diffusion coefficient D_t . See also section 2.5

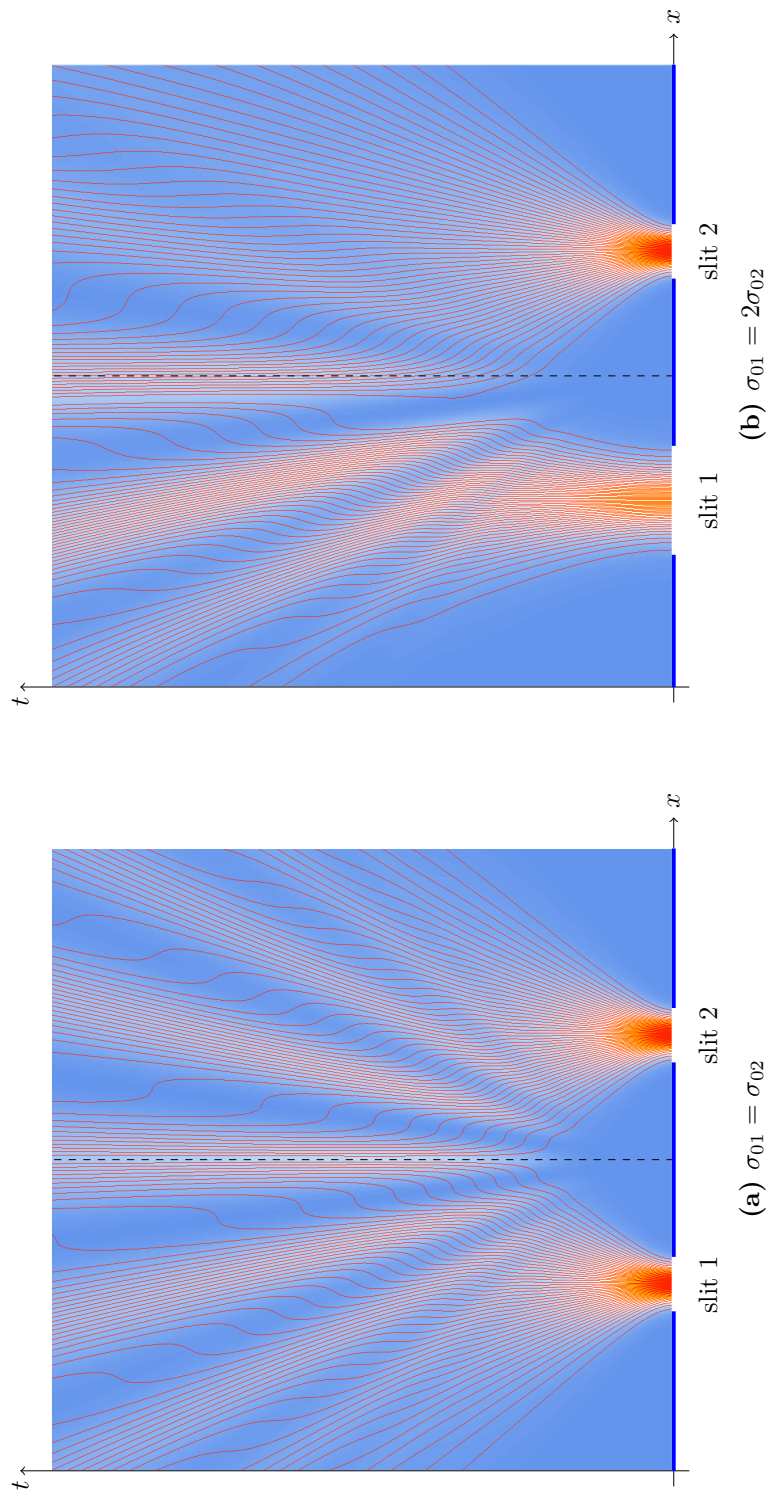


Figure 5.3.: Classical computer simulation of the interference pattern with different slit widths: intensity distribution with increasing intensity from white through yellow and orange, with trajectories (red) for two Gaussian slits, and with large dispersion (evolution from bottom to top; $v_{x,1} = v_{x,2} = 0$).

5.2. The finite difference method

In section 2.5 we have formulated the ballistic diffusion equation (2.25),

$$\frac{\partial P}{\partial t} = \underbrace{\frac{D^2 t}{\sigma_0^2}}_{D_t} \frac{\partial^2 P}{\partial x^2}, \quad (5.15)$$

with diffusion constant $D = \hbar/2m$. Eq. (5.15) is valid per slit of width σ_0 . In a multi-slit system Eq. (5.15) has to be evaluated once per slit and combined with phases (5.9).

In this section we describe the evaluation procedure of $P(x, t)$ in order to solve Eq. (5.15) with initial value $P(x, 0)$ given by Eq. (5.1) by means of finite difference methods (FDM). FDMs are numerical methods for solving differential equations by approximation with difference equations. Here, the ballistic diffusion equation (5.15) is solved per slit on a discretised grid. As first relations, we define

$$t = T \Delta t, \quad x = X \Delta x, \quad (5.16)$$

with t and x denoting time and position in the physical domain while T and X denote time and position of the simulation domain, respectively. Then we have for the step widths

$$\Delta t = \frac{t}{T}, \quad \Delta x = \frac{x}{X}, \quad (5.17)$$

thereby defining the scaling between the physical domain and the numerical discretisation.

Now, we take a closer look at two different numerical procedures to solve Eq. (5.15) and the stability conditions of these procedures.

5.2.1. Coupled map lattices

Coupled map lattices, or short CML, are equivalent to cellular automata, though each cell² is represented by real values instead of integers (see Fig. 5.4). CMLs allow to inquire into dynamical processes of emergent processes and could model not only general phenomenological aspects of our world but also directly the laws of physics themselves. CMLs then could be a powerful tool to get a deeper understanding on what is going on because they are information-preserving and thus retain one of the most fundamental features of microscopic physics – namely reversibility. [TM87]

²We shall use the terms “cell” and “node” synonymously. However, for CMLs or cellular automata the term cell is more common which is associated with the idea of a space filled with some entities.

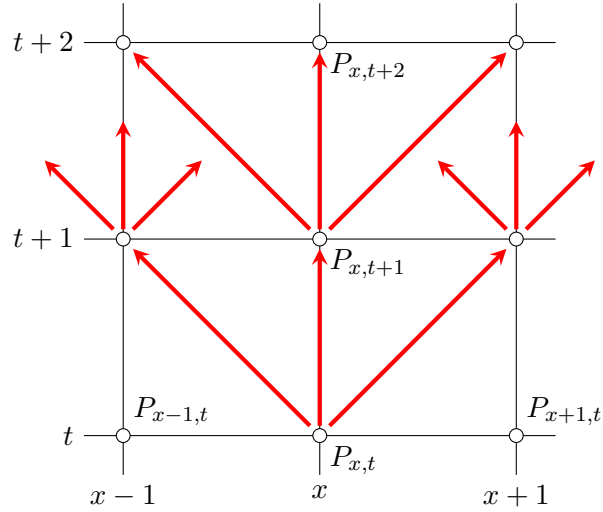


Figure 5.4.: Neighbourhood in coupled map lattices

Coupled map lattices reduce macroscopic phenomena to precisely defined microscopic processes which make them of prime methodological interest, but in order to obtain such features, in general one has no choice but to implement an explicit finite difference forward scheme, a so-called *Euler scheme*, respectively.

An explicit *forward* scheme is characterized by the fact that solely solutions of already elapsed time steps are sufficient to calculate the solution of the next time step. In a coupled map lattice, then, all values of the next time step of the whole domain are computable within a single iteration only out of values already calculated before. The crucial point of this definition is that these upcoming values are *computable* in the same iteration, these values must therefore not be part of a condition that is itself subject to be solved before, otherwise the scheme were *implicit*. In this sense coupled map lattices are completely specified, discrete dynamical systems of a local relation, i.e. neighbourhood rules, as is the case for continuous dynamical systems defined by partial differential equations. And hence coupled map lattices are the discrete physicist's concept of *fields*.

In order to derive the coupled map lattices' relations we replace the differential terms

of Eq. (5.15) by discrete differences,³

$$\frac{\partial P}{\partial t} \rightarrow \frac{P_{x,t+1} - P_{x,t}}{\Delta t} + O(\Delta t^2), \quad (5.18)$$

$$\frac{\partial^2 P}{\partial x^2} \rightarrow \frac{P_{x+1,t} - 2P_{x,t} + P_{x-1,t}}{\Delta x^2} + O(\Delta x^2), \quad (5.19)$$

using two-dimensional cells $P_{x,t}$ for each value $P(x,t)$ on a discrete lattice. Δx and Δt being the step width in space and time, respectively. The Landau notation O describes the limiting behaviour of the functions, both of which are here of order 2.

The resulting finite difference equation is obtained by simply substituting Eqs. (5.18) and (5.19) into (5.15), thereby omitting the Landau notation O ,

$$\frac{P_{x,t+1} - P_{x,t}}{\Delta t} = \frac{D_{x,t+1}}{\Delta x^2} \left(P_{x+1,t} - 2P_{x,t} + P_{x-1,t} \right), \quad (5.20)$$

and in case $D_t(x,t)$, or its pendant on the lattice $D_{x,t}$, is independent of x , then, after reordering the equation reads as

$$P_{x,t+1} = P_{x,t} + \frac{D_{t+1}\Delta t}{\Delta x^2} \left(P_{x+1,t} - 2P_{x,t} + P_{x-1,t} \right) \quad (5.21)$$

with spatial variable x , time t , and initial Gaussian distribution $P(x,0)$ having standard deviation σ_0 at $t = 0$. The calculation of a cell's value $P_{x,t+1}$ (at time $t + \Delta t$) only depends on cell values at the previous time step t , which fulfils the necessary condition for coupled map lattices as stated above. In Eq. (5.21) the time-dependent diffusion coefficient D_{t+1} can be calculated without any knowledge of neighbouring cells because it only depends on time. As this diffusion coefficient represents the underlying physical process at a given cell it is calculated in Eq. (5.21) for the evaluated time step $t + \Delta t$ at which $P_{x,t+1}$ is evaluated, hence D_{t+1} instead of D_t .

Concerning the neighbourhood rules as local relations, a cell's value affects only itself and its direct neighbours in the next time step thereby defining a light-cone-like 45° line in the unity-sized grid of the coupled map lattice as shown in Fig. 5.4. However, this is an impact of the construction of derivatives in the finite different scheme as is obvious from Eqs. (5.18) and (5.19).

³To make things easily readable and taking into account that the indexed variables are only used in this chapter, we leave the naming of the variables untouched, even though the indexed variables define a grid comprising only natural number, i.e. $x, t \in \mathbb{N}$, whereas non-index variables represent physical quantities. In this chapter let us define: A variable being an index (\cdot_x, \cdot_t) pertains to the grid, else (x,t) it represents a physical quantity.

Stability of coupled map lattices

The solutions of finite difference schemes may provide instabilities which are related to high-frequency oscillations. Instability is essentially a local phenomenon as at the points where the oscillations arise the derivative of the solution is discontinuous. Even though, the oscillations caused by the instability propagate to other regions, which can eventually make the disturbance seem to be global in extent. Here, we examine the conditions to be taken into consideration under which and when the system is stable.

The stability condition for the scheme (5.21) is that

$$\left| \frac{D_t \Delta t}{\Delta x^2} \right| \leq \frac{1}{2} \quad (5.22)$$

be satisfied for all values of the cells in the domain of computation. The general procedure is that one considers each of the *frozen coefficient problems* arising from the scheme. The frozen coefficient problems are the constant coefficient problems obtained by fixing the coefficients at their values attained at each point in the domain of the computation (cf. Strikwerda [Str04]).

To fix the coefficients in Eq. (5.22) the variables Δx and Δt are kept constant during the whole computation, whereas the value of $D_t(t)$ grows with increasing time. In order to obtain the best possible estimate with Eq. (5.22) we substitute the maximum possible value of D_{t+1} , i.e.

$$D_t(t) \rightarrow \max(D_{t+1}) = D_{t_{\max}+1} \quad (5.23)$$

to be kept up for the sake of derivation of the stability conditions only.

Substituting $D_t(t)$ of Eq. (5.15) into (5.22) leads to

$$\Delta t \leq \frac{\Delta x^2 \sigma_0^2}{2D^2 t} \quad (5.24)$$

which reaches its minimum value in the domain at $t = t_{\max}$, thereby defining the largest allowed step width Δt_{\max} to ensure stability. Using these limits, i.e. $t_{\max} = T_{\max} \Delta t_{\max}$, yields

$$\Delta t_{\max} \leq \frac{\Delta x^2 \sigma_0^2}{2D^2 t_{\max}} = \frac{\Delta x^2 \sigma_0^2}{2D^2 T_{\max} \Delta t_{\max}}, \quad (5.25)$$

$$\Delta t_{\max}^2 \leq \frac{\Delta x^2 \sigma_0^2}{2D^2 T_{\max}}, \quad (5.26)$$

and eventually leads to the *stability condition*

$$\Delta t_{\max} \leq \frac{\Delta x \sigma_0}{D \sqrt{2T_{\max}}}. \quad (5.27)$$

While the numerator's variables, Δx and σ_0 , are solely determined by the setup in x -direction, the denominator's variables, $D = \hbar/2m = \text{const.}$ and T_{\max} , the latter is solely determined by the t -direction. If, for example, one extends the time development, i.e. by setting

$$T_{\max} \rightarrow aT_{\max}, \quad a > 1, \quad (5.28)$$

one then has to shrink

$$\Delta t_{\max} \rightarrow \Delta t_{\max}/\sqrt{a} \quad (5.29)$$

simultaneously to ensure stability.

The stability condition (5.27) turns out to be a problematic restriction on computability. However, in cases with moderate spreading we obtain pretty good results and proved the method of coupled map lattices to work fine. Nevertheless, coupled map lattices demand explicit methods, as already stated above. As there are also examples in this thesis where this method does not work economically usefully, we then must employ other methods (see chapter 5.2.2).

Finally, we want to point out that, in cases where coupled map lattices are stable, the approximation follows the exact solution at least linearly with x and t . The complete proves can be found in textbooks, e.g. from Toffoli *et al.* [TM87], Schwarz and Köckler [SK09], or Haas [Haa99].

5.2.2. Crank–Nicolson's method

Now we investigate Crank–Nicolson's method as an example of an *implicit* method. From the viewpoint of the difference approximation the disadvantage with the derivative of an explicit method is that the used difference quotients approximate their associated derivatives at different positions of the domain. In order to enhance the approximations the second derivative is replaced in the following way: Instead of using rule (5.19) we approximate $\partial^2 P/\partial x^2$ by the arithmetic mean of the two difference quotients at nodes $[x, t]$ and $[x, t + 1]$ at two consecutive time steps, as shown in Fig. 5.5, and obtain for the approximations⁴ with respect to M [SK09]

$$\frac{\partial^2 P}{\partial x^2} = \frac{P_{x+1,t} - 2P_{x,t} + P_{x-1,t}}{2\Delta x^2} + \frac{P_{x+1,t+1} - 2P_{x,t+1} + P_{x-1,t+1}}{2\Delta x^2} + O(\Delta x^2), \quad (5.30)$$

$$\frac{\partial P}{\partial t} = \frac{P_{x,t+1} - P_{x,t}}{\Delta t} + O(\Delta t^2). \quad (5.31)$$

⁴We repeat here the statement of footnote 3 on page 88

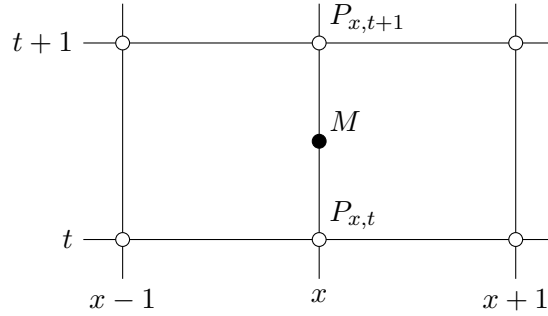


Figure 5.5.: Lattice according to Crank–Nicolson’s method

The limiting behaviour of each function is of order 2 as indicated by the Landau notation O . As D_t is independent of x , the resulting finite difference equation is obtained by substitution of Eqs. (5.30) and (5.31) into (5.15), thereby omitting the Landau notation O , which reads after reordering as

$$\begin{aligned}
 & -d_t P_{x-1,t+1} + (2 + 2d_t) P_{x,t+1} - d_t P_{x+1,t+1} \\
 = & d_t P_{x-1,t} + (2 - 2d_t) P_{x,t} - d_t P_{x+1,t}
 \end{aligned} \tag{5.32}$$

with

$$d_t := \frac{D_t \Delta t}{\Delta x^2} \tag{5.33}$$

thereby assuming the value

$$D_t := D_{t+1/2} = D_t(t + \Delta t/2) \tag{5.34}$$

at M .

A quick look at Eq. (5.32) illuminates why the scheme is implicit: The values of the next time step cannot be calculated directly out of the former ones. Instead, a linear equation system has first to be solved to obtain the solution. In comparison with coupled map lattice, then, one has to put more effort into computer programs.

Stability of Crank-Nicolson's method

We set d_t (5.33) being constant in a first step, i.e. $d_t \rightarrow d$, and rewrite Eq. (5.32) as

$$\begin{aligned}
 & \begin{pmatrix} 2+2d & -d & & & \\ -d & 2+2d & -d & & \\ \ddots & \ddots & \ddots & & \\ & -d & 2+2d & -d & \\ & & -2d & 2+2d & \end{pmatrix} \mathbf{p}_{t+1} \\
 = & \begin{pmatrix} 2-2d & d & & & \\ d & 2-2d & d & & \\ \ddots & \ddots & \ddots & & \\ & d & 2-2d & d & \\ & & 2d & 2-2d & \end{pmatrix} \mathbf{p}_t
 \end{aligned} \tag{5.35}$$

or short

$$(2\mathbf{I} + d\mathbf{J})\mathbf{p}_{t+1} = (2\mathbf{I} - d\mathbf{J})\mathbf{p}_t \tag{5.36}$$

with \mathbf{I} being the identity matrix and

$$\mathbf{J} := \begin{pmatrix} 2 & -1 & & & \\ -1 & 2 & -1 & & \\ & -1 & 2 & -1 & \\ & & \ddots & \ddots & \ddots \\ & & & -1 & 2 & -1 \\ & & & & -2 & 2 \end{pmatrix} \in \mathbb{R}^{n,n}, \tag{5.37}$$

$$\mathbf{p}_t := \begin{pmatrix} P_{1,t} \\ P_{2,t} \\ P_{3,t} \\ \vdots \\ P_{n-1,t} \\ P_{n,t} \end{pmatrix} \tag{5.38}$$

with n being the number of nodes in x -direction. Because of $d > 0$ the matrix $(2\mathbf{I} + d\mathbf{J})$ is diagonal dominant and regular, thus we obtain formally

$$\mathbf{p}_{t+1} = (2\mathbf{I} + d\mathbf{J})^{-1}(2\mathbf{I} - d\mathbf{J})\mathbf{p}_t. \tag{5.39}$$

This method is absolutely stable if the absolute values of the eigenvalues λ_i of the matrix $(2\mathbf{I} + d\mathbf{J})^{-1}(2\mathbf{I} - d\mathbf{J})$ are less than one. Because of the form of \mathbf{J} the eigenvalues μ_i are real and $0 < \mu_i < 4$ [SK09] and hence

$$-1 < \lambda_i = \frac{2 - d\mu_i}{2 + d\mu_i} < 1. \quad (5.40)$$

This proves Crank–Nicolson’s method absolutely stable because the value d is not restricted. For we allow any positive values for D_t and hence any arbitrary values $d \rightarrow d_t = D_t \Delta t / (\Delta x)^2$ (5.33) without loss of stability.

The approximation follows the exact solution at least with $O(\Delta x^2)$ and $O(\Delta t^2)$, respectively, and converges thus 10 times faster than coupled map lattices. However, the iteration steps must not be chosen too big because, though stability is given, the approximation error increases $\propto O(\Delta x^2 + \Delta t^2)$. The proves can be found in textbooks, e.g. from Toffoli *et al.* [TM87], Schwarz and Köckler [SK09], or Haas [Haa99].

5.2.3. Comparison of the finite difference schemes

We compared two finite difference schemes and provided a short overview on advantages and restrictions in both cases. The coupled map lattices, as an example of an explicit scheme (5.21), has its most advantageous feature definitely in its quick and easy implementation at the cost of problematic restrictions on the step width. For the Crank–Nicolson method, as an example of an implicit scheme (5.32), the implementation task is rather on the expensive side because of the equations solvers needed for, while its advantage lies in its convergence behaviour for any step width. For an overview see Tab. (5.1).

Scheme	Stable	Error	Comment
Coupled map lattices	$\Delta t_{\max} \leq \frac{\Delta x \sigma_0}{D \sqrt{2T_{\max}}}$	$O(\Delta x + \Delta t)$	easy to implement
Crank–Nicolson	yes	$O(\Delta x^2 + \Delta t^2)$	converges always

Table 5.1.: Overview on the two compared finite difference schemes.

For our simulations within this thesis we employed both coupled map lattices as well as Crank–Nicolson’s method. For both of which we developed on a standard personal

computer using *Scilab* [Cam10] and recently also *Julia language* [Bez14], two open source packets for numerical computation.

5.3. The simulation procedure

The simulation procedure, which is schematically shown in Fig. 5.6, comprises the following steps to simulate solutions according to the ballistic diffusion equation (2.25):

1. Define an initial probability distribution P as in Eq. (5.1),
2. Compute the spreading: (5.21) or (5.32),
3. Calculate the associated phase φ according to Eqs. (5.5) and (5.8)
4. Combine to
 - a) either a total probability distribution (3.14),
 - b) or a total probability current (3.21).

Accordingly, with this procedure we simulate intensity probabilities as well as current distributions.

5.4. Trajectories

If one considers a particle as a walker obeying a Brownian-type motion including the zitterbewegung, then the resulting trajectory would be erratic and thus of little usefulness for the purpose of repeated experiments (see section 2.2 for further explanation). Therefore, the particle's trajectories in the pictures within this thesis are the results of averaging of a huge number of such walkers, in the mean obeying a Bohmian-type trajectory which is sufficiently smooth to explain repeated experiments then. The emerging trajectories are in full accordance with those obtained from the Bohmian approach, as can be seen by comparison with references [BH93; Dav15; dGos16; Hol93; SB09; SM12], for example.

Accordingly, trajectories of Bohmian-type are shown, which are always computed from the underlying probability distribution P . On some occasions the distances between two single, adjacent trajectories differ for didactic reasons,

- as in Fig. 2.6, for example, where each two single trajectories are chosen equally spaced, and hence the trajectories are initially equidistant,

- as in Fig. 5.3, for example, where the flux, i.e. every value ΔP , between any two adjacent trajectories is equal and kept constant, hence the trajectories reach their highest density around the maximum of the intensity distribution.

While the former method of displaying trajectories is mostly used for comparison reasons with older pictures in literature, the latter one gives a better idea of properties.

In most of the pictures the same number of trajectories for each Gaussian is used thereby resulting in well proportioned figures as long as the distributions possess about the same intensities. However, if the relation of the intensities differ considerable, this easy recipe fails. For example, in figures in chapter 4 the number of trajectories are chosen to be equal for each slit thereby resulting in sweeper effects comprising trajectories that do not provide the correct physical proportions: Thus, if one maintained the trajectories of said sweeper-figures to enclose the same amount of flux for both beams at the same time, and thus for the whole picture, then either the low-intensity beam had no visible trajectories or the high-intensity beam had too many trajectories so that one couldn't distinguish between the single lines.

5.5. Calibrating the simulation tools

The double-slit experiment is of particular interest and therefore there is a bunch of measured data available. In an actual experiment as sketched in Fig. 5.7, the double-slit diffraction of neutrons has been measured [RW00; Zei88]. The typical wavelength used is $\lambda = 1.845 \text{ nm}$. The Gaussian slit width is $21.9 \mu\text{m}$ and $22.5 \mu\text{m}$, respectively with their centres being $126.3 \mu\text{m}$ apart, and the intensity distributions are recorded on a screen S_4 located in the forward direction at a distance of 5 m from the object slit S_5 .

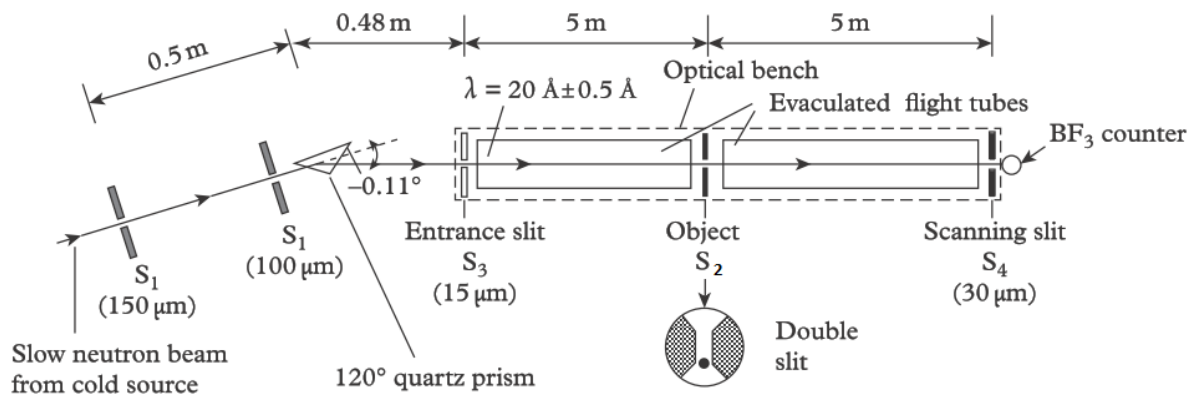


Figure 5.7.: Experimental setup. From [RW15; Zei88]

In Fig. 5.8 we show the results of our computer simulations for the probability density distributions of a neutron beam using the parameters of this experiment.

Comparing these simulations' results with actual measurement data in Rauch and Werner [RW00] as well as from Zeilinger et al. [Zei88] enabled us to adjust the parameters. It turned out that there is a certain ratio between the slit width and σ_0 to be maintained that is around

$$\sigma_0 \approx \frac{\text{slit width}}{3} \quad (5.41)$$

such that the correct shape of the intensity recorded at $y = 5$ m can be ensured.

Even though the curves do not perfectly fit, the result is sufficiently accurate, taking into account, that the actual measurement did not have taken place with idealized Gaussians but with real neutron beams. Zeilinger et al. [Zei88] carried out in their paper how they compared the measured data with theory. In fact, they integrated of course the whole length of the optical bench, i.e. in Fig. 5.7 this corresponds to the paths from S_3 to S_4 . In our model this is not possible as we do not yet allow objects in the path. Thus, our path contains the second half of the optical bench, i.e. in Fig. 5.7 corresponding to the paths from S_2 to S_4 , thereby assuming an idealized Gaussian behind S_5 . The scope of this thesis is to simulate a Gaussian beam in one dimension without diffraction, therefore, modelling diffracted Gaussians would need further investigation.

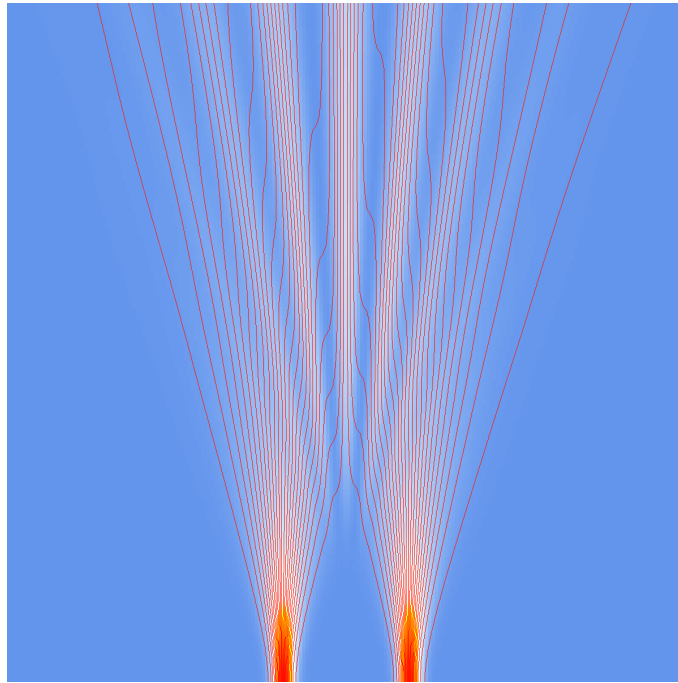
5.6. Conclusions and outlook

In this chapter, the simulation means for obtaining probability distributions as well as density currents has been provided. Preliminarily, the setup, the phase conditions and the diffusion coefficient for different slit widths has been discussed.

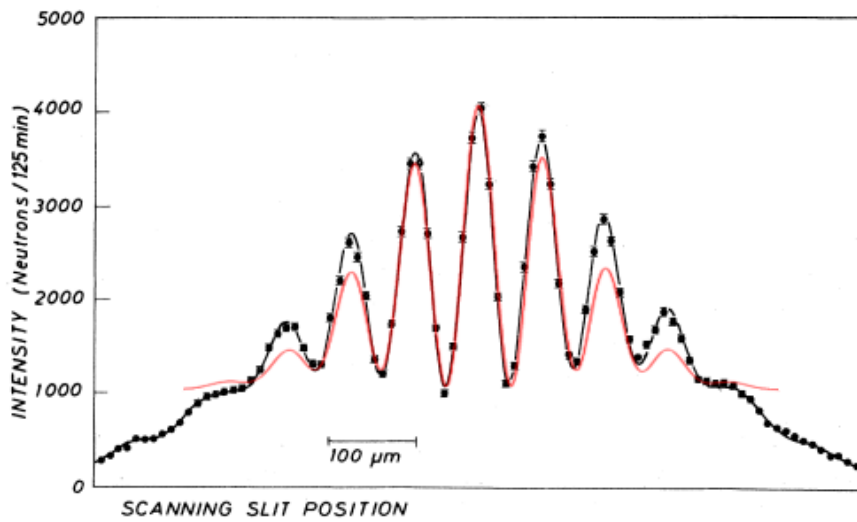
As a numerical means to solve the ballistic diffusion equation two finite different schemes have been introduced. The first one, coupled map lattices as an example for an explicit scheme has been shown to be beneficial for exploration of the dynamical behaviour bringing in the advantage of easy implementation. The second one, the implicit scheme of Crank–Nicolson has been proven to be unconditionally stable for the cost of much more computational effort, however, it allows obtaining solutions independent of the domain even in situations where coupled map lattices collapse.

The method of constructing trajectories which are part of the numerical procedure, has been explained.

Finally, a calibration procedure has been provided: The comparison of measured results from a neutron-experiment with simulated results of the same setup has yielded the relation between the slit width and the initial half-width of the Gaussian σ_0 .



(a) Probability distribution



(b) Intensity recorded at $y = 5$ m comprising the measured curve (black) from [Zei88], and the simulation's result (red)

Figure 5.8.: Classical computer simulation of the interference pattern for $\lambda = 1.8$ nm, the slit width is $22 \mu\text{m}$ each, with their centres being $200 \mu\text{m}$ apart

A. Classical mechanics and Boltzmann's relation

The equations of mechanics can be deduced from a least action principle, where usually the varied path in configuration space always terminates at end points representing the system configuration at the same times, t_0 and t_1 , as the natural path.

In the following one starts with the derivation of a less constrained δ -variation with a varied path over which an integral is evaluated that may end at other times than the natural path, and there may be a variation in the coordinates at the end points. By defining a relation between heat and mechanical work one follows the thoughts of Brillouin [Bri64, Chapter 11], and to some extent of Goldstein [Gol02], Scheck [Sch10], Hamel [Ham67, pp.312-314], and Hand [HF98, pp.230ff] leading directly to the Boltzmann relation of periodic motion.

A.1. The principle of least action

We consider a general problem with time-dependent holonomic constraints. With kinetic energy T , potential energy V , time t , generalized coordinates q^k and velocities \dot{q}^k , $k = 1, \dots, r$ (r being the remaining coordinates), we form then the Lagrangian function

$$L(q^k, \dot{q}^k, t) = T(q^k, \dot{q}^k, t) - V(q^k, t). \quad (\text{A.1})$$

We have further the momentum p_k conjugate to the coordinate q^k given by

$$p_k = \frac{\partial T}{\partial \dot{q}^k} = \frac{\partial L}{\partial \dot{q}^k}, \quad (\text{A.2})$$

and Lagrange's equation takes the form

$$\frac{dp_k}{dt} = \frac{\partial L}{\partial q^k}. \quad (\text{A.3})$$

We will study the value of the action integral

$$S = \int L dt \quad (\text{A.4})$$

during the evolution of the system.

For the δ -variation the varied path always terminates at end points representing the system configuration at the same times, t_0 and t_1 , as the natural path. To obtain Lagrange's equations of motion, it is also required that the varied path returns to the same end points in configuration space, i.e. $\delta q^k(t_0) = \delta q^k(t_1) = 0$. [Bri64; Gol02]

Now, we define a less constrained δ -variation (note the bold δ -symbol) according to Fig. A.1 with a varied path over which an integral is evaluated that may end at other times than the natural path, i.e. the paths have different throughput times, and there may be an additional variation in the coordinates at the end points.

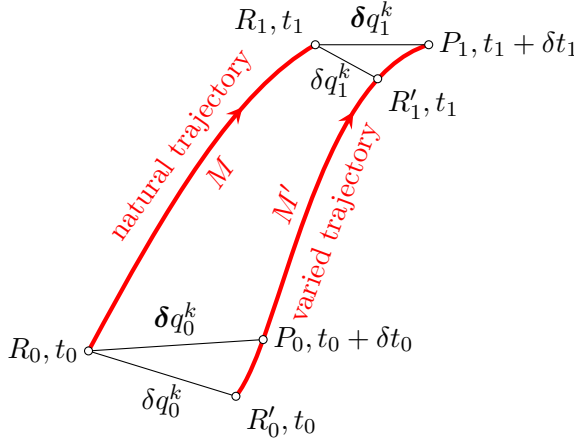


Figure A.1.: The δ -variation in configuration space, composed of a variation in space, δq^k , and, additionally, of a variation in time, δt .

As shown in Fig. A.1 the two usual variations, δq^k in space and δt in time, lead to the δ -variation of the space variable by the relation

$$\delta q^k = \delta q^k + (\dot{q}^k + \delta \dot{q}^k) \delta t \approx \delta q^k + \dot{q}^k \delta t \quad (\text{A.5})$$

with negligible second order correction $\delta \dot{q}^k \delta t$. The variation of action integral S , i.e.

$$\delta S = \delta \int_{t_0}^{t_1} L dt, \quad (\text{A.6})$$

is the difference of the action of the natural trajectory M from R_0 to R_1 and the action of the varied trajectory M' from R_0 to R_1 . Thus we can rewrite Eq. (A.6) as

$$\delta S = \int_{t_0 + \delta t_0}^{t_1 + \delta t_1} L(q^k + \delta q^k) dt - \int_{t_0}^{t_1} L(q^k) dt \quad (\text{A.7})$$

with the Lagrangian function L along the varied trajectory in the first integral and L along the natural trajectory in the second integral. We separate the integration over the terminal segments R'_0P_0 and R'_1P_1 and obtain

$$\begin{aligned}\delta S &= \underbrace{L(q_1^k + \delta q_1^k)\delta t_1}_{Q'_1P_1} - \underbrace{L(q_0^k + \delta q_0^k)\delta t_0}_{Q'_0P_0} + \underbrace{\int_{t_0}^{t_1} L(q^k + \delta q^k) dt}_{M'} - \underbrace{\int_{t_0}^{t_1} L(q^k) dt}_M \\ &= L(q_1^k + \delta q_1^k)\delta t_1 - L(q_0^k + \delta q_0^k)\delta t_0 + \int_{t_0}^{t_1} \delta L dt.\end{aligned}\quad (\text{A.8})$$

Here the variation in the last integral can be carried out through a parametrization of the varied path,

$$\delta L = L(q^k + \delta q^k) - L(q^k) = \sum_k \left(\frac{\partial L}{\partial q^k} \delta q^k + \frac{\partial L}{\partial \dot{q}^k} \delta \dot{q}^k + \frac{\partial L}{\partial t} \delta t \right), \quad (\text{A.9})$$

where the last term in the bracket vanishes because we have chosen two simultaneous positions and hence $\delta t = 0$. We integrate the second term by parts, using the exchange relation $\delta \left(\frac{d}{dt} \right) = \frac{d}{dt} (\delta \cdot)$ for \dot{q}^k and obtain

$$\frac{\partial L}{\partial \dot{q}^k} \frac{d}{dt} (\delta q^k) = \frac{d}{dt} \left(\frac{\partial L}{\partial \dot{q}^k} \delta q^k \right) - \delta q^k \frac{d}{dt} \left(\frac{\partial L}{\partial \dot{q}^k} \right). \quad (\text{A.10})$$

Substitution of these expressions into Eq. (A.9) leads to

$$\int_{t_0}^{t_1} \delta L dt = \int_{t_0}^{t_1} \sum_k \left[\frac{\partial L}{\partial q^k} - \frac{d}{dt} \left(\frac{\partial L}{\partial \dot{q}^k} \right) \right] \delta q^k dt + \sum_k \frac{\partial L}{\partial \dot{q}^k} \delta q^k \Big|_{R_0}^{R_1}. \quad (\text{A.11})$$

On account of Eqs. (A.2) and (A.3), the equation within the square brackets of the integral disappears entirely. Now we substitute Eqs. (A.9) and (A.11) into (A.8) and find

$$\delta S = \left[L(q_1^k) + \delta L \right] \delta t_1 - \left[L(q_0^k) + \delta L \right] \delta t_0 + \sum_k \frac{\partial L}{\partial \dot{q}^k} (\delta q^k - \dot{q}^k \delta t) \Big|_{R_0}^{R_1}. \quad (\text{A.12})$$

We identify $L(q_i^k) = L_i$, neglect the second order terms and reorder to find our final result as

$$\delta S = H_0 \delta t_0 - H_1 \delta t_1 - \sum_k p_{0k} \delta q_0^k + \sum_k p_{1k} \delta q_1^k. \quad (\text{A.13})$$

Here, we substituted Eq. (A.2) and introduced the Hamiltonian

$$H_i = \sum_k p_{ik} \dot{q}_i^k - L(q_i^k, \dot{q}_i^k, t_i). \quad (\text{A.14})$$

A.1.1. The conservative case

Along with the integral S defined in Eq. (A.4) we shall consider the *abbreviated action*

$$F = 2 \int T dt = \int \sum_k p_k \dot{q}^k dt = \int \sum_k p_k dq^k. \quad (\text{A.15})$$

Taking into account

$$H = \sum_k p_k \dot{q}^k - L = 2T - L = T + V = E. \quad (\text{A.16})$$

For conservative systems the total energy E remains constant, $H_0 = H_1 = E$, and from (A.13) we find

$$\delta S = E(\delta t_0 - \delta t_1) - \sum_k p_{0k} \delta q_0^k + \sum_k p_{1k} \delta q_1^k. \quad (\text{A.17})$$

We reconsider Eq. (A.4) and set up the equation connecting F with action S by

$$S = \int L dt = \int (T - V) dt = \int (2T - E) dt = F - \int E dt. \quad (\text{A.18})$$

We compare the values of the integrals F taken along two neighbouring trajectories, the natural and a nearby entirely arbitrary trajectory. On the natural trajectory, the total energy E remains constant, but this is not so on the varied trajectory. We obtain then

$$\delta F = \delta S + \delta \int E dt = \delta S + \int \delta E dt + E(\delta t_1 - \delta t_0), \quad (\text{A.19})$$

where the last term in (A.19) is an expression for the variation at the endpoints of the trajectory from 0 to 1. Substitution of Eq. (A.17) into (A.19) yields

$$\delta F = \int \delta E dt + \sum_k p_{1k} \delta q_1^k - \sum_k p_{0k} \delta q_0^k \quad (\text{A.20})$$

as a general result. A nearby trajectory, although entirely arbitrary, is only subject to the conditions of respecting constraints [Bri64; Ham67]. Now, we investigate the influence of a modification of such constraints.

A.1.2. Reduced constraints

We consider, again, a system of N mass points defined by their $3N$ position coordinates. We further suppose that there exist l holonomic constraints among these points so that there remains only

$$r = 3N - l \quad (\text{A.21})$$

independent degrees of freedom. We assume a conservative system characterized by time-independent holonomic constraints, hence we can define a total energy E remaining constant in time during the natural evolution of the system.

We find

$$E = T + V = \text{const.}, \quad L = T - V = 2T - E \quad (\text{A.22})$$

for the natural motion of the conservative system, the usual Lagrangian L referring only to the visible coordinates q^1, \dots, q^r . Now, we allow for a variation of constraints and we will use the asterisk $*$ to indicate the overall quantities containing the independent coordinates $q^{r+1}, q^{r+2}, \dots, q^{3N}$. So as not to give useless complication to the equations, we take it, that the forces guaranteeing the constraints are derived from a potential energy V^* by

$$V^* = \sum_{k=r+1}^{3N} A_k (q^k)^2 \quad (\text{A.23})$$

with very large positive coefficients A_k thereby guaranteeing very small q^k s. This form corresponds to the hypothesis that the constraints are realized by very rigid elastic systems. A small displacement q^k brings into action a very great force $-2A_k q^k$ which opposes this change. The coordinates $q^{r+1}, q^{r+2}, \dots, q^{3N}$ then remain practically constant, their corresponding velocities \dot{q}^k vanish; the corresponding momenta p_k however will not always vanish due to their dependence on \dot{q}_i^k , $i = 1, \dots, l = 3N - r$.

The kinetic energy T is unchanged in the natural motion, for, all the velocities $q^{r+1}, q^{r+2}, \dots, q^{3N}$ of the hidden coordinates are practically constant (and zero) for this trajectory and hence $p_k \dot{q}^k \approx 0$ for $k = r + 1, \dots, 2N$. With these definitions we find the total energy as

$$E^* = E + V^*, \quad (\text{A.24})$$

including a new term coming from the new potential energy V^* . The complete Lagrangian function reads

$$L^* = T - V - V^* = L - V^* \quad (\text{A.25})$$

with L being the usual Lagrangian referring only to the visible coordinates q^1, \dots, q^r . Note that E^* and L^* in Eqs. (A.24) and (A.25) are related to the natural trajectory.

On a varied trajectory, the kinetic energy T^* changes. In this case we write

$$2T^* = 2T + \sum_{k=r+1}^{3N} p_k \dot{q}^k, \quad (\text{A.26})$$

and

$$F^* = F + \sum_{k=r+1}^{3N} \int p_k \dot{q}^k dt = F + \sum_{k=r+1}^{3N} \int p_k dq^k. \quad (\text{A.27})$$

We can thus apply Eq. (A.20) to our system with the quantities marked with asterisks and we obtain

$$\delta F^* = \int \delta E^* dt + \sum_{k=1}^{3N} p_{1k} \delta q_1^k - \sum_{k=1}^{3N} p_{0k} \delta q_0^k, \quad (\text{A.28})$$

indicating visible and hidden coordinates, whereas Eq. (A.20) contained only the r visible coordinates. Equation (A.15) must also hold for the constraints, thus

$$\delta F^* = \delta \int 2T^* dt = \delta F + \delta \int \sum_{k=r+1}^{3N} p_k dq^k = \delta F + \int \delta \sum_{k=r+1}^{3N} p_k dq^k + \sum_{k=r+1}^{3N} p_k \delta q^k \Big|_0^1. \quad (\text{A.29})$$

Returning now to the quantities without asterisks we get by substituting Eq. (A.29) into (A.28) that

$$\delta F = \int \left(\delta E + \delta V^* - \delta \sum_{k=r+1}^{3N} p_k \dot{q}^k \right) dt + \sum_{k=1}^r p_{1k} \delta q_1^k - \sum_{k=1}^r p_{0k} \delta q_0^k \quad (\text{A.30})$$

because the term $\sum_{k=r+1}^{3N} p_{1k} \delta q_1^k - \sum_{k=r+1}^{3N} p_{0k} \delta q_0^k$ cancels.

A.2. A thermodynamical analogy

To carve out the thermodynamical analogy we suppose a given physical state $R_0 R_1$ represented by a first trajectory as shown in Fig. A.2. Suppose we wish to make a transition of state $R_0 R_1$, characterized by different pressure, volume, and temperature, into state $P_0 P_1$, represented by another trajectory. These two trajectories correspond to different constant values of the coordinates q^{r+1}, \dots, q^{3N} , called the macroscopic coordinates in the thermodynamical sense.

We must have special forces that are capable of acting on all the molecules, and these forces supply work. The work supplied by these forces will be equivalent to the heat supplied to the system. If in this transition the volume is changed, external work will be done against the forces which cause the constraints $\delta W = \delta V^*$.

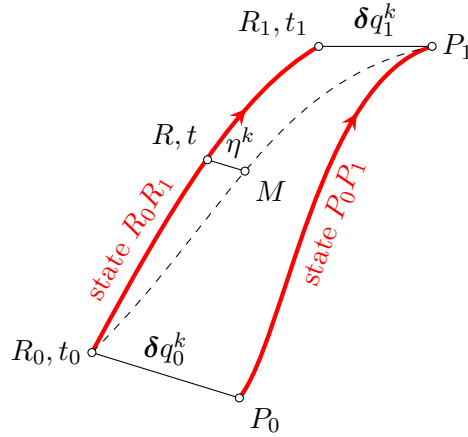


Figure A.2.: A very slow transformation from a physical state $R_0 R_1$ to the physical state $P_0 P_1$ leads to Boltzmann's formula.

The heat supplied to the system will, on the one hand, increase the total internal energy E and, on the other hand, furnish the external work W . We have then

$$\delta Q = \delta E + \delta W = \delta E + \delta V^* \quad (\text{A.31})$$

which is the heat supplied to the system (δQ), the increase of disordered internal energy (δE) and the ordered work furnished by the system against constraint mechanism ($\delta W = \delta V^*$) according to Boltzmann [Bol66] (see also [Grö08; Grö09]).

We assume a continuous and gradual transition from the trajectory $R_0 R_1$, characterized by certain constant values of q^{r+1}, \dots, q^{3N} , to the trajectory $P_0 P_1$, characterized by values of the coordinates $q^k + \delta q^k$, that starts at time t_0 and ends at time t_1 , represented by the path $R_0 M P_1$. At time t the ratio of change between the two states is represented by the segment RM given as

$$\eta^k = \frac{t - t_0}{t_1 - t_0} \delta q^k. \quad (\text{A.32})$$

In a time dt , the change is

$$d\eta^k = \frac{dt}{t_1 - t_0} \delta q^k. \quad (\text{A.33})$$

The heat furnished to the system in the time dt to bring about the change is

$$d(\delta Q) = \frac{dt}{t_1 - t_0} \delta Q. \quad (\text{A.34})$$

The work done by the system is then

$$d(\delta V^*) = \frac{dt}{t_1 - t_0} \delta V^* \quad (\text{A.35})$$

where the definitions are exactly those used before, δQ and δV^* being the quantities defined for a sudden jump and $d(\delta Q)$, $d(\delta V^*)$ being the same quantities for an infinitesimal transformation.

The total supply of heat ΔQ given to the system during time $t_1 - t_0$ of the transformation with the use of (A.31) reads

$$\Delta Q = \int_{t_0}^{t_1} d(\delta Q) = \frac{1}{t_1 - t_0} \int_{t_0}^{t_1} \delta Q dt = \frac{1}{t_1 - t_0} \int_{t_0}^{t_1} (\delta E + \delta V^*) dt. \quad (\text{A.36})$$

To compare this result with integral (A.30) we make the hypothesis that *the varied motion keeps the values of the hidden coordinates $q^{r+1} \dots q^{3N}$ constant and very small*. Under those circumstances the velocities \dot{q}^k , $k = r + 1, \dots, 3N$, would vanish in the varied motion as it does in the natural motion, and the term

$$\delta \sum_{k=r+1}^{3N} p_k \dot{q}^k = 0 \quad (\text{A.37})$$

disappears in Eq. (A.30). Therefore, we find a general form of Boltzmann's formula by substitution of Eq. (A.30) into (A.36) as

$$\Delta Q = \frac{1}{t_1 - t_0} \left(\delta F - \sum_{k=1}^r p_k \delta q^k \Big|_{t_0 + \delta t_0}^{t_1 + \delta t_1} \right). \quad (\text{A.38})$$

A.2.1. Periodic motions

At that point, we move one step further and close the trajectories of Fig. A.2 which yields a periodic configuration as provided in Fig. A.3. In this special case the two points R_0 and R_1 coincide, as well as the two points P_0 , P_1 of the varied trajectory.

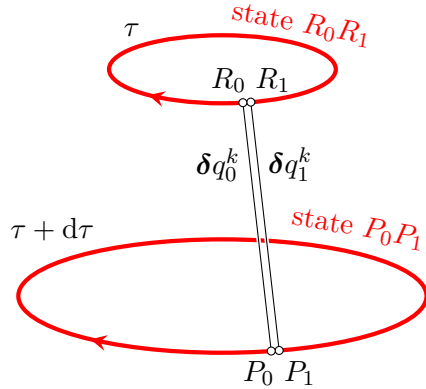


Figure A.3.: The δ -variation adapted to periodic motion with each start point, R_0 and P_0 , connected to its corresponding end point, R_1 and P_1 , respectively.

The δq_i^k are equal, and also the momenta p_{ik} ,

$$\delta q_0^k = \delta q_1^k, \quad p_{0k} = p_{1k}. \quad (\text{A.39})$$

We apply these relations to Eq. (A.38) where the sum disappears. We then find for a cyclic motion with period $\tau = t_1 - t_0 = 2\pi/\omega$ that

$$\Delta Q = \frac{1}{\tau} 2\delta \int_0^\tau T dt. \quad (\text{A.40})$$

Suppose that we could make a canonical transformation (c.f. [Gol02; HF98]) from variables p, q to a different, but still canonical, set of variables I, ψ , whereby in terms of the new variables the new Hamiltonian lacks any dependence on ψ , i.e. $H = H(I)$. Because H is constant in this periodic system and depends only on I , I itself must be a constant of the motion, thus

$$\dot{I} = -\frac{\partial H}{\partial \psi} = 0, \quad \dot{\psi} = \frac{\partial H}{\partial I} = \text{const.} \quad (\text{A.41})$$

The variable ψ must increase linearly with the time

$$\omega(I) \equiv \dot{\psi} = \frac{\partial H}{\partial I}, \quad \psi = \omega(t - t_0). \quad (\text{A.42})$$

Here, I is the action variable which plays the role of a momentum, while ψ is the coordinate conjugate to I and is called the angle variable.

With the use of an appropriate type- F_1 generating function, $\tilde{W}(q, \psi)$, which is a function of both old and new coordinate variables. Since the motion is periodic in p, q , then the motion must also be periodic in ψ , so $\tilde{W}(q, \psi)$ is a periodic function of ψ . We have then

$$d\tilde{W} = p dq - I d\psi \quad (\text{A.43})$$

and integration over a single period of the motion, q returns to its original value, while ψ advances by the amount of one period, 2π ,

$$\oint d\tilde{W} = 0 = \oint p dq - \oint I d\psi. \quad (\text{A.44})$$

Because I is a constant, it can be taken out of the integral. With the integral $\oint d\psi = 2\pi$ we get

$$I = \frac{1}{2\pi} \oint p dq. \quad (\text{A.45})$$

Comparing this result with Eq. (A.15), one recognizes immediately the identity of I with the abbreviated action F , since

$$\oint p dq = \int_0^\tau p \dot{q} dt = \int_0^\tau 2T dt = F \quad (\text{A.46})$$

and hence

$$\delta F = 2 \int_0^\tau \delta T dt. \quad (\text{A.47})$$

On the other hand, for the special case that the period τ remains constant¹ during the transition, i.e. $\delta\tau = 0$, Boltzmann [Bol66] has shown that the heat supplied to the system then splits up into two equal parts, heat and work energy, respectively, expressed by

$$\delta Q = 2\delta E, \quad \delta L = \delta E. \quad (\text{A.48})$$

Now, this formulation is equivalent with the vanishing of the variation of the potential energy V , i.e. $\delta V = 0$, and hence the variation of the action due to the change from the natural to the varied trajectory reads as

$$\delta S = \delta \int_0^\tau (T - V) dt = \int_0^\tau \delta T dt, \quad (\text{A.49})$$

which leads by substitution of Eq. (A.45) into (A.40) to [Grö08; Grö09]

$$\Delta Q = \omega \delta F = 2\omega \delta S. \quad (\text{A.50})$$

¹Due to the definition of the bold-faced δ -variation (A.5), $\delta q^k \approx \delta q^k + \dot{q}^k \delta t$, the rightmost term containing $\delta t = 0$ vanishes and reduces the variation to a standard variation, $\delta \rightarrow \delta$.

B. Mathematical relations

B.1. Random variables

Let X be a random variable. If the values x which X can assume are continuously distributed, we define the probability density of the random variable to be $P(x)$. This means that $P(x) dx$ is the probability that X assumes a value in the interval $[x, x + dx]$. The total probability must be one, i.e. $P(x)$ is normalized to one:

$$\int P(x) dx = 1. \tag{B.1}$$

The mean value of X is defined by

$$\bar{X} = \int xP(x) dx. \tag{B.2}$$

Now let $F(X)$ be a function of the random variable X ; we call $F(X)$ a random function. Its mean value is defined corresponding to Eq. (B.2) by

$$\overline{F(X)} = \int F(x)P(x) dx. \tag{B.3}$$

By default, we shall use different symbols for mean values over space \bar{x} , and mean values over time $\langle x \rangle$, if not otherwise noted (see any good textbook, e.g. [Sch06; WH06]).

Let us consider continuous probability densities on the real line, i.e. in one dimension, with or without explicit time dependence: $P \in L^1(\mathbb{R})$; $\int_{\mathbb{R}} P(x) dx = 1$. Then we can define the expectation value (mean value) by

$$\mu := \bar{x} = \int xP(x) dx, \tag{B.4}$$

and the variance by

$$\sigma^2 := \overline{(x - \bar{x})^2} = \int (x - \mu)^2 P(x) dx. \tag{B.5}$$

The standard deviation σ equals the square root of the variance.

B.2. Vectors and fields

The following is an overview on often used identities in Cartesian vector calculus (see any good Textbook, e.g., [Pre10]).

Let's start with the nabla operator

$$\nabla = \mathbf{e}_x \frac{\partial}{\partial x} + \mathbf{e}_y \frac{\partial}{\partial y} + \mathbf{e}_z \frac{\partial}{\partial z}, \quad (\text{B.6})$$

which is of vector type. \mathbf{e}_u denotes the unit vector in u -direction. If needed, brackets have to be set in order to define the scope of the operator, e.g.,

$$\nabla (fg) = (\nabla f)g + f\nabla g, \quad (\text{B.7})$$

$$\nabla (\mathbf{f} \cdot \mathbf{g}) = (\nabla \otimes \mathbf{f}) \cdot \mathbf{g} + (\nabla \otimes \mathbf{g}) \cdot \mathbf{f}, \quad (\text{B.8})$$

$$\nabla \otimes (f\mathbf{g}) = (\nabla f) \otimes \mathbf{g} + f\nabla \otimes \mathbf{g}. \quad (\text{B.9})$$

In Eqs. (B.7)–(B.9) the nabla operator applies on a product of terms, the result is of vector type or tensor type as in Eq. (B.9), respectively.

Tab. B.1 shows elementary nabla operations in Cartesian coordinates.

Finally, we mention some frequently used rules in one variable, denoting the derivative by prime:

$$(fg)' = f'g + fg' \quad (\text{B.10})$$

$$\left(\frac{f}{g}\right)' = \frac{f'g - fg'}{g^2} \quad (\text{B.11})$$

$$(f(g))' = f'(g)g' \quad (\text{B.12})$$

$$\int f'g = fg - \int fg' \quad (\text{B.13})$$

$$\int \frac{f'}{f} = \ln |f| \quad (\text{B.14})$$

The result of integration over (B.10) yields Eq. (B.13). Eq. (B.14) can also be achieved by substituting $f \rightarrow \ln f$ and $g \rightarrow f$ into (B.12).

B.3. Entropic functionals

Now we derive some practical identities. These identities hold true on general information theoretic grounds and are thus not bound to quantum mechanical issues. Symbols being used are scalars f and vectors \mathbf{f} in Cartesian coordinates (cf. [Gar08]). Starting with

$$\nabla \ln f = \frac{\nabla f}{f} \quad (\text{B.15})$$

$\nabla f = \mathbf{e}_x \partial_x f + \mathbf{e}_y \partial_y f + \mathbf{e}_z \partial_z f$
$\nabla \cdot \mathbf{f} = \partial_x f_x + \partial_y f_y + \partial_z f_z$
$\nabla \times \mathbf{f} = \mathbf{e}_x (\partial_y f_z - \partial_z f_y) + \mathbf{e}_y (\partial_z f_x - \partial_x f_z) + \mathbf{e}_z (\partial_x f_y - \partial_y f_x)$
$\nabla^2 f = \partial_x^2 f + \partial_y^2 f + \partial_z^2 f$
$\nabla(f + g) = \nabla f + \nabla g$
$\nabla \cdot (\mathbf{f} + \mathbf{g}) = \nabla \cdot \mathbf{f} + \nabla \cdot \mathbf{g}$
$\nabla \times (\mathbf{f} + \mathbf{g}) = \nabla \times \mathbf{f} + \nabla \times \mathbf{g}$
$\nabla(fg) = f \nabla g + g \nabla f$
$\nabla \cdot (f\mathbf{g}) = f \nabla \cdot \mathbf{g} + \mathbf{g} \cdot \nabla f$
$\nabla \times (f\mathbf{g}) = f \nabla \times \mathbf{g} + (\nabla f) \times \mathbf{g}$
$\nabla(\mathbf{f} \cdot \mathbf{g}) = \mathbf{f} \cdot \nabla \mathbf{g} + \mathbf{g} \cdot \nabla \mathbf{f} + \mathbf{f} \times (\nabla \times \mathbf{g}) + \mathbf{g} \times (\nabla \times \mathbf{f})$
$\nabla \cdot (\mathbf{f} \times \mathbf{g}) = \mathbf{g} \cdot (\nabla \times \mathbf{f}) - \mathbf{f} \cdot (\nabla \times \mathbf{g})$
$\nabla \times (\mathbf{f} \times \mathbf{g}) = \mathbf{f} \nabla \cdot \mathbf{g} - \mathbf{g} \nabla \cdot \mathbf{f} + \mathbf{g} \cdot \nabla \mathbf{f} - \mathbf{f} \cdot \nabla \mathbf{g}$
$\nabla \cdot (\nabla f) = \nabla^2 f = \Delta f$
$\nabla \times (\nabla f) = \mathbf{0}$
$\nabla \cdot (\nabla \times \mathbf{f}) = 0$
$\nabla \times (\nabla \times \mathbf{f}) = \nabla(\nabla \cdot \mathbf{f}) - \nabla^2 \mathbf{f}$

Table B.1.: Elementary nabla calculus; Cartesian coordinates x, y, z ; f and g denote scalar fields, \mathbf{f} and \mathbf{g} denote vector fields.

which is a special case of Eq. (B.12) and hence analogue to (B.14). Next,

$$\nabla^2 \ln f = \nabla \cdot (\nabla \ln f) \tag{B.16}$$

$$= \nabla \cdot \left(\frac{\nabla f}{f} \right) \tag{B.17}$$

$$= \frac{f \nabla^2 f - (\nabla f)^2}{f^2} \tag{B.18}$$

$$= \frac{\nabla^2 f}{f} - \left(\frac{\nabla f}{f} \right)^2, \tag{B.19}$$

and thus, reordered, we obtain

$$\frac{\nabla^2 f}{f} = \nabla^2 \ln f + \left(\frac{\nabla f}{f} \right)^2. \quad (\text{B.20})$$

Obviously, Eq. (B.11) has been used in (B.18). Substitution of $f = \sqrt{g}$ into (B.20) leads to

$$\begin{aligned} \frac{\nabla^2 \sqrt{g}}{\sqrt{g}} &= \frac{\nabla^2 g^{1/2}}{g^{1/2}} \\ &= \nabla^2 \ln g^{1/2} + \left(\nabla \ln g^{1/2} \right)^2 \\ &= \frac{1}{2} \nabla^2 \ln g + \frac{1}{4} (\nabla \ln g)^2, \end{aligned} \quad (\text{B.21})$$

and

$$\begin{aligned} \frac{\nabla f}{f} &= \frac{\nabla \sqrt{g}}{\sqrt{g}} = \nabla \ln \sqrt{g} = \frac{1}{2} \nabla \ln g \\ &= \frac{1}{2} \frac{\nabla g}{g}. \end{aligned} \quad (\text{B.22})$$

For further calculations we make use of the above introduced probability function P which leads us from (B.15) to

$$\begin{aligned} \overline{\nabla \ln P} &= \frac{\overline{\nabla P}}{P} = \int P \frac{\nabla P}{P} dx \\ &= \int \nabla P dx = P \Big|_{-\infty}^{\infty} = 0. \end{aligned} \quad (\text{B.23})$$

Note that $P(-\infty) = 0$ and $P(\infty) = 0$ must hold since the integral over R equals a finite value, namely 1. Further, from (B.20) we obtain

$$\frac{\overline{\nabla^2 P}}{P} = \overline{\nabla^2 \ln P} + \overline{\left(\frac{\nabla P}{P} \right)^2} \quad (\text{B.24})$$

$$= \int P \frac{\nabla^2 P}{P} dx = \int \nabla^2 P dx \quad (\text{B.25})$$

$$= \int \nabla \cdot \nabla P dx = \nabla P \Big|_{-\infty}^{\infty} = 0. \quad (\text{B.26})$$

For P we must demand that any derivative of P must vanish at its limits, i.e. $\lim_{x \rightarrow \pm\infty} \nabla^n P(x) = 0$, $n \geq 0$, otherwise we have $\int_{-\infty}^{\infty} \nabla^n P(x) dx \neq 0$ that leads us to at least one further integral from $-\infty$ to $-\infty$ which therefore cannot be finite.

As (B.26) is the value of the l.h.s. of (B.24), the r.h.s. of (B.24) must also vanish. By considering Eq. (B.15) we obtain

$$-\overline{\nabla^2 \ln P} = \overline{(\nabla \ln P)^2} = \overline{\left(\frac{\nabla P}{P}\right)^2}. \quad (\text{B.27})$$

The mean value of Eq. (B.21) can hence be obtained by

$$\frac{\overline{\nabla^2 \sqrt{P}}}{\sqrt{P}} = \frac{1}{2} \overline{\nabla^2 \ln P} + \frac{1}{4} \overline{(\nabla \ln P)^2} \quad (\text{B.28})$$

$$= \frac{1}{4} \overline{\nabla^2 \ln P} = -\frac{1}{4} \overline{\left(\frac{\nabla P}{P}\right)^2}. \quad (\text{B.29})$$

Bibliography

- [BA14] Brady, R. and Anderson, R. ‘Why bouncing droplets are a pretty good model of quantum mechanics’. *pre-print* (2014). arXiv: [1401.4356 \[physics, physics:quant-ph\]](#).
- [Bez14] Bezanson, J., Edelman, A., Karpinski, S. and Shah, V. B. ‘Julia: a fresh approach to numerical computing’. *pre-print* (2014). arXiv: [1411.1607 \[cs.MS\]](#).
- [BH93] Bohm, D. and Hiley, B. J. *The Undivided Universe: An Ontological Interpretation of Quantum Theory*. London, UK: Routledge, 1993.
- [Bli13] Bliokh, K. Y., Bekshaev, A. Y., Kofman, A. G. and Nori, F. ‘Photon trajectories, anomalous velocities, and weak measurements: A classical interpretation’. *New J. Phys.* **15** (2013), 073022. DOI: [10.1088/1367-2630/15/7/073022](#). arXiv: [1304.1276 \[quant-ph\]](#).
- [Bol10] Bologna, M., Ascolani, G. and Grigolini, P. ‘Density approach to ballistic anomalous diffusion: an exact analytical treatment’. *J. Math. Phys.* **51** No. 4 (2010), 043303. DOI: [10.1063/1.3355199](#).
- [Bol66] Boltzmann, L. ‘Über die mechanische Bedeutung des zweiten Hauptsatzes der Wärmetheorie’. *Wien. Ber.* **53** (1866), 195–200.
- [Bri64] Brillouin, L. *Tensors in Mechanics and Elasticity*. New York, NY: Academic Press, 1964.
- [BY07] Burgdörfer, J. and Yoshida, S. *Statistical Physics II*. Vienna University of Technology: Skriptum, 2007.
- [Cam10] Campbell, S. L., Chancelier, J.-P. and Nikoukhah, R. *Modeling and simulation in Scilab/Scicos with ScicosLab 4.4*. 2nd ed. OCLC: 602828704. New York, NY: Springer, 2010.
- [CdIP12] Cetto, A. M. and de la Peña, L. ‘Quantization as an emergent phenomenon due to matter-zero-point field interaction’. *J. Phys.: Conf. Ser.* **361** No. 1 (2012), 012013. DOI: [10.1088/1742-6596/361/1/012013](#).

- [CF06] Couder, Y. and Fort, E. ‘Single-particle diffraction and interference at a macroscopic scale’. *Phys. Rev. Lett.* **97** (2006), 154101. DOI: [10.1103/PhysRevLett.97.154101](https://doi.org/10.1103/PhysRevLett.97.154101).
- [CF12] Couder, Y. and Fort, E. ‘Probabilities and trajectories in a classical wave-particle duality’. *J. Phys.: Conf. Ser.* **361** No. 1 (2012), 012001. DOI: [10.1088/1742-6596/361/1/012001](https://doi.org/10.1088/1742-6596/361/1/012001).
- [Cof04] Coffey, W. T., Kalmykov, Y. P. and Waldron, J. T. *The Langevin Equation: With Applications to Stochastic Problems in Physics, Chemistry and Electrical Engineering*. 2nd ed. Vol. 14. World Scientific series in contemporary chemical physics. Singapore: World Scientific, 2004.
- [Cou05] Couder, Y., Protière, S., Fort, E. and Boudaoud, A. ‘Dynamical phenomena: Walking and orbiting droplets’. *Nature* **437** (2005), 208–208. DOI: [10.1038/437208a](https://doi.org/10.1038/437208a).
- [Cou10] Couder, Y., Boudaoud, A., Protière, S. and Fort, E. ‘Walking droplets, a form of wave-particle duality at macroscopic scale?’ *Europhys. News* **41** No. 1 (2010), 5. DOI: [10.1051/epn/2010101](https://doi.org/10.1051/epn/2010101).
- [Dav15] Davidovic, M., Sanz, A. S. and Bozic, M. ‘Description of classical and quantum interference in view of the concept of flow line’. *J. Russ. Laser Res.* **36** No. 4 (2015), 329–342. DOI: [10.1007/s10946-015-9507-y](https://doi.org/10.1007/s10946-015-9507-y). arXiv: [1508.05194](https://arxiv.org/abs/1508.05194) [quant-ph].
- [dBro60] De Broglie, L. V. P. R. *Non-Linear Wave Mechanics: A Causal Interpretation*. Amsterdam: Elsevier, 1960.
- [Dem06] Demtröder, W. *Experimentalphysik 1, Mechanik und Wärme*. 4th ed. Berlin: Springer, 2006.
- [DeR12] De Raedt, H., Jin, F. and Michielsen, K. ‘Discrete-event simulation of neutron interferometry experiments’. *AIP Conf. Proc.* **1508** No. 1 (2012), 172–186. DOI: [10.1063/1.4773129](https://doi.org/10.1063/1.4773129).
- [dGdG16] De Gosson, C. and de Gosson, M. ‘Weak values, the reconstruction problem, and the uncertainty principle’. *J. Phys.: Conf. Ser.* **701** (2016), 012011. DOI: [10.1088/1742-6596/701/1/012011](https://doi.org/10.1088/1742-6596/701/1/012011).
- [dGos16] De Gosson, M., Hiley, B. and Cohen, E. ‘Observing quantum trajectories: From Mott’s problem to quantum Zeno effect and back’. *Ann. Phys.* **374** (2016), 190–211. DOI: [10.1016/j.aop.2016.08.003](https://doi.org/10.1016/j.aop.2016.08.003). arXiv: [1606.06065](https://arxiv.org/abs/1606.06065) [quant-ph].
- [dlPeñ14] De la Peña, L., Cetto, A. M. and Valdés-Hernández, A. *The Emerging Quantum: The Physics behind Quantum Mechanics*. Berlin: Springer, 2014.

- [Edd09] Eddi, A., Fort, E., Moisy, F. and Couder, Y. ‘Unpredictable tunneling of a classical wave-particle association’. *Phys. Rev. Lett.* **102** (2009), 240401. DOI: [10.1103/PhysRevLett.102.240401](https://doi.org/10.1103/PhysRevLett.102.240401).
- [Elz11] Elze, H.-T., Gambarotta, G. and Vallone, F. ‘General linear dynamics - quantum, classical or hybrid’. *J. Phys.: Conf. Ser.* **306** (2011), 012010. DOI: [10.1088/1742-6596/306/1/012010](https://doi.org/10.1088/1742-6596/306/1/012010).
- [For10] Fort, E., Eddi, A., Boudaoud, A., Moukhtar, J. and Couder, Y. ‘Path-memory induced quantization of classical orbits’. *PNAS* **107** No. 41 (2010), 17515–17520. DOI: [10.1073/pnas.1007386107](https://doi.org/10.1073/pnas.1007386107).
- [Fre05] Freire Jr, O. ‘Science and exile: David Bohm, the cold war, and a new interpretation of quantum mechanics’. *HSPS* **36** No. 1 (2005), 1–34. DOI: [10.1525/hsp.2005.36.1.1](https://doi.org/10.1525/hsp.2005.36.1.1). arXiv: [physics/0508184](https://arxiv.org/abs/physics/0508184) [[physics.hist-ph](#)].
- [Fus14] Fussy, S., Mesa Pascasio, J., Schwabl, H. and Grössing, G. ‘Born’s rule as signature of a superclassical current algebra’. *Ann. Phys.* **343** (2014), 200–214. DOI: [10.1016/j.aop.2014.02.002](https://doi.org/10.1016/j.aop.2014.02.002). arXiv: [1308.5924](https://arxiv.org/abs/1308.5924) [[quant-ph](#)].
- [Gar08] Garbaczewski, P. ‘Information dynamics: Temporal behavior of uncertainty measures’. *Cent. Eur. J. Phys.* **6** No. 1 (2008), 158–170. DOI: [10.2478/s11534-008-0020-6](https://doi.org/10.2478/s11534-008-0020-6).
- [Gol02] Goldstein, H., Poole, C. P. and Safko, J. L. *Classical Mechanics*. 3rd ed. New York, NY: Addison-Wesley, 2002.
- [Grö04] Grössing, G. ‘From classical Hamiltonian flow to quantum theory: Derivation of the Schrödinger equation’. *Found. Phys. Lett.* **17** No. 4 (2004), 343–362. DOI: [10.1023/B:FOPL.0000035669.03595.ce](https://doi.org/10.1023/B:FOPL.0000035669.03595.ce). arXiv: [quant-ph/0311109](https://arxiv.org/abs/quant-ph/0311109).
- [Grö08] Grössing, G. ‘The vacuum fluctuation theorem: Exact Schrödinger equation via nonequilibrium thermodynamics’. *Phys. Lett. A* **372** No. 25 (2008), 4556–4563. DOI: [10.1016/j.physleta.2008.05.007](https://doi.org/10.1016/j.physleta.2008.05.007). arXiv: [0711.4954](https://arxiv.org/abs/0711.4954) [[quant-ph](#)].
- [Grö09] Grössing, G. ‘On the thermodynamic origin of the quantum potential’. *Physica A* **388** (2009), 811–823. DOI: [10.1016/j.physa.2008.11.033](https://doi.org/10.1016/j.physa.2008.11.033). arXiv: [0808.3539](https://arxiv.org/abs/0808.3539) [[quant-ph](#)].
- [Grö10a] Grössing, G. ‘Sub-quantum thermodynamics as a basis of emergent quantum mechanics’. *Entropy* **12** No. 9 (2010), 1975–2044. DOI: [10.3390/e12091975](https://doi.org/10.3390/e12091975).

- [Grö10b] Grössing, G., Fussy, S., Mesa Pascasio, J. and Schwabl, H. ‘Emergence and collapse of quantum mechanical superposition: Orthogonality of reversible dynamics and irreversible diffusion’. *Physica A* **389** No. 21 (2010), 4473–4484. DOI: [10.1016/j.physa.2010.07.017](https://doi.org/10.1016/j.physa.2010.07.017). arXiv: [1004.4596](https://arxiv.org/abs/1004.4596) [quant-ph].
- [Grö11a] Grössing, G., Fussy, S., Mesa Pascasio, J. and Schwabl, H. ‘Elements of sub-quantum thermodynamics: Quantum motion as ballistic diffusion’. *J. Phys.: Conf. Ser.* DICE2010, 13–17 September 2010, Castiglioncello, Italy **306** (2011), 012046. DOI: [10.1088/1742-6596/306/1/012046](https://doi.org/10.1088/1742-6596/306/1/012046). arXiv: [1005.1058](https://arxiv.org/abs/1005.1058) [physics.gen-ph].
- [Grö11b] Grössing, G., Mesa Pascasio, J. and Schwabl, H. ‘A classical explanation of quantization’. *Found. Phys.* **41** No. 9 (2011), 1437–1453. DOI: [10.1007/s10701-011-9556-1](https://doi.org/10.1007/s10701-011-9556-1). arXiv: [0812.3561](https://arxiv.org/abs/0812.3561) [quant-ph].
- [Grö12a] Grössing, G., Fussy, S., Mesa Pascasio, J. and Schwabl, H. ‘A classical framework for nonlocality and entanglement’. *AIP Conf. Proc.* QTRF6, 11–14 June 2012, Växjö, Sweden **1508** (2012), 187–196. DOI: [10.1063/1.4773130](https://doi.org/10.1063/1.4773130). arXiv: [1210.4406](https://arxiv.org/abs/1210.4406) [quant-ph].
- [Grö12b] Grössing, G., Fussy, S., Mesa Pascasio, J. and Schwabl, H. ‘An explanation of interference effects in the double slit experiment: Classical trajectories plus ballistic diffusion caused by zero-point fluctuations’. *Ann. Phys.* **327** No. 2 (2012), 421–437. DOI: [10.1016/j.aop.2011.11.010](https://doi.org/10.1016/j.aop.2011.11.010). arXiv: [1106.5994](https://arxiv.org/abs/1106.5994) [quant-ph].
- [Grö12c] Grössing, G., Fussy, S., Mesa Pascasio, J. and Schwabl, H. ‘The quantum as an emergent system’. *J. Phys.: Conf. Ser.* EmerQuM11, 11–13 November 2011, Vienna, Austria **361** (2012), 012008. DOI: [10.1088/1742-6596/361/1/012008](https://doi.org/10.1088/1742-6596/361/1/012008). arXiv: [1205.3393](https://arxiv.org/abs/1205.3393) [quant-ph].
- [Grö13] Grössing, G., Fussy, S., Mesa Pascasio, J. and Schwabl, H. ‘Systemic nonlocality’ from changing constraints on sub-quantum kinematics’. *J. Phys.: Conf. Ser.* DICE2012, 17–21 September 2012, Castiglioncello, Italy **442** (2013), 012012. DOI: [10.1088/1742-6596/442/1/012012](https://doi.org/10.1088/1742-6596/442/1/012012). arXiv: [1303.2867](https://arxiv.org/abs/1303.2867) [quant-ph].
- [Grö14a] Grössing, G. ‘Emergence of quantum mechanics from a sub-quantum statistical mechanics’. *Int. J. Mod. Phys. B* (2014), 145–179. DOI: [10.1142/S0217979214501793](https://doi.org/10.1142/S0217979214501793). arXiv: [1304.3719](https://arxiv.org/abs/1304.3719) [quant-ph].
- [Grö14b] Grössing, G., Elze, H.-T., Mesa Pascasio, J. and Walleczek, J., eds. *Emergent Quantum Mechanics 2013*. Vol. 504. Url: <http://iopscience.iop.org/1742-6596/504/1>. Bristol: IOP Publishing, 2014.

- [Grö14c] Grössing, G., Fussy, S., Mesa Pascasio, J. and Schwabl, H. ‘Relational causality and classical probability: Grounding quantum phenomenology in a superclassical theory’. *J. Phys.: Conf. Ser.* EmQM13, 3–6 October 2013, Vienna, Austria **504** (2014), 012006. DOI: [10.1088/1742-6596/504/1/012006](https://doi.org/10.1088/1742-6596/504/1/012006). arXiv: [1403.3295 \[quant-ph\]](https://arxiv.org/abs/1403.3295).
- [Grö15a] Grössing, G., Fussy, S., Mesa Pascasio, J. and Schwabl, H. ‘Extreme beam attenuation in double-slit experiments: Quantum and subquantum scenarios’. *Ann. Phys.* **353** (2015), 271–281. DOI: [10.1016/j.aop.2014.11.015](https://doi.org/10.1016/j.aop.2014.11.015). arXiv: [1406.1346 \[quant-ph\]](https://arxiv.org/abs/1406.1346).
- [Grö15b] Grössing, G., Fussy, S., Mesa Pascasio, J. and Schwabl, H. ‘The quantum sweeper effect’. *J. Phys.: Conf. Ser.* DICE2014, 15–19 September 2014, Castiglioncello, Italy **626** No. 1 (2015), 012017. DOI: [10.1088/1742-6596/626/1/012017](https://doi.org/10.1088/1742-6596/626/1/012017). arXiv: [1502.04034 \[quant-ph\]](https://arxiv.org/abs/1502.04034).
- [Grö16a] Grössing, G., Elze, H.-T., Mesa Pascasio, J. and Walleczek, J., eds. *Emergent Quantum Mechanics 2015*. Url: <http://iopscience.iop.org/1742-6596/701/1>. Bristol: IOP Publishing, 2016.
- [Grö16b] Grössing, G., Fussy, S., Mesa Pascasio, J. and Schwabl, H. ‘Conditions for Lorentz-invariant superluminal information transfer without signaling’. *J. Phys.: Conf. Ser.* **701** (2016), 012006. DOI: [10.1088/1742-6596/701/1/012006](https://doi.org/10.1088/1742-6596/701/1/012006). arXiv: [1603.02123 \[quant-ph\]](https://arxiv.org/abs/1603.02123).
- [Haa99] Haas, H. *Numerische Berechnung elektromagnetischer Felder*. Vienna University of Technology: Skriptum, 1999.
- [Ham67] Hamel, G. *Theoretische Mechanik*. Vol. 57. Die Grundlehren der mathematischen Wissenschaften. Berlin, Heidelberg: Springer, 1967.
- [Har13] Harris, D. M., Moukhtar, J., Fort, E., Couder, Y. and Bush, J. W. M. ‘Wavelike statistics from pilot-wave dynamics in a circular corral’. *Phys. Rev. E* **88** No. 1 (2013). DOI: [10.1103/PhysRevE.88.011001](https://doi.org/10.1103/PhysRevE.88.011001).
- [HF98] Hand, L. N. and Finch, J. D. *Analytical Mechanics*. Cambridge, UK: Cambridge Univ. Press, 1998.
- [Hil12] Hiley, B. J. ‘Weak values: Approach through the Clifford and Moyal algebras’. *J. Phys.: Conf. Ser.* **361** No. 1 (2012), 012014. DOI: [10.1088/1742-6596/361/1/012014](https://doi.org/10.1088/1742-6596/361/1/012014). arXiv: [1111.6536v1 \[quant-ph\]](https://arxiv.org/abs/1111.6536v1).
- [Hil16] Hiley, B. J., de Gosson, M. A. and Dennis, G. ‘Quantum trajectories: Dirac, Moyal and Bohm’. *pre-print* (2016). arXiv: [1610.07130 \[quant-ph\]](https://arxiv.org/abs/1610.07130).
- [Hol82] Holland, P. R. ‘Electromagnetism, particles and anholonomy’. *Phys. Lett. A* **91** No. 6 (1982), 275–278. DOI: [10.1016/0375-9601\(82\)90570-9](https://doi.org/10.1016/0375-9601(82)90570-9).

- [Hol93] Holland, P. R. *The Quantum Theory of Motion*. Cambridge, UK: Cambridge University Press, 1993.
- [JS12a] Jizba, P. and Scardigli, F. ‘Emergence of special and doubly special relativity’. *Phys. Rev. D* **86** No. 2 (2012), 025029. DOI: [10.1103/PhysRevD.86.025029](https://doi.org/10.1103/PhysRevD.86.025029). arXiv: [1105.3930](https://arxiv.org/abs/1105.3930) [hep-th].
- [JS12b] Jizba, P. and Scardigli, F. ‘Quantum mechanics and local Lorentz symmetry violation’. *J. Phys.: Conf. Ser.* **361** No. 1 (2012), 012026. DOI: [10.1088/1742-6596/361/1/012026](https://doi.org/10.1088/1742-6596/361/1/012026).
- [Koc11] Kocsis, S., Braverman, B., Ravets, S., Stevens, M. J., Mirin, R. P., Shalm, L. K. and Steinberg, A. M. ‘Observing the average trajectories of single photons in a two-slit interferometer’. *Science* **332** No. 6034 (2011), 1170–1173. DOI: [10.1126/science.1202218](https://doi.org/10.1126/science.1202218).
- [Lea05] Leavens, C. R. ‘Weak measurements from the point of view of Bohmian mechanics’. *Found. Phys.* **35** No. 3 (2005), 469–491. DOI: [10.1007/s10701-004-1984-8](https://doi.org/10.1007/s10701-004-1984-8).
- [LS15] Luis, A. and Sanz, Á. S. ‘What dynamics can be expected for mixed states in two-slit experiments?’ *Ann. Phys.* **357** (2015), 95–107. DOI: [10.1016/j.aop.2015.03.030](https://doi.org/10.1016/j.aop.2015.03.030). arXiv: [1311.2612](https://arxiv.org/abs/1311.2612) [quant-ph].
- [Man00] Mandelis, A. ‘Diffusion waves and their uses’. *Phys. Today* **53** No. 8 (2000), 29–34. DOI: [10.1063/1.1310118](https://doi.org/10.1063/1.1310118).
- [Man01] Mandelis, A., Nicolaides, L. and Chen, Y. ‘Structure and the reflectionless/refractionless nature of parabolic diffusion-wave fields’. *Phys. Rev. Lett.* **87** No. 2 (2001), 020801. DOI: [10.1103/PhysRevLett.87.020801](https://doi.org/10.1103/PhysRevLett.87.020801).
- [Mes12] Mesa Pascasio, J., Fussy, S., Schwabl, H. and Grössing, G. ‘Classical simulation of double slit interference via ballistic diffusion’. *J. Phys.: Conf. Ser.* EmerQuM11, 11–13 November 2011, Vienna, Austria **361** (2012), 012041. DOI: [10.1088/1742-6596/361/1/012041](https://doi.org/10.1088/1742-6596/361/1/012041). arXiv: [1205.4521](https://arxiv.org/abs/1205.4521) [quant-ph].
- [Mes13] Mesa Pascasio, J., Fussy, S., Schwabl, H. and Grössing, G. ‘Modeling quantum mechanical double slit interference via anomalous diffusion: Independently variable slit widths’. *Physica A* **392** No. 12 (2013), 2718–2727. DOI: [10.1016/j.physa.2013.02.006](https://doi.org/10.1016/j.physa.2013.02.006). arXiv: [1304.2885](https://arxiv.org/abs/1304.2885) [quant-ph].

- [Mes16] Mesa Pascasio, J., Fussy, S., Schwabl, H. and Grössing, G. ‘Emergent quantum mechanics without wave functions’. *J. Phys.: Conf. Ser.* EmQM15, 23–25 October 2015, Vienna, Austria **701** (2016), 012036. DOI: [10.1088/1742-6596/701/1/012036](https://doi.org/10.1088/1742-6596/701/1/012036). arXiv: [1602.04932](https://arxiv.org/abs/1602.04932) [quant-ph].
- [Phi79] Philippidis, C., Dewdney, C. and Hiley, B. J. ‘Quantum interference and the quantum potential’. *Nuov. Cim. B* **52** No. 1 (1979), 15–28. DOI: [10.1007/BF02743566](https://doi.org/10.1007/BF02743566).
- [Pre10] Prechtel, A. *Vorlesungen über Elektrodynamik*. Vienna University of Technology: Skriptum, 2010.
- [Pro06] Protière, S., Boudaoud, A. and Couder, Y. ‘Particle-wave association on a fluid interface’. *J. Fluid Mech.* **554** (2006), 85–108. DOI: [10.1017/S0022112006009190](https://doi.org/10.1017/S0022112006009190).
- [Rau90] Rauch, H., Summhammer, J., Zawisky, M. and Jericha, E. ‘Low-contrast and low-counting-rate measurements in neutron interferometry’. *Phys. Rev. A* **42** No. 7 (1990), 3726–3732. DOI: [10.1103/PhysRevA.42.3726](https://doi.org/10.1103/PhysRevA.42.3726).
- [Ric14] Richardson, C. D., Schlagheck, P., Martin, J., Vandewalle, N. and Bastin, T. ‘On the analogy of quantum wave-particle duality with bouncing droplets’. *pre-print* (2014). arXiv: [1410.1373](https://arxiv.org/abs/1410.1373) [physics.flu-dyn].
- [RS84] Rauch, H. and Summhammer, J. ‘Static versus time-dependent absorption in neutron interferometry’. *Phys. Lett. A* **104** No. 1 (1984), 44–46. DOI: [10.1016/0375-9601\(84\)90586-3](https://doi.org/10.1016/0375-9601(84)90586-3).
- [RW00] Rauch, H. and Werner, S. A. *Neutron Interferometry: Lessons in Experimental Quantum Mechanics*. New York, NY: Clarendon Press, 2000.
- [RW15] Rauch, H. and Werner, S. A. *Neutron Interferometry: Lessons in Experimental Quantum Mechanics*. 2nd ed. New York, NY: Oxford University Press, 2015.
- [SB09] Sanz, Á. S. and Borondo, F. ‘Contextuality, decoherence and quantum trajectories’. *Chem. Phys. Lett.* **478** No. 4-6 (2009), 301–306. DOI: [10.1016/j.cplett.2009.07.061](https://doi.org/10.1016/j.cplett.2009.07.061). arXiv: [0803.2581](https://arxiv.org/abs/0803.2581) [quant-ph].
- [Sch06] Schwabl, F. *Statistical Mechanics*. 2nd ed. Advanced Texts in Physics. Berlin, Heidelberg: Springer, 2006.
- [Sch10] Scheck, F. *Mechanics from Newton’s Laws to Deterministic Chaos*. 5th ed. Heidelberg, New York: Springer, 2010.

- [Sch12] Schwabl, H., Mesa Pascasio, J., Fussy, S. and Grössing, G. ‘Quantum features derived from the classical model of a bouncer-walker coupled to a zero-point field’. *J. Phys.: Conf. Ser.* EmerQuM11, 11–13 November 2011, Vienna, Austria **361** (2012), 012021. DOI: [10.1088/1742-6596/361/1/012021](https://doi.org/10.1088/1742-6596/361/1/012021). arXiv: [1205.4519 \[quant-ph\]](https://arxiv.org/abs/1205.4519).
- [Scu98] Scully, M. O. ‘Do Bohm trajectories always provide a trustworthy physical picture of particle motion?’ *Phys. Scr.* **T76** No. 1 (1998), 41–46. DOI: [10.1238/Physica.Topical.076a00041](https://doi.org/10.1238/Physica.Topical.076a00041).
- [SK09] Schwarz, H. R. and Köckler, N. *Numerische Mathematik*. 7th ed. Wiesbaden: Vieweg+Teubner, 2009.
- [SM07] Sanz, Á. S. and Miret-Artés, S. ‘A causal look into the quantum Talbot effect’. *J. Chem. Phys.* **126** No. 23 (2007), 234106. DOI: [10.1063/1.2741555](https://doi.org/10.1063/1.2741555).
- [SM08] Sanz, Á. S. and Miret-Artés, S. ‘A trajectory-based understanding of quantum interference’. *J. Phys. A: Math. Gen.* **41** No. 43 (2008), 435303. DOI: [10.1088/1751-8113/41/43/435303](https://doi.org/10.1088/1751-8113/41/43/435303). arXiv: [0806.2105 \[quant-ph\]](https://arxiv.org/abs/0806.2105).
- [SM12] Sanz, Á. S. and Miret-Artés, S. *A Trajectory Description of Quantum Processes. I. Fundamentals. A Bohmian Perspective*. Vol. 850. Lecture Notes in Physics. Heidelberg: Springer, 2012.
- [SM14] Sanz, Á. S. and Miret-Artés, S. *A Trajectory Description of Quantum Processes. II. Applications. A Bohmian Perspective*. Vol. 831. Lecture Notes in Physics. Heidelberg: Springer, 2014.
- [Str04] Strikwerda, J. C. *Finite Difference Schemes and Partial Differential Equations*. 2nd ed. Philadelphia: SIAM, 2004.
- [Sum87] Summhammer, J., Rauch, H. and Tuppinger, D. ‘Stochastic and deterministic absorption in neutron-interference experiments’. *Phys. Rev. A* **36** No. 9 (1987), 4447–4455. DOI: [10.1103/PhysRevA.36.4447](https://doi.org/10.1103/PhysRevA.36.4447).
- [TM87] Toffoli, T. and Margolus, N. *Cellular Automata Machines: A New Environment for Modeling*. Cambridge, MA: MIT Press, 1987.
- [UO30] Uhlenbeck, G. E. and Ornstein, L. S. ‘On the theory of the Brownian motion’. *Phys. Rev.* **36** No. 5 (1930), 823–841. DOI: [10.1103/PhysRev.36.823](https://doi.org/10.1103/PhysRev.36.823).
- [vBlo10] Von Bloh, K. *Causal interpretation of the free quantum particle*. 2010. URL: <http://demonstrations.wolfram.com/CausalInterpretationOfTheFreeQuantumParticle/>.

- [Wal00] Walleczek, J., ed. *Self-Organized Biological Dynamics and Nonlinear Control*. Cambridge, UK: Cambridge University Press, 2000.
- [WG16] Walleczek, J. and Grössing, G. ‘Is the world local or nonlocal? towards an emergent quantum mechanics in the 21st century’. *J. Phys.: Conf. Ser.* **701** (2016), 012001. DOI: [10.1088/1742-6596/701/1/012001](https://doi.org/10.1088/1742-6596/701/1/012001). arXiv: [1603.02862](https://arxiv.org/abs/1603.02862) [quant-ph].
- [WH06] Wachter, A. and Hoerber, H. *Compendium of theoretical physics*. New York, NY: Springer, 2006.
- [Wik16] Wikipedia. *Emergence*. 2016. URL: <https://en.wikipedia.org/wiki/Emergence>.
- [Wis07] Wiseman, H. M. ‘Grounding Bohmian mechanics in weak values and bayesianism’. *New J. Phys.* **9** No. 6 (2007), 165–176. DOI: [10.1088/1367-2630/9/6/165](https://doi.org/10.1088/1367-2630/9/6/165). arXiv: [0706.2522](https://arxiv.org/abs/0706.2522) [quant-ph].
- [Zei88] Zeilinger, A., Gähler, R., Shull, C., Treimer, W. and Mampe, W. ‘Single- and double-slit diffraction of neutrons’. *Rev. Mod. Phys.* **60** No. 4 (1988), 1067–1073. DOI: [10.1103/RevModPhys.60.1067](https://doi.org/10.1103/RevModPhys.60.1067).

Publication list

Journals

- Grössing, G., Fussy, S., Mesa Pascasio, J. and Schwabl, H. ‘Emergence and collapse of quantum mechanical superposition: Orthogonality of reversible dynamics and irreversible diffusion’. *Physica A* **389** No. 21 (2010), 4473–4484. DOI: [10.1016/j.physa.2010.07.017](https://doi.org/10.1016/j.physa.2010.07.017). arXiv: [1004.4596](https://arxiv.org/abs/1004.4596) [quant-ph].
- Grössing, G., Mesa Pascasio, J. and Schwabl, H. ‘A classical explanation of quantization’. *Found. Phys.* **41** No. 9 (2011), 1437–1453. DOI: [10.1007/s10701-011-9556-1](https://doi.org/10.1007/s10701-011-9556-1). arXiv: [0812.3561](https://arxiv.org/abs/0812.3561) [quant-ph].
- Grössing, G., Fussy, S., Mesa Pascasio, J. and Schwabl, H. ‘An explanation of interference effects in the double slit experiment: Classical trajectories plus ballistic diffusion caused by zero-point fluctuations’. *Ann. Phys.* **327** No. 2 (2012), 421–437. DOI: [10.1016/j.aop.2011.11.010](https://doi.org/10.1016/j.aop.2011.11.010). arXiv: [1106.5994](https://arxiv.org/abs/1106.5994) [quant-ph].
- Mesa Pascasio, J., Fussy, S., Schwabl, H. and Grössing, G. ‘Modeling quantum mechanical double slit interference via anomalous diffusion: Independently variable slit widths’. *Physica A* **392** No. 12 (2013), 2718–2727. DOI: [10.1016/j.physa.2013.02.006](https://doi.org/10.1016/j.physa.2013.02.006). arXiv: [1304.2885](https://arxiv.org/abs/1304.2885) [quant-ph].
- Fussy, S., Mesa Pascasio, J., Schwabl, H. and Grössing, G. ‘Born’s rule as signature of a superclassical current algebra’. *Ann. Phys.* **343** (2014), 200–214. DOI: [10.1016/j.aop.2014.02.002](https://doi.org/10.1016/j.aop.2014.02.002). arXiv: [1308.5924](https://arxiv.org/abs/1308.5924) [quant-ph].
- Grössing, G., Fussy, S., Mesa Pascasio, J. and Schwabl, H. ‘Extreme beam attenuation in double-slit experiments: Quantum and subquantum scenarios’. *Ann. Phys.* **353** (2015), 271–281. DOI: [10.1016/j.aop.2014.11.015](https://doi.org/10.1016/j.aop.2014.11.015). arXiv: [1406.1346](https://arxiv.org/abs/1406.1346) [quant-ph].
- Grössing, G., Fussy, S., Mesa Pascasio, J. and Schwabl, H. ‘Implications of a deeper level explanation of the deBroglie–Bohm version of quantum mechanics’. *Quantum Stud.: Math. Found.* **2** No. 1 (2015), 133–140. DOI: [10.1007/s40509-015-0031-0](https://doi.org/10.1007/s40509-015-0031-0). arXiv: [1412.8349](https://arxiv.org/abs/1412.8349) [quant-ph].

Conference Proceedings

- Grössing, G., Fussy, S., Mesa Pascasio, J. and Schwabl, H. ‘Elements of sub-quantum thermodynamics: Quantum motion as ballistic diffusion’. *J. Phys.: Conf. Ser.* DICE2010, 13–17 September 2010, Castiglioncello, Italy **306** (2011), 012046. DOI: [10.1088/1742-6596/306/1/012046](https://doi.org/10.1088/1742-6596/306/1/012046). arXiv: [1005.1058](https://arxiv.org/abs/1005.1058) [[physics.gen-ph](#)].
- Schwabl, H., Mesa Pascasio, J., Fussy, S. and Grössing, G. ‘Quantum features derived from the classical model of a bouncer-walker coupled to a zero-point field’. *J. Phys.: Conf. Ser.* EmerQuM11, 11–13 November 2011, Vienna, Austria **361** (2012), 012021. DOI: [10.1088/1742-6596/361/1/012021](https://doi.org/10.1088/1742-6596/361/1/012021). arXiv: [1205.4519](https://arxiv.org/abs/1205.4519) [[quant-ph](#)].
- Mesa Pascasio, J., Fussy, S., Schwabl, H. and Grössing, G. ‘Classical simulation of double slit interference via ballistic diffusion’. *J. Phys.: Conf. Ser.* EmerQuM11, 11–13 November 2011, Vienna, Austria **361** (2012), 012041. DOI: [10.1088/1742-6596/361/1/012041](https://doi.org/10.1088/1742-6596/361/1/012041). arXiv: [1205.4521](https://arxiv.org/abs/1205.4521) [[quant-ph](#)].
- Grössing, G., Fussy, S., Mesa Pascasio, J. and Schwabl, H. ‘The quantum as an emergent system’. *J. Phys.: Conf. Ser.* EmerQuM11, 11–13 November 2011, Vienna, Austria **361** (2012), 012008. DOI: [10.1088/1742-6596/361/1/012008](https://doi.org/10.1088/1742-6596/361/1/012008). arXiv: [1205.3393](https://arxiv.org/abs/1205.3393) [[quant-ph](#)].
- Grössing, G., Fussy, S., Mesa Pascasio, J. and Schwabl, H. ‘A classical framework for nonlocality and entanglement’. *AIP Conf. Proc.* QTRF6, 11–14 June 2012, Växjö, Sweden **1508** (2012), 187–196. DOI: [10.1063/1.4773130](https://doi.org/10.1063/1.4773130). arXiv: [1210.4406](https://arxiv.org/abs/1210.4406) [[quant-ph](#)].
- Grössing, G., Fussy, S., Mesa Pascasio, J. and Schwabl, H. ‘Systemic nonlocality’ from changing constraints on sub-quantum kinematics’. *J. Phys.: Conf. Ser.* DICE2012, 17–21 September 2012, Castiglioncello, Italy **442** (2013), 012012. DOI: [10.1088/1742-6596/442/1/012012](https://doi.org/10.1088/1742-6596/442/1/012012). arXiv: [1303.2867](https://arxiv.org/abs/1303.2867) [[quant-ph](#)].
- Grössing, G., Fussy, S., Mesa Pascasio, J. and Schwabl, H. ‘Relational causality and classical probability: Grounding quantum phenomenology in a superclassical theory’. *J. Phys.: Conf. Ser.* EmQM13, 3–6 October 2013, Vienna, Austria **504** (2014), 012006. DOI: [10.1088/1742-6596/504/1/012006](https://doi.org/10.1088/1742-6596/504/1/012006). arXiv: [1403.3295](https://arxiv.org/abs/1403.3295) [[quant-ph](#)].
- Grössing, G., Fussy, S., Mesa Pascasio, J. and Schwabl, H. ‘The quantum sweeper effect’. *J. Phys.: Conf. Ser.* DICE2014, 15–19 September 2014, Castiglioncello, Italy **626** No. 1 (2015), 012017. DOI: [10.1088/1742-6596/626/1/012017](https://doi.org/10.1088/1742-6596/626/1/012017). arXiv: [1502.04034](https://arxiv.org/abs/1502.04034) [[quant-ph](#)].

- Grössing, G., Fussy, S., Mesa Pascasio, J. and Schwabl, H. ‘Conditions for Lorentz-invariant superluminal information transfer without signaling’. *J. Phys.: Conf. Ser.* **701** (2016), 012006. DOI: [10.1088/1742-6596/701/1/012006](https://doi.org/10.1088/1742-6596/701/1/012006). arXiv: [1603.02123](https://arxiv.org/abs/1603.02123) [quant-ph].
- Mesa Pascasio, J., Fussy, S., Schwabl, H. and Grössing, G. ‘Emergent quantum mechanics without wave functions’. *J. Phys.: Conf. Ser.* EmQM15, 23–25 October 2015, Vienna, Austria **701** (2016), 012036. DOI: [10.1088/1742-6596/701/1/012036](https://doi.org/10.1088/1742-6596/701/1/012036). arXiv: [1602.04932](https://arxiv.org/abs/1602.04932) [quant-ph].

Books

- Grössing, G., Elze, H.-T., Mesa Pascasio, J. and Walleczek, J., eds. *Emergent Quantum Mechanics 2013*. Vol. 504. Url: <http://iopscience.iop.org/1742-6596/504/1>. Bristol: IOP Publishing, 2014.
- Grössing, G., Elze, H.-T., Mesa Pascasio, J. and Walleczek, J., eds. *Emergent Quantum Mechanics 2015*. Url: <http://iopscience.iop.org/1742-6596/701/1>. Bristol: IOP Publishing, 2016.